MASTER'S THESIS

OBSERVATIONAL CHARACTERIZATION OF BALEARIC ISLANDS METEOTSUNAMIS AT AN UNPRECEDENTED HIGH SPATIAL RESOLUTION

Joan Villalonga Llauger

Master's Degree in Advanced Physics and Applied Mathematics

(Specialisation in geophysical fluids)

Centre for Postgraduate Studies

Academic Year 2020-21

OBSERVATIONAL CHARACTERIZATION OF BALEARIC ISLANDS METEOTSUNAMIS AT AN UNPRECEDENTED HIGH SPATIAL RESOLUTION

Joan Villalonga Llauger

Master's Thesis

Centre for Postgraduate Studies

University of the Balearic Islands

Academic Year 2020-21

Key words:

Meteotsunamis, Sea level, Atmospheric pressure disturbances, Balearic Islands

Thesis Supervisor's Name: Gabriel Jordà Sánchez

Tutor's Name: Angel Miguel Amores Maimó

Acknowledgements

Abstract

Meteotsunamis are atmospherically induced sea level oscillations with energy at the same frequency band that seismically induced tsunamis. Ciutadella harbour in Menorca is known to be one of the locations with more frequent occurrence of severe meteotsunamis worldwide: every year several events that exceed 1 meter of amplitude (trough-to-crest) are registered. This has motivated extensive research on this phenomenon in the Balearic Islands that has established the basis of the physical generation mechanisms responsible for the meteotsunami occurrence: the synoptic environment enables the formation of high-frequency atmospheric pressure disturbances that generate a sea level response which is amplified both at open sea, mainly by effect of the Proudman resonance, and at the coast, mainly by harbour resonance. Even though the proposed generation mechanisms can explain the energy transfer between the atmospheric perturbation and the sea wave, it is still not possible to infer the amplitude of the sea level oscillations from the atmospheric perturbation characteristics. This is due to the complex relationship between the atmospheric forcing and the sea wave amplification not being fully comprehended yet. It is also hard to correctly guess the formation of an atmospheric disturbance capable of provoking a meteotsunami from the synoptic conditions.

The goal of this thesis is to revise the established meteotsunami generation mechanism and to outline the features whose effects on the meteotsunamis amplitude are still uncertain. To do so, a series of meteotsunami events is analysed by means of the high spatial and temporal resolution data provided by a new ultra-dense observational network. Advanced techniques to estimate the atmospheric perturbation propagation velocity and the external forcing acting on the harbours are also implemented.

From the analysed events the idea that a certain established synoptic pattern is necessary to the occurrence of meteotsunamis is reinforced and the possible mechanism of generation and propagation of the atmospheric disturbance is suggested for every event. Furthermore, the amplification of the sea wave is found to be highly influenced by the propagation speed and direction of the atmospheric perturbation and the presence of atmospheric energy around the 10.5 min period (the normal mode of Ciutadella harbour) seems to be a requisite to the meteotsunami occurrence. Other factors not considered previously, as the phase difference between the incoming wave and the standing wave in the harbour and the perturbation duration, are observed to be crucial to determine the meteotsunami amplitude.

Contents

Chapter 1

Introduction

1.1 Meteotsunamis

Meteotsunamis, or atmospherically generated tsunamis, are oceanic waves with energy at the same frequency band that seismically induced tsunamis that are caused by atmospheric disturbances (Monserrat et al., 2006). This phenomenon, that has been identified all around the world (Balearic Islands (Jansà, 1986; Jansa et al., 2007), Sicily (Candela et al., 1999; Zemunik et al., 2021), the Adriatic Sea (Orlic, 1980; Vilibić and Šepić, 2009), the Great Lakes in the US (Ewing et al., 1954; Donn and Ewing, 1956) or Japan (Hibiya and Kajiura, 1982)), has associated sea level oscillation amplitudes that can be of several meters depending on the event and periods that vary from a few minutes to an hour depending on the topography of the place where are occurring. The atmospheric source of meteotsunamis is not as energetic as the seismic phenomena that cause tsunamis. For that reason, meteotsunamis are the result of the action of several amplification mechanisms that optimize the energy transfer between the atmosphere and the ocean (Monserrat et al., 2006). The generation mechanisms for meteotsunamis will be explained in detail in Chap. 2.

Japan is known for being a region with high tsunami wave incidence, therefore it is not strange that atmospherically induced seiches in harbours were first studied there by Honda et al. (1908). Later, Nomitsu (1935) pointed out the similarity between seismically induced tsunamis and atmospherically induced seiche amplification. They both have oscillation periods ranging from a few minutes to an hour and may have hazardous effects at the coast. In fact, in the tsunami catalogues, some of the events that have "unknown origin" are atmospherically induced tsunamis. These similarities have led the scientific community to accept the nomenclature meteotsunami or meteorological tsunami for this phenomenon (Monserrat et al., 2006). However, in the different regions where meteotsunami events are frequent they have received names in local languages such as *rissaga*, in the Balearic Islands (Jansa et al., 2007), *marrobio* in Sicily (Candela et al., 1999), *milghuba* in Malta (Drago, 2009), *šćiga* in the Adriatic Sea (Hodžić, 1979), *abiki* in Japan (Hibiya and Kajiura, 1982) or *Seebär* in the Baltic Sea (Metzner et al., 2000).

During the 20th century, meteotsunami events have been reported worldwide (e.g., Fontserè (1934); Ewing et al. (1954); Hodžić (1979); Hibiya and Kajiura (1982); Jansà (1986); Churchill et al. (1995); Candela et al. (1999)). Pattiaratchi and Wijeratne (2015) and Rabinovich (2020) have gathered scientific studies of meteotsunamis occurring all around the World Ocean. In particular, the work by Rabinovich (2020) is the first attempt of elaborating a meteotsunami catalogue in the same way of the existing tsunami cata-

logues (e.g., Intergovernmental Oceanographic Commission (2016); Okal (2019)). There, 51 meteotsunami relevant events, most of them with a wave height thought-to-crest of more than 1 meter, are reported in different worldwide locations from 1992 to 2019.

The author of that paper makes an interesting separation of meteotsunami events in different categories, depending on the weather conditions during the event and on the topographical characteristics of the affected coast. In first place, meteotsunamis can occur during *Bad Weather* conditions as consequence of storms or large and intense atmospheric processes, as typhoons, hurricanes, cold fronts or deep cyclones, that cause rapid atmospheric pressure variations at sea level; and they also can occur in *Good Weather*, i.e. apparently "calm" conditions for the atmosphere and the ocean. In this last case, meteotsunamis are caused by pressure perturbations that propagate through a stable layer at the lower troposphere (more details will be given in Sect. 2.1). Secondly, meteotsunamis were also classified between harbour oscillations, when an arriving meteotsunami wave excites the normal mode of the harbour causing large oscillation due to harbour resonance (Rabinovich et al., 2009), and solitary waves, when a singular meteotsunami wave reaches an open coastal region, such as a beach.

This classification is very useful to understand the potential destructive effects of meteotsunamis. Bad weather events are part of a major hazard and their destructive effects result from the combination of the meteotsunami with the simultaneous storm surge and wind-generated short waves. On the other hand, the good weather meteotsunamis are difficult to anticipate and it is hard to warn potentially affected populations. This type of meteotsunamis typically affect harbours that have the optimal topographical characteristics for the meteotsunami generation: these places are known as meteotsunami *hot spots*. Some examples are Vela Luka harbour in Croatia (Orlic, 1980; Orlić et al., 2010), Nagasaki Bay in Japan (Hibiya and Kajiura, 1982) and, may be the hottest spot, Ciutadella Harbour in Menorca (Jansà, 1986; Jansa et al., 2007). In these locations, meteotsunamis are known and have been studied for decades, which has led to population awareness and infrastructure adaptation to these events. This is the case for Ciutadella's port, which has been recently adapted to these sea level oscillations[1]. The most uncommon events are the good weather meteotsunamis that occur in open coasts as a solitary wave, yet this kind of meteotsunamis are the most dangerous for human lives since they happen suddenly without any evident previous sign. Some examples of meteotsunamis with dramatic consequences are the meteotsunami of 26 June 1954 in the Lake Michigan (Chicago) that killed seven people (Ewing et al., 1954), the meteotsunami of 4 July 1992 in Daytona Beach, Florida, that injured 75 people (Churchill et al., 1995) and the meteotsunami of 19 March 2017 in Bandar Dayyer, Iran, that caused six casualties (Salaree et al., 2018).

The meteotsunamis reported in the Balearic Islands fall within the category of good weather events (Rabinovich, 2020) and most of the largest sea level oscillations are observed within semi enclosed harbours as Portocolom or Port de Sóller, and they are particularly severe in Ciutadella Harbour. The large amount of meteotsunami events observed in Ciutadella has motivated its persistent research at that location.

---

[1]Link to local newspaper describing the Ciutadella Port remodelling: https://www.menorca.info/menorca/local/2011/02/02/532200/ports-confirma-los-amarres-ciutadella-seran-seguros.html

1.1.1 Research history for Ciutadella's *rissagues*

In Ciutadella Harbour, we have written evidence of meteotsunami events since the 15th century (Jansà and Ramis, 2021). Nevertheless, the generation mechanism of meteotsunamis in Ciutadella was not hypothesized until the 1980s. Jansà and Jansà (1980) observed the simultaneity of high-frequency atmospheric pressure oscillations with the sea level oscillations in Ciutadella and other ports of Mallorca and Catalonia. They hypothesized that the sea level perturbation generated by inverse barometer with the atmospheric pressure perturbation was amplified by harbour resonance, since the oscillation frequency of the perturbation was close to the normal modes of the harbour (more details on harbour resonance are provided in Sect. 2.2.2). Later, in the study made by Ramis and Jansà (1983), the synoptic pattern associated with meteotsunamis was established and related to the generation and propagation of atmospheric gravity waves.

On 21 June 1984 sea level oscillations of more than 3 meters hit Ciutadella Harbour, destroying several boats docked on the port (Jansà, 1986). As a consequence of this event, the interest for meteotsunamis grew within the Balearic scientific community. Two meetings were celebrated, leading to the initialization of two research lines: theoretical research and observational data collecting. Several works were done with the aim to theoretically explain the meteotsunami generation. They were particularly focused on explaining the amplification mechanisms responsible from the large meteotsunami waves at the coast (Tintoré et al., 1988; Gomis et al., 1993). On the other side, important efforts were made to increase the available atmospheric and oceanographic data with the sufficient high temporal resolution to study meteotsunamis (Monserrat et al., 1991a,b; Garcies et al., 1996; Rabinovich and Monserrat, 1996). The increase in available data would help to better understand the meteotsunami generation mechanisms: Monserrat and Thorpe (1996) confirmed the generation of a wave duct that allowed the atmospheric disturbances' propagation over the Balearic Islands, and Rabinovich and Monserrat (1998) started to study the role of atmospheric parameters such as the propagation velocity and the spectrum of the perturbation in the meteotsunami amplitude.

In the 21st century, the availability of computational resources have boosted the use of numerical models in meteotsunami research. Thanks to the use of a high-resolution 2D nonlinear shallow water model Vilibić et al. (2008) could reproduce the sea level oscillations of the catastrophic meteotsunami that hit Ciutedella in 15 June 2006 (Jansa et al., 2007), some images from this remarkable event are shown in Fig. 1.1. The sea level oscillation were underestimated by the model, although the model provided sea level information in all grid points that were useful to understand the meteotsunami amplification mechanisms in more detail.

1.1.2 Meteotsunami forecasting systems

One of the goals in meteotsunami research is to predict hazardous events which could have catastrophic consequences in people and coastal populations. The aim of these systems is to precisely forecast the meteotsunami event in order to early warn the affected population and infrastructures to avoid the potential damage.

The first meteotsunami early warning system was developed in the regional centre of the Spanish National Meteorological Institute (INM) at the Balearic Islands (Jansà, 1990). The system provided a probabilistic warning with different alarm levels from *no meteotsunami* to *extreme meteotsunami* based on subjective analysis of the forecasted synoptic conditions. A meteotsunami was considered as probable when the predicted

Figure 1.1: Images of Ciutadella Harbour in four different instants during the extreme meteotsunami of 17 June 2006. Source: Jansa et al. (2007)

atmospheric pattern was similar to that detailed in Ramis and Jansà (1983). In the short term (0h-12h), observations from soundings and satellites are incorporated and taken into account to obtain a more precise meteotsunami forecast. This system has been working since 1985 until present days, being now runned by the Spanish Meteorological Agency (AEMET).

In the last decade numerical models have been implemented to predict meteotsunamis. The Balearic RIssaga Forecasting System (BRIFS)[2] is a deterministic forecasting ensemble model developed by the Balearic Islands Coastal Observing and Forecasting System (SOCIB) to predict meteotsunamis in Ciutadella (Renault et al., 2011). This system has been running for the last ten years providing meteotsunami forecasts. No performance study has been performed but a tendency towards underestimating the meteotsunami heights was detected by Mourre et al. (2020) when using the BRIFS model to reproduce past events. In the Adriatic Sea, a similar forecasting system, called AdriSC (Adriatic Sea and Coast system), has been designed to predict meteotsunamis along the Croatian coast (Denamiel et al., 2019).

Alternative approaches to the meteotsunami forecasting have been suggested: Romero

---

[2]The predictions by BRIFS can be found in: https://www.socib.es/?seccion=modelling&facility=rissagaforecast

et al. (2019)[3] proposed to use a simplified numerical model of very high resolution which takes into account the physical characteristics of meteotsunamis and Vich and Romero (2021) trained a neuronal network to predict the meteotsunami height in Ciutadella. Both systems have a performance comparable to those of AEMET and BRIFS warning systems (Vich and Romero, 2021).

The proposal of different forecasting methods is motivated by the performance problems that all the current forecasting systems present when predicting the meteotsunami amplitude and the time of occurrence. Up to our knowledge, there are no comprehensive studies that analyse the performance of the implemented meteotsunami forecasting systems. Nevertheless, the meteotsunami events observed during summer 2021 provide a quick overlook on the weaknesses of these systems. Several false alarms have been given during this time period, as for example, in 7 July 2021 when the warning systems of AEMET and BRIFS alerted from meteotsunamis with amplitude between 100 and 130 cm while the measured one in Ciutadella was of 30 cm and in 25 September 2021 the BRIFS anticipated meteotsunamis of more than 2 meters when the measured oscillations only reached 50 cm. These are not isolated examples, more false alarms have occurred during summer 2021. There are some cases where the meteotsunami event has been indeed predicted, but the amplitude predictions failed for 30 - 50 cm. One of the problems with the BRIFS model is that the different ensembles of the model can provide very different estimations that can go from 50 to 200 cm in some extreme cases. This uncertainty is too large to consider it as a reliable warning system. All in all, it is clear that these systems have a great margin to improve.

1.2 Motivation and contents

Meteotsunamis are important hazards that affect the coast all over the World Ocean and may have important catastrophic consequences over people and coastal infrastructures. They are more relevant in some ocean basins where the optimal conditions for the occurrence of this phenomenon are found, as is the case for the Balearic Islands and Ciutadella Harbour in particular. Even in these places where meteotsunamis have been widely studied there are unclear features on the physical mechanism that determines the magnitude and timing of such events and, as a result of these uncertainties, the current warning and forecasting systems can still be improved.

Recently, the Sea Level and Climate group of the University of the Balearic Islands (UIB) and the Spanish Institute of Oceanography (IEO), in the context of project VENOM, has deployed a new ultra-dense network of tide gauges that is providing a large amount of new observational high-resolution sea level data. In this work we will combine sea level and atmospheric pressure high temporal resolution data, from the VENOM network and other sources (more details on the data used in Sect. 3.1), to analyse in detail the meteotsunami events of 10 May, 23 May and 18 June 2021. Based on these observations, we will revise the established generation mechanism of meteotsunamis trying to answer some of the questions that remain still unsolved within the meteotsunami's field.

In the Chap. 2 the current knowledge concerning the generation mechanism will be presented, from the synoptic scale meteorological pattern to the final sea level oscillation within the harbour, passing by the generation and propagation of mesoscale atmospheric disturbances and by the amplification mechanism of the sea waves. Chap. 3 will provide

---

[3]The predictions Romero et al. (2019) model can be found in: https://meteo.uib.es/rissaga/

all the information about the data and the methods used in the analysis. In Chap. 4 the observed meteotsunami events will be presented in detail and in Chap. 5 these results will be discussed. Finally, in Chap. 6 the concluding remarks will be given.

Chapter 2

Meteotsunamis generation mechanism

As it is introduced in Chap. 1, scientific research has gathered an important amount of information about the generation of meteotsunamis worldwide, being Ciutadella one of the most studied locations. In the following chapter, a summary of the knowledge gathered about the generation mechanisms for the meteotsunamis in Ciutadella is presented. Most of the knowledge of the generation of meteotsunamis there can be generalized to other *good weather* meteotsunamis (Rabinovich, 2020) around the World Ocean.

The established meteotsunami generation mechanism can be summarized in the following parts:

  i. A particular synoptic-scale atmospheric situation brings the conditions for the generation and propagation of mesoscale atmospheric pressure disturbances.

  ii. Atmospheric disturbances are generated by dynamic stability or convective activity and then propagated over the Balearic Islands thanks to the formation of a wave duct or to the coupling between the perturbation and convection (wave-CISK mechanism).

  iii. The atmospheric pressure perturbation generates a response in the sea level by inverse barometer effect. The coupling between the propagating atmospheric perturbation and the generated sea wave causes the amplification of the resulting sea wave (schematic representation in Fig. 2.1).

  iv. The amplified sea wave arrives to the coast where it gains more amplitude due to wave shoaling, shelf resonance and harbour resonance. Here, the meteotsunami wave reaches its maximum amplitude.

This chapter is organized as follows: in Sect. 2.1.1 the synoptic conditions necessary for the occurrence of meteotsunamis will be detailed; in Sect 2.1.2 we will take a close look at the generation and propagation of the mesoscale atmospheric disturbances; Sect. 2.2.1 tackles the coupling between atmospheric pressure perturbation and its sea level response, and the explanation of the different amplifications mechanisms of the sea wave. The topographical amplification suffered by the sea wave when it reaches the coast is explained in Sect. 2.2.2. Finally, in Sect. 2.3, the identified research gaps are gathered, and the objectives of this work are described in Sect. 2.4.
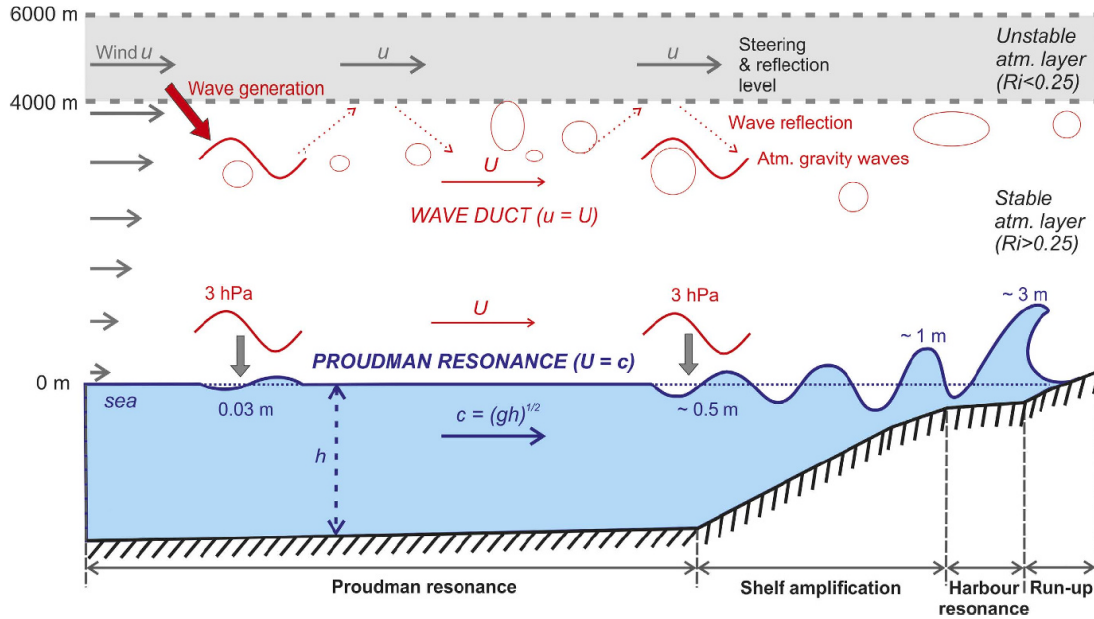
Figure 2.1: Schematic representation of the meteotsunami generation mechanism. Source: Šepic et al. (2015)

2.1 Atmospheric disturbances

Depending on the region that we are studying, meteotsunamis may have different atmospheric origins. In this work, we will study the atmospheric patterns related to meteotsunami occurrence in the Balearic Islands from different scales.

2.1.1 Synoptic patterns

Ramis and Jansà (1983) were the first to report the synoptic conditions associated with meteotsunamis in the Balearic Islands from observations of four severe meteotsunami events occurred between 1975 and 1981. They identified three key conditions:

 i. The presence of warm and dry air masses coming from North Africa at low levels ($\sim$850 hPa, $\sim$1500 m) which can cause a temperature inversion in the lower troposphere. The inversion produces a strong stratification at that level, which is associated with high atmospheric stability.

 ii. Strong wind jet of more than 20 m/s in the mid-troposphere, i.e., between 3 and 8 km height. During the Ciutadella meteotsunamis we expect the jet direction to point north-eastwards, i.e., towards the entrance of Ciutadella Harbour.

 iii. An unstable layer in the mid-troposphere with a Richardson number[1] lower than

---

[1] The Richardson number is considered as a way to measure the turbulence within a fluid (Stull, 1988). It is obtained combining the effect of the two turbulence generation mechanisms, which are buoyancy and wind shear. Thus, the gradient Richardson number is defined as the ratio between the stability (reduces turbulence) and the wind shear (increases turbulence): $Ri = \frac{N^2}{\left(\frac{du}{dz}\right)^2}$.

On one hand, large values of Ri will correspond to stable atmospheric layers with no wind shear that will present laminar flows. On the other hand, small Ri will be associated with low or no stability and strong wind shear, leading to a turbulent flow. It has been established that 0.25 is the critical value for the Ri when the flow goes from turbulent to laminar or vice versa.

0.25. From the definition of the Richardson number, it is deduced that a strong wind shear in this layer will contribute to the fulfilment of this condition.

The existence of these conditions has been observed in several meteotsunami events (e.g., Jansà (1986); Jansa et al. (2007); Šepic et al. (2015); Šepić et al. (2016)). In Šepić et al. (2009), they used the ECMWF (European Center for Medium-Range Weather Forecasts) ERA-40 reanalysis to verify the fulfilment of the mentioned synoptic conditions for 32 events of meteotsunamis in Ciutadella. They proved that the 3 conditions were present in 23 of the 32 events (i.e., 72%), and there was just one case when only one of the three conditions was present. A first attempt to quantify the relationship between the synoptic atmospheric conditions and sea level oscillations in Ciutadella was made by Šepić et al. (2016) by creating an empirical index that related the synoptic conditions to the meteotsunami amplitude. They identified a threshold level on the synoptic index that needed to be surpassed for a meteotsunami to occur in Ciutadella. However, they observed that just in the 20% of the cases with *favourable* synoptic conditions (i.e., for a synoptic index over the threshold level) a meteotsunami in Ciutadella occurred. Therefore, they concluded that the synoptic pattern described above is necessary but not sufficient for meteotsunami occurrence, which implies that there exist key parameters in the generation and propagation of meteotsunamigenic disturbances that cannot be resolved in the synoptic scale.

Šepic et al. (2015) proved that these particular synoptic conditions, that enhance meteotsunamis, can propagate and endure in large spatial regions. They observed how the described synoptic pattern propagated eastwards over the whole Mediterranean, from Balearic Islands (23 June 2014) to the Black Sea (27 June 2014) passing over the Adriatic Sea (25-26 June 2014), causing destructive meteotsunamis in different locations.

2.1.2 Atmospheric gravity waves generation and propagation

As introduced above, most meteotsunamis in the Balearic Islands occur in *good weather* conditions as a consequence of high-frequency atmospheric pressure perturbations. There are different generation mechanisms that could create these rapid atmospheric pressure perturbations. The main hypotheses are that they are generated from wind shear stress, convection or orography, but it is still unclear which is the major source of meteotsunamigenic atmospheric perturbations (Vilibić et al., 2020). Independently of the generation mechanism, it has been observed that these perturbations can travel long distances, one complete wavelength or more, without dissipating (Monserrat et al., 1991a,b; Monserrat and Thorpe, 1992), which indicates that some propagation mechanism must exist that traps the perturbation energy near the surface avoiding its dissipation to upper atmospheric levels.

Monserrat and Thorpe (1992) carried out a pioneering study in the characterization of atmospheric gravity waves in the Balearic Islands, relating them to the meteotsunami generation in Ciutadella. They used a triangular array of high-resolution barographs to compute the phase speed and propagation direction of the travelling atmospheric wave train. They found out that the observed atmospheric waves were non-dispersive and pointed towards the wave ducting mechanism proposed by Lindzen and Tung (1976) as the energy trapping mechanism that allowed the long travelling of the atmospheric perturbations. In Monserrat and Thorpe (1996) the authors adapted the wave ducting theory introduced by Lindzen and Tung (1976) to the observational data collected by Monserrat and Thorpe (1992) and they concluded that there was evidence enough to

confirm the existence of a wave duct during the studied events. Later, the work done by Belušić et al. (2007) reported a meteotsunami event in the Croatian coast where the conditions differed from those of a wave duct and suggested the wave-CISK as responsible for the atmospheric disturbance propagation. Both mechanisms will be explained in detail in the remaining part of the present section.

A. Wave duct theory

To comprehend the atmospheric conditions associated with meteotsunamis it is important to understand how the wave duct works. To study analytically the generation of the wave duct Lindzen and Tung (1976) idealize the atmosphere as a 2D fluid, with one horizontal dimension x and one vertical z and with no dependence on the transversal horizontal dimension, i.e., $v = 0$ and $\frac{\partial}{\partial y} = 0$; where all displacements are adiabatic; the air is considered an incompressible fluid; and neglecting the effects of the Earth rotation. Thus, we also assume that the flow is composed by a stationary main, or basic, flow (denoted by $(\bar{\cdot})$) plus small perturbations (denoted by $(.')$) for all state variables :

$$u = \bar{u}(z) + u'(t, x, z), \tag{2.1}$$
$$w = w'(t, x, z), \tag{2.2}$$
$$\theta = \bar{\theta}(z) + \theta'(t, x, z), \tag{2.3}$$
$$p = \bar{p}(z) + p'(t, x, z), \tag{2.4}$$

where u is the wind velocity in the x direction; w is the wind velocity in the vertical direction, whom basic mean flow is considered zero ($\bar{w} \approx 0$); θ is the potential temperature; and p is the pressure. We also hypothesize that the basic state is in hydrostatic equilibrium, i.e.,

$$\partial_z \bar{p} = -g\bar{\rho}. \tag{2.5}$$

Then, the fluid mechanics equations of momentum conservation, mass conservation and energy conservation can be simplified into:

$$\partial_t u' + \bar{u}\partial_x u' + w'\partial_z \bar{u} = -\frac{1}{\bar{\rho}}\partial_x p', \tag{2.6}$$

$$\partial_t u' + \bar{u}\partial_x w' + w'\partial_z \bar{u} = -\frac{1}{\bar{\rho}}\partial_z p' + \frac{g\theta'}{\bar{\theta}}, \tag{2.7}$$

$$\partial_x u' + \partial_z w' = 0, \tag{2.8}$$
$$\partial_t \theta' + \bar{u}\partial_x \theta' + w'\partial_z \bar{\theta} = 0. \tag{2.9}$$

Now, we can try a horizontally propagating wave as a solution for the vertical velocity perturbation,

$$w' = w(z)e^{ik(x-ct)}, \tag{2.10}$$

where k is the horizontal wavenumber, c is the phase propagation velocity, and $w(z)$ is the vertical structure function. Applying Eq. 2.10 into Eq. 2.6 - 2.9 we reach the so-called Taylor-Goldstein equation for the vertical structure function, w from now on:

$$\frac{d^2 w}{dz^2} + \left[\frac{N^2}{(c - \bar{u})^2} + \frac{1}{(c - \bar{u})} \frac{d^2 \bar{u}}{dz^2} - k^2 \right] w = 0, \tag{2.11}$$

where $N^2 = \frac{g}{\theta}\frac{d\bar{\theta}}{dz}$ is the Brunt-Väisälä frequency known to be a measure of the atmospheric stability. Eq. 2.11 accept wave solutions depending on the sign of the vertical wave number $m^2 = \left[\frac{N^2}{(c-\bar{u})^2} + \frac{1}{(c-\bar{u})}\frac{d^2\bar{u}}{dz^2} - k^2 \right]$:

10

- If $m^2 > 0$, we obtain propagating wave solutions for w'.

- If $m^2 < 0$, we obtain vanishing with height solutions for w'.

Therefore, to have atmospheric gravity waves, we need $m^2 > 0$. For the simplest case, an atmospheric profile with no wind shear, the following inequality must be fulfilled by the waves that propagate horizontally:

$$\frac{N}{c - \bar{u}} > k. \tag{2.12}$$

This means that as more stable the atmosphere is (i.e. larger is N) more modes will propagate.

In the case of a wave duct we can study the atmosphere as a superposition of air layers, each one with a different constant N. The first layer, in contact with the surface, is stable (large N and $m^2 > 0$) and non-dispersive waves can propagate within it; we will call wave duct to this layer. The duct is capped by an unstable layer (smaller N and $m^2 < 0$) that reflects the waves back to the duct, trapping the energy near the surface. The reflection between layers can be understood similarly to the reflection of electromagnetic waves when they change from one medium with a refractive index to a medium with a different refractive index.

According to Lindzen and Tung (1976) the duct amplifies some waves modes over others depending on the duct height, H. The first propagating mode that fulfils the duct boundary conditions is that with $\lambda_z = 4H$, and it is also the largest mode. Although Eq. 2.11 accepts infinite wave modes, all smaller than the first one, the largest ones will be the only observed modes since they are less attenuated by turbulent dissipation. The propagation velocity for the first wave mode can be computed as:

$$c \approx \frac{2NH}{\pi} + \bar{u}. \tag{2.13}$$

Then, a wave duct with Brunt-Väisälä frequency $N = 0.015$ s^{-1} and no horizontal wind, $\bar{u} = 0$, where the wave propagates with a velocity $c = 28$ m/s should have a height of approximately 3 km.

Lindzen and Tung (1976) also point out that a key feature to have an optimal wave duct is the presence of a critical level in the capping layer. A critical level is defined as that vertical level where the wind velocity matches the wave propagation velocity ($\bar{u} = c$). It can be proven that if the critical level is found within an unstable layer (Ri< 0.25) it generates an overreflection ($R > 1$) which means that the wave will grow by tacking energy from the mean flow. At this point the vertical group velocity of the wave vanishes which prohibits the energy dissipation into upper levels, confining the wave energy at the ducting layer. Therefore, one of the conditions to have waves travelling through a duct is that their propagation velocity matches the wind velocity at some level of the aloft unstable layer. Continuing with the example presented above, to have a critical level there should be some level within the unstable capping layer, above $H = 3$ km, where the wind reaches a speed of 28 m/s to produce overreflection.

Summarizing, an optimal wave duct that allows the propagation of atmospheric gravity waves over large distances should fulfil the following conditions:

- The presence of a lower stable layer in contact to the ground that allows the wave propagation. This layer may contain a thermal inversion and it receives the name of wave duct.

- The duct should be capped by an unstable layer with Ri< 0.25. This layer has small N and acts as a reflector.

- The existence of an important wind shear at the unstable layer with wind speeds capable of matching the wave propagation velocity would result in the appearance of an overreflecting critical level.

Although the previous conditions are obtained theoretically for idealized conditions, they have been observed when important atmospheric gravity waves have been detected (Monserrat and Thorpe, 1996). We can relate the synoptic pattern introduced by Ramis and Jansà (1983) with the described atmospheric profile needed to the presence of a wave duct: in first place the entrance of African warm air at lower levels creates the conditions necessary to stabilize the lower troposphere resulting on a wave duct. The upper cooler air will present less stability and the strong wind jet detected at higher levels will create an important wind shear that will contribute to the dynamical instability of the capping layer and favour the existence of a critical level within this upper layer.

B. Coupling between waves and convection (wave-CISK)

As is concluded in Šepić et al. (2016), similar atmospheric patterns are present in all Ciutadella meteotsunamis. However, most of the studies do not investigate in detail the origin of the atmospheric perturbation and its propagation mechanism, since the authors usually assume that the environmental conditions are adequate for the formation of a wave duct. Nevertheless, there are studies (e.g., Powers and Reed (1993)) that prove that important atmospheric pressure perturbations can be propagated without the existence of a wave duct thanks to the reinforcement produced between atmospheric waves and convective activity, also known as wave-CISK (Conditional Instability of Second Kind).

If the atmosphere is conditionally unstable but unsaturated and an air parcel at the surface is moist and warm enough, there will exist a level where this parcel would saturate and start rising by buoyancy called Free Convection Level (FCL). This convective movement is driven by the latent heat released in vapour water condensation during the rising, but it needs from some initialization mechanism to raise the air parcel to the FCL. In CISK, this mechanism is the convergence at low levels (Lindzen, 1974). We are talking about wave-CISK when the convergence that allows the initialization of convection is caused by atmospheric waves. This can lead to a positive feedback loop where the convection and gravity waves couple and reinforce each other: the wave causes convergence that starts convection, which releases latent heat that provides energy to the wave propagation.

In Powers and Reed (1993) some events of atmospheric gravity waves are simulated with the MM4 model. They analyse the presence of a wave duct in the different events, and they reach the conclusion that the wave duct mechanism is not enough to explain the atmospheric waves' amplitude. They conclude that the wave-CISK mechanism contributes to the wave propagation since convective activity is observed moving in phase with the atmospheric gravity waves. In this case, convection occurs in the mid-troposphere aloft the stable wave duct, and optimal wave propagation is given when the maximum upward motion is found at the critical level of the unstable layer. It is shown that the convective uprising cell and the consequent subsidence downstream are in phase with a pressure crest and trough, respectively, at surface level. According to this study, the wave duct and the wave-CISK mechanism can easily coexist, with leads to the conclusion that the described

synoptic pattern that suites to the existence of a wave duct would also be compatible which the occurrence of wave-CISK interaction.

In the meteotsunami field, Belušić et al. (2007) used an MM5 atmospheric model to reproduce the atmospheric disturbances that caused a meteotsunami in the Adriatic coast the 26/27 June 2003. They reproduced atmospheric gravity waves that generated over the Alps consequent with the air pressure observations. The lack of a wave duct indicated that the wave-CISK mechanism was the main responsible for the wave amplification and propagation. Indeed, the model outputs showed how convection and wave travelled together over the Adriatic Sea. Unfortunately, there are no analogue studies in the Balearic Islands that use high resolution numerical models to compare the contribution of wave duct and wave-CISK in the atmospheric disturbance propagation, as was made for a meteotsunami event in the Adriatic by Šepić et al. (2009). This comparison cannot be made from observational data, like pressure time series or soundings data, since we need high-resolution observations of the atmospheric profiles to discern the propagation mechanism and, nowadays, this information is only provided by the mesoscale atmospheric numerical models.

There are some observational studies that associate atmospheric pressure jumps measured during meteotsunamis in Ciutadella to moving mesoscale convective systems. In fact, several major meteotsunamis (> 2 m) (Jansà, 1986; Jansa et al., 2007) are related to important pressure jumps caused by convective activity. Jansà and Ramis (2021) proposes to investigate if these large amplitude events can occur just with an atmospheric gravity wave train or, otherwise, they need from a convective pressure jump. The authors also remark the lack of research concerning the characterization of the atmospheric part of meteotsunamis.

2.2   Oceanic waves amplification

Once we have detailed the main mechanisms of generation and propagation of atmospheric perturbations that cause meteotsunamis in the Balearic Islands, we are going to explain how the perturbation energy is transferred to the sea, generating the meteotsunami wave that will propagate and amplify along the oceanic shelf. We know that the direct sea level change due to the atmospheric pressure perturbations, the *inverse barometer* effect, is of 1 cm of sea level change for every 1 hPa of amplitude of the atmospheric pressure perturbation. This response is too weak to produce important effects at the coast, since the typical atmospheric pressure perturbations do not surpass the 10 hPa. Nevertheless, the observed meteotsunamis can reach several meters of amplitude, which evidences the existence of some mechanisms of amplification that increase the sea level response.

From the early meteotsunami studies carried out worldwide (e.g., Ewing et al. (1954); Orlic (1980); Hibiya and Kajiura (1982); Jansà (1986)) it was already suggested that the meteotsunami wave suffered from amplification in at least two steps: first when propagating at open sea coupled to the atmospheric disturbance and, later, by interaction with the topographical accidents of the coast by, for instance, shoaling and resonance within a harbour. Hibiya and Kajiura (1982) were the first to measure separately the effects of both amplifications for the severe meteotsunami (*abiki* in Japanese) event of 31 March 1979 in Nagasaki Bay. The measured pressure perturbation had an amplitude of 3 hPa, which implies an expected sea level response of 3 cm. However, a tide gauge located close to the entrance of Nagasaki Bay measured sea level oscillations of ~ 20 cm and the final amplitude of the meteotsunami within Nagasaki Bay reached 278 cm of trough-to-crest

amplitude. Hence, a first amplification took place at open sea when the atmospheric perturbation and the sea wave travelled together and a second amplification occurred at the coast first by shoaling and second by harbour resonance. These hypotheses were consistent with the numerical reproduction of the event presented in that paper.

Consequently, it makes sense to separate the sea wave amplification in these two steps, since the amplification mechanisms will be different at open sea and at the coast. The remaining part of this section will address the different sea wave amplification mechanisms that have been proposed in the literature, first at open sea and, then, by topographical effects at the coast.

2.2.1 Open-sea generation and amplification

The amplification of the sea wave at open sea are of huge importance to the occurrence of severe meteotsunamis since the amplification capacity of ports and harbours is not enough to generate sea level oscillations of the order of meters (Garcies et al., 1996). An argument in favour of this hypothesis is the occurrence of meteotsunamis at open coasts (e.g., Ewing et al. (1954); Churchill et al. (1995)). The question then is which are the mechanisms that contribute to amplify the ocean wave generated by the atmospheric disturbance. Most of the studies have taken the Proudman resonance (Proudman, 1929) as the more relevant mechanism for the sea wave amplification, although Greenspan resonance (Greenspan, 1956) has also been proposed as open sea amplification mechanism. Now, the Proudman resonance mechanism will be explained in detail and, later, the Greenspan resonance will also be introduced.

A. Proudman resonance

The resonant amplification of a long sea wave coupled to an atmospheric pressure perturbation was first theorized by Proudman (1929), thus, receiving the name of Proudman resonance. In some of the first scientific works on meteotsunamis, this mechanism was already pointed out as responsible of at least some part of the sea wave amplification (e.g., Ewing et al. (1954); Orlic (1980); Jansà (1986)). In the mentioned above study of Hibiya and Kajiura (1982), the authors used a numerical model to prove the occurrence of Proudman resonance and to quantify its contribution to the sea wave amplification. Later, most of the observational and numerical studies have reinforced the idea that this mechanism is crucial in the meteotsunami generation (e.g., Jansa et al. (2007); Vilibić et al. (2008); Orlić et al. (2010); Bechle and Wu (2014)).

The Proudman resonance mechanism can be obtained analytically from a simple 1D *shallow water* model. The *shallow water* model is a simplification of the momentum conservation and continuity equations for an incompressible fluid, where we neglect the effects of the Earth rotation and the viscous friction. Moreover, the assumption that gives the *shallow* name to the model is that de depth H of the water in considered to be very small in comparison with the horizontal dimension L. The *shallow water* model equations are:

$$\frac{\partial u}{\partial t} + u\frac{\partial u}{\partial x} + \frac{1}{\rho}\frac{\partial p}{\partial x} = 0, \tag{2.14}$$

$$\frac{\partial \eta}{\partial t} + \frac{\partial (uh)}{\partial x} = 0, \tag{2.15}$$

where u is the flow velocity in the x direction, p is the pressure at the surface, η is the sea surface level variation, called free surface, and h is the sea depth which is the sum of the sea level variation plus the stationary water depth (z_b), i.e., $h = \eta + z_b$. In the simplest case, z_b will be constant. The atmospheric pressure term will be written as the sum of a constant atmospheric pressure P_{atm} plus an atmospheric pressure disturbance $\hat{p}(t, x)$, and plus the hydrostatic variation of pressure caused by a height change in the water column $\rho g \eta(t, x)$:

$$p(t, x) = P_{atm} + \hat{p}(t, x) + \rho g \eta(t, x). \tag{2.16}$$

Then, we can write the atmospheric pressure disturbance in terms of its sea level response by the *inverse barometer* effect, $\hat{\eta}$, as

$$\hat{\eta}(t, x) = -\frac{\hat{p}(t, x)}{\rho g}. \tag{2.17}$$

Now, applying Eq. 2.16 and 2.17 into Eq. 2.14, taking a constant water depth ($z_b = H$) and neglecting the non-lineal terms, we reach a forced wave equation for the sea level:

$$\frac{\partial^2 \eta}{\partial t^2} - gH \frac{\partial^2 \eta}{\partial x^2} = -gH \frac{\partial^2 \hat{\eta}}{\partial x^2}. \tag{2.18}$$

If no atmospheric perturbation is present, the solutions to Eq. 2.18 will be free waves that propagate in the horizontal direction with a phase velocity $c = \sqrt{gH}$. In the case of meteotsunamis a moving atmospheric pressure perturbation is present, and it can be written as $\hat{\eta}(x - Ut)$ if we consider that it propagates at a constant phase velocity U. Introducing this kind of forcing into Eq. 2.18, we reach the following solution (Proudman, 1929):

$$\eta(x, t) = \frac{Fr}{Fr^2 - 1} \hat{\eta}(x - Ut) - \frac{Fr^2}{2(Fr - 1)} \hat{\eta}(x - ct) + \frac{Fr^2}{2(Fr + 1)} \hat{\eta}(x + ct), \tag{2.19}$$

where the Fround number is defined as the ratio between the perturbation velocity and the free wave velocity, $Fr = \frac{U}{c}$. This solution presents three different waves: the first is a forced wave which moves together with the atmospheric perturbation, while the second and the third are free waves propagating forward and backward, respectively. In can be seen that the amplitude of both forward propagating wave would reach infinite amplitudes if the velocity of the atmospheric perturbation matches the velocity of the free wave ($Fr = 1$). Thus, if we compute the limit when $Fr \to 1$ we obtain the following expression for the sea level:

$$\eta(x, t) = -\frac{Ut}{2} \frac{\partial \hat{\eta}(x - Ut)}{\partial x} + \frac{1}{4} \hat{\eta}(x + ct). \tag{2.20}$$

As we can see, the forward propagating sea wave will grow during all the time that the atmospheric disturbance and the oceanic wave travel together due to the transfer of energy from the atmosphere to the ocean.

Then, if we idealize the atmospheric perturbation as a pressure jump with amplitude Δp, a distance L_1 between the beginning of the pressure jump and the pressure maximum and that travels over the sea in optimal resonance conditions, i.e., $Fr = 1$, for a distance $x_f = Ut$, the amplitude of the forced wave, $\Delta \eta$, can be computed, according to Eq. 2.20, as

$$\Delta \eta = \frac{x_f}{2L_1} \Delta \hat{\eta}, \tag{2.21}$$

15

where $\Delta\hat{\eta} = -\frac{\Delta p}{\rho g}$ (Hibiya and Kajiura, 1982). Consequently, the amplitude of the perturbation, the rate of change of the pressure jump and the distance that the forced wave and the atmospheric perturbation travel together are key parameters in the sea wave amplification produced by Proudman resonance.

In the real ocean the bathymetry is not constant and the friction dissipates part of the energy which limits the amplification described by Eq. 2.21. Typical atmospheric perturbations travel at velocities between 20 and 40 m/s, therefore, their sea level response should be amplified by Proudman resonance in ocean basins with depth between 40 and 160 m (Pattiaratchi and Wijeratne, 2015). The conditions for the occurrence of Proudman resonance during meteotsunami events have been found around the World Ocean: in the Great Lakes (Ewing et al., 1954), in the Balearic Islands (Vilibić et al., 2008; Ličer et al., 2017), in Sicily (Zemunik et al., 2021), in the Adriatic Sea (Orlic, 1980; Orlić et al., 2010; Šepić et al., 2015) and at the Japanese coast (Hibiya and Kajiura, 1982) among others.

Since the Proudman resonance mechanism is obtained from a very simplified model for the sea, it should be tested how sensible it is to changes in the idealized conditions. Some studies have used simplified numerical models to experiment with Proudman resonance. Williams et al. (2021) investigated the effects of currents and tide in the occurrence of Proudman resonance, concluding that the phenomenon is weakly perturbed by these circumstances. They also tried the effects of varying propagation velocity of the atmospheric disturbance, and they found out that rapid variations in the Fr between 0.8 and 1.2 around a mean $Fr = 1$ still produced effective Proudman amplifications. These results reinforce the hypothesis that Proudman resonance is important in the meteotsunami generation mechanism, since it does not need from a strong fulfilment of the idealized conditions to produce important amplifications. The effect of a slope in the bathymetry on the Proudman resonance has also been explored, concluding that in these cases the shoaling effect also contributes to the sea wave amplification and that gentle slopes provide larger Proudman amplifications (Vennell, 2007; Williams et al., 2021). Finally, the experiments of Williams et al. (2021) also proved that the amplification ratio, i.e., $\frac{\Delta\eta}{\Delta\hat{\eta}}$, of the sea wave by Proudman resonance does not depend on the amplitude of the pressure disturbance, the same conclusion that is reached from Eq. 2.21.

In addition to these experiments for simplified models, some studies have applied numerical simulations on the real ocean basins (e.g., Vilibić et al. (2008); Orlić et al. (2010); Šepić et al. (2015); Ličer et al. (2017)). Vilibić et al. (2008) and Ličer et al. (2017) are focused on studying the meteotsunamis in Ciutadella Harbour. The first one forced an oceanic model with a 7 hPa pressure jump and the second one with a sinusoidal perturbation, both changing the perturbation propagation speed and direction to estimate the wave amplification produced as function of these variables. They showed how a wide range of propagation directions, 210° - 260° (degrees from the north), and propagation speeds, 24 - 36 m/s, can lead to important meteotsunamis at Ciutadella. In the later study by Ličer et al. (2017), they also study separately the amplification produced by Proudman at the southern Mallorca shelf, the northern Mallorca shelf and the channel between Mallorca and Menorca (see the map in Fig. 2.2). The conclusions were that more than the 70% of the amplification is produced on the channel. Therefore, to have an important meteotsunami in Ciutadella, the propagation of the atmospheric perturbation over the Menorca channel is necessary. Moreover, it has been observed that large meteotsunamis in Ciutadella may appear as a consequence of atmospheric disturbances that generate over the channel, without affecting the rest of the Balearic Islands. The southern and northern shelves work as wave guides, focusing the wave to the channel, but cannot produce enough
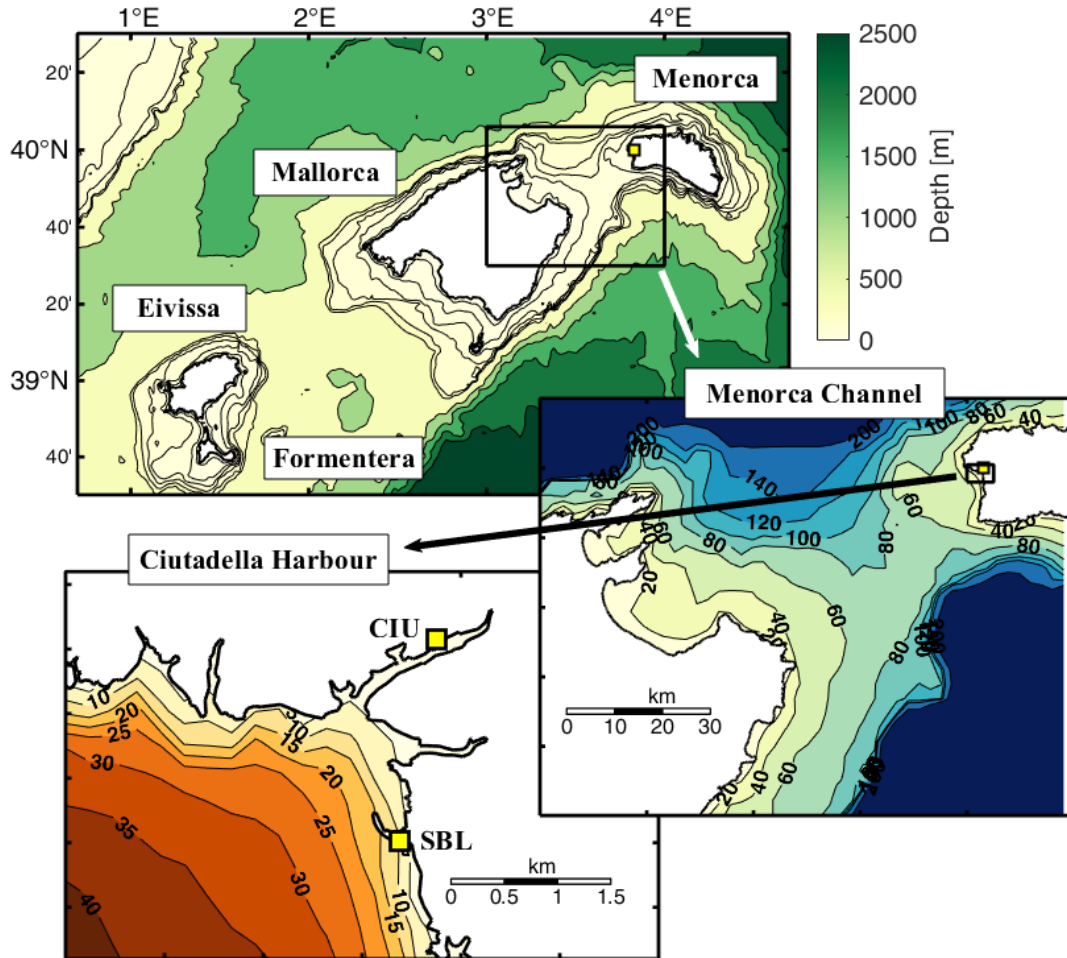
Figure 2.2: Map of the Balearic Islands with its surrounding bathymetry, different scales are shown. From top to bottom: complete map of the Balearic Islands, contour lines every 30 m from 0 to 200 m and every 500 m from 500 to 2500 m; map of the Menorca Channel with contour lines every 20 m; map of Ciutadella Harbour and its preceding shelf with contour lines every 5 m, Ciutadella Harbour (CIU) and Son Blanc (SBL) tide gauges are marked with a yellow square. In the two upper maps, Ciutadella is marked with a yellow square.

amplification by themselves.

The importance of the Menorca Channel as amplification area of the ocean wave before hitting Ciutadella Harbour was already pointed out in Rabinovich and Monserrat (1998) as the key to explain the frequent occurrence of severe meteotsunamis in Ciutadella. The authors noted that Ciutadella inlet is capable of producing a large amplification to external forcings with energy at its fundamental period, but harbours with similar natural responses can be found around the world, and they do not suffer from that many meteotsunami events. Thus, they concluded that the key feature that conditioned the large number of meteotsunamis occurring in Ciutadella was the good conditions for Proudman resonance offered by the Menorca Channel and the fact that the entrance of Ciutadella Harbour is orientated towards it. The Menorca Channel has depths between 70 and 120 meters which produces resonance with propagation speeds between 26 and 35 m/s and the Ciutadella Harbour entrance is oriented to 228°. This reasoning is clearly supported

by the simulations of Vilibić et al. (2008) and Ličer et al. (2017).

Although the Proudman resonance is the more studied sea wave amplification mechanism and seems to be common on most of meteotsunamis around the world, there are more amplification mechanisms that can contribute to increase the meteotsunami energy at the coast.

B. Greenspan resonance

Proudman resonance is obtained theoretically for a flat bathymetry. However, in some places, it may be more realistic to consider the bathymetry as a slope linearly growing from the ocean to the coast. In these cases the *shallow water* equation will have as solution waves, called edge wave, that propagate in parallel to the coast. The energy of these waves is confined near the coast by reflection and its amplitude can be neglected far from the coast, at a distance higher than $\lambda/2\pi$ (λ stands for the wavelength of the wave). The edge waves will have the following dispersion relation (Ursell and Taylor, 1952):

$$c_n = \frac{gT}{2\pi} \tan \left[\beta(2n+1) \right], \tag{2.22}$$

where T is the period of the propagating wave, β is the slope of the bathymetry, and n is the wave mode. Then, similarly to the Proudman resonance, an edge wave that has the same phase velocity than the atmospheric perturbation is amplified (Greenspan, 1956).

This kind of resonance has been found to be very important in reported meteotsunami events, such as the particular case of the sea level oscillation of 1.5 m reported in Chicago on 6 June 1954. The sea level wave amplification was associated to Greenspan resonance, since the observed atmospheric pressure perturbation travelled with a speed of 22 m/s with direction parallel to the coast of the Michigan Lake; this speed and direction match the wave velocity of the observed edge wave mode with period of 110 min (Donn and Ewing, 1956). Later, it was proven by Bechle and Wu (2014), using numerical models, that both Proudman and Greenspan resonance were responsible for that meteotsunami. The same combination of resonance factors has been observed in others basins of the world ocean (Vilibić and Šepić, 2009), which indicates that both mechanisms can act together to amplify the meteotsunami waves.

For the Balearic Islands, the influence of this resonant mechanism has not been explored in detail. However, in Ličer et al. (2017), the meteotsunami waves that they simulated propagate as edge wave in parallel to the coast along the northern and southern Mallorca shelves, implying that the occurrence of Greenspan resonance between the edge waves and the atmospheric perturbation would be relevant on those zones. They also noted that the convergence of these waves in the Menorca Channel contributes to increase the sea wave height. Liu et al. (2002) compared sea level observations in Ciutadella with an analytical analysis of the edge waves around the Balearic Islands and suggested the existence of two modes with periods of 32 and 24 min propagating around the Balearic Islands. More research is needed in this field. The use of sea level measurements at different points of the Balearic basin should help to identify any existent edge wave propagating along the Balearic coast.

2.2.2 Coastal amplification

The effects of open sea resonance are key to explain the final meteotsunami wave. However, according to different numerical studies (e.g., Hibiya and Kajiura (1982); Vilibić

et al. (2008); Šepić et al. (2015)), the amplification of the sea waves at open sea, mainly by Proudman resonance, produce amplifications of factor 4 to 10. With initial pressure jumps of between 2 and 7 hPa the sea wave that hits the coast has, even in extreme events of maximum open sea amplification, an amplitude shorter than a meter. Consequently, to justify the severe meteotsunamis of several meters, we need to include to the meteotsunami generation some other amplification mechanisms related to the topographical conditions near the coast.

A. Shelf resonance

In a shelf compressed between a coast and a deep ocean, waves coming from the ocean can propagate to the coast and get reflected back to the ocean, but the change in wave velocity from the shelf to the ocean causes the reflection of the wave back to the shelf, trapping the wave within it (Vennell, 2007). When the interference between waves in the shelf is constructive, it may lead to important wave height increase that affects the coast.

According to Buchwald and de Szoeke (1973) the waves with phase velocity that fulfil,

$$\sqrt{gh_1} < c < \sqrt{gh_2} \tag{2.23}$$

where h_1 and h_2 are the shelf and the ocean depth, respectively, are trapped within the shelf. That relation has been obtained from considering a rectangular shelf of length L and constant depth. Then, the dispersion relation from the waves that propagate in that shelf is (Tintoré et al., 1988):

$$\frac{h_1}{h_2} \tan \left(L\sqrt{\frac{\omega^2}{gh_1} - k^2} \right) = \sqrt{\frac{k^2 - \omega^2/gh_2}{\omega^2/gh_1 - k^2}}, \tag{2.24}$$

where k is the wave number and $\omega = \frac{2\pi}{T}$ the angular frequency of the trapped wave. In Tintoré et al. (1988), it is obtained that the trapped waves in the Balearic shelf have a period similar to the normal mode in Ciutadella Harbour (10 min). They conclude, then, that shelf resonance may be a factor of amplification that contributes to the meteotsunami generation in Ciutadella. Further research is needed to determine the importance of the shelf resonance in the Balearic basin. The analysis of meteotsunamis in different ports that share the same outer continental shelf could provide more information on the amplification of shelf modes.

B. Wave shoaling

One of the effects of the wave approaching to the coast, when the water depth decreases, is the wave shoaling as a consequence of the reduction in propagation velocity when decreasing the sea depth. Thus, in order to preserve the wave energy, the wave height will increase following the so-called Green's Law (Green, 1838):

$$h_1 \sqrt[4]{H_1} = h_2 \sqrt[4]{H_2}, \tag{2.25}$$

where H_i denotes the water depth and h_i the wave height in the region i. In the particular case of Ciutadella the water depth goes from 80-120 meters within the Menorca channel to 5 meters depth in the harbour with is traduced in a factor of amplification ~ 2. Nevertheless, in the case of semi-closed harbours and inlets the most relevant amplification mechanism is the amplification produced by the constructive interference between the waves trapped in these basins, this phenomenon is called harbour resonance.

C. Harbour resonance

In coastal regions, seiches are a very important phenomenon. They are long-period standing sea level oscillations in an enclosed basin or a local part of a basin (Rabinovich et al., 2009). Depending on its particular geometry, each basin will have a particular set of eigen periods and modal structures which are independent of the external forcing. Harbour oscillations are considered a particular kind of seiches occurring in enclosed basins with one or more connections to the open sea, that are forced by external energy. The most important mode in a harbour oscillation is the lowest one, called *Helmholtz mode* or normal mode, which is a particular characteristic of each harbour. According to Rabinovich et al. (2009) it can be computed analytically for basins with simple geometry, being the simplest case a 1D port with length L and constant depth, H, where the eigen periods can be computed as:

$$T_n = \frac{4L}{(2n + 1)\sqrt{gH}}, \quad \text{where} \quad n = 0, 1, 2, ... \tag{2.26}$$

being the normal mode $T_0 = \frac{4L}{\sqrt{gH}}$. In the particular case of Ciutadella Harbour, it is a very long and narrow inlet that could be idealized as a 1D harbour with $L = 1.1$ km in the longitudinal dimension and $H = 5$ m. Then, the obtained *Helmholtz* period is $T_0 = 10.47$ min with matches the frequency peak obtained in sea level observations (see Fig. 3.5). In port and harbours with more complex geometries, it will be hard to compute analytically the eigen modes, but we can know their frequency response with in-situ measurements (Fig. 3.5 shows the measured spectral response for different Balearic harbours).

We need from an external forcing to excite the harbour oscillations. Then, the eigen modes of the basin will be amplified depending on its *amplification factor*:

$$H^2(f) = \frac{1}{(1 - f/f_0)^2 + Q^{-2}(f/f_0)^2}, \tag{2.27}$$

where f is the frequency of the arriving wave, f_0 is the frequency of the harbour normal mode, and Q is called quality factor (Q-factor). The Q-factor is a measure of the energy dumping produced by harbour resonance, and it depends on the characteristics of the basin. When the frequency of the incoming waves matches the normal frequency of the harbour, the power amplification is equal to Q^2 and it is maximum. It is important to note that Eq. 2.27 is an idealization of the harbour response for harbours with very simple geometry and high Q-factor; real semi-closed basins will have more complex response with several spectral energy peaks (examples in Fig. 3.5).

Then, the Q-factor of a harbour is a key parameter to determine how important will be the seiches there. For Ciutadella Harbour, Q has been estimated to be close to 10, which means that an arriving wave at the normal mode of the port, i.e. 10.5 min, with a wave height of 10 cm will reach 1 m of amplitude at the end of the port (Rabinovich et al., 1999). The Q-factor can be estimated from observations or from numerical experiments. If we can measure the spectral natural response of a harbour, assuming $Q \gg 1$, we can compute the Q-factor by using the following equation, provided in Miles and Munk (1961):

$$Q = \frac{f_0}{f_{1/2}^+ - f_{1/2}^-}, \tag{2.28}$$

where f_0 is the frequency of the normal mode and $f_{1/2}$ denotes the frequency at which the spectral power has decayed to half of its value at f_0.

The main source of energy dissipation in semi-closed basin oscillation is radiation through the harbour mouth. This leads to a paradox introduced by Miles and Munk (1961) because a small harbour opening would limit the energy lose, leading to high Q-factors. On the other side, a narrow entrance may limit the amount of entering energy, which leads to the need for some time ($\sim \frac{Q}{\pi}$ cycles) of forcing to reach the maximum amplification.

All in all, this amplification mechanism explains the large sea level oscillation measured in harbours as Ciutadella. Combining the effects of Proudman resonance (amplification factor 4-10), the wave shoaling (amplification factor ~ 2) and the harbour resonance with $Q \sim 10$ it is feasible that an atmospheric perturbation of 2-5 hPa of amplitude could cause meteotsunamis of the order of meters in Ciutadella. However, it is hard to quantify the total contribution of each one of the different amplification mechanisms to the final meteotsunami amplitude since the introduced mechanisms are explained from simplified models that are very far from the complexity of the real atmospheric forcings or of the coastal topographical characteristics. Therefore, there are still research gaps that should be tackled if we want to comprehend all the features concerning the meteotsunami generation.

2.3   Research gaps

Once we have introduced the reader into the state of the art of the literature concerning the meteotsunami generation mechanisms, we should point towards the unanswered questions that remain unsolved and that are worth to investigate to provide new knowledge to meteotsunami science. From the literature revised to complete this section, we have identified the following points as unclear issues that should be tackled in further research:

- Most of current studies are based on single events occurring in a particular basin. With the current data sets of sea level observations, that last for several years in some locations, a statistical study could be done with the aim of outlining the climatology, seasonality and connection to atmospheric patterns of the registered meteotsunami events.

- A first approach in quantifying the relationship between the synoptic pattern atmospheric was made by Šepić et al. (2016) for the meteotsunamis in Ciutadella, by creating an index derived from key synoptic parameters from ERA5 reanalysis. Similar studies can be extrapolated to other ports and basins. It also would be interesting to include mesoscale parameters that could be obtained from the vertical atmospheric profiles obtained by soundings.

- Most meteotsunamis in the Balearic Islands are associated to the creation of a wave duct (Vilibić et al., 2020) that allows the propagation of atmospherical gravity waves and atmospheric perturbations. However, meteotsunamis have been also observed simultaneously to the pass of convective systems (Jansa et al., 2007; Jansà and Ramis, 2021). It is worth to clarify which mechanism is the dominant one to allow the propagation of atmospheric perturbations. Jansà and Ramis (2021) also point towards the need of performing an historical review of the meteotsunamis in the Balearic Islands classifying the events depending on their atmospherical origin, waves train or convective jump, in order to discern if there is any relation between the meteotsunami amplitude and its atmospherical source. This task would not

be easy since the atmospheric origin of meteotsunamis is difficult to discern from observational data and the use of numerical high-resolution simulations would need from an important computational effort.

- Orography is known for its key role in mesoscale atmospheric processes. Belušić et al. (2007) suggest that the atmospheric perturbation responsible for causing a meteotsunami at the east Adriatic on 26-27 June 2003 was generated by the Alps orography. The mechanism triggering the atmospheric perturbations in the Balearic Islands is still unclear.

- Some important questions still remain unsolved concerning the relationship between atmospheric perturbation parameters, as its velocity and spectrum, and the final meteotsunami amplitude. The effect of these parameters have been tested by using numerical experiments that, for instance, relate the perturbation velocity to the produced sea wave amplification (Vilibić et al., 2008; Ličer et al., 2017). The comparison of their results with observed meteotsunami events would validate that results or point towards the weaknesses of the established amplification mechanism.

- Similarly, the meteotsunami wave propagation has been better understood in the past years thanks to numerical studies (Ličer et al., 2017). However, the lack of observational data with high spatial density has not allowed the complete validation of those results which are based on idealized considerations. The contribution from other amplification mechanisms besides than the Proudman resonance, as the Greenspan and shelf resonances, should also be investigated for meteotsunamis in the Balearic Islands.

- The understanding of past meteotsunamis will allow us to estimate the role of this hazard in the future climate. A first approach to project the future occurrence of meteotsunamis was made by Vilibić et al. (2018) using the index developed by Šepić et al. (2016), which relates the synoptic pattern to the sea level oscillation in Ciutadella. Similar methods could be used to predict the occurrence of meteotsunamis in the future climate on other regions of the world.

- Finally, as it has been introduced in Sect. 1.1.2, an exhaustive review of the current meteotsunami forecasting systems should be done to identify their strengths and weaknesses. All, with the aim of increasing the reliability of their predictions.

In order to investigate these suggested topics it is necessary to increase the available observations of sea level and atmospheric pressure. Since meteotsunamis are small-scale and high-frequency processes, the high spatial and temporal resolution of the observations is critical in order to obtain useful information. It is also necessary to expand the number of available observations in the basins of high meteotsunami occurrence to map the sea level oscillations and the atmospheric pressure perturbation during these events. The combination of new data with the use of high-resolution numerical models to reproduce both, the atmospheric perturbation generation and the sea wave propagation and amplification, would be the way to deal with most of the outlined research gaps.

2.4   Objective of this work

The goal of this work is to take advantage of the new ultra-dense observational network to review the fulfilment of the established mechanisms for the generation of meteotsunamis in the Balearic Islands. To do so, we focus on a set of events occurring during May and June 2021. The analysis performed will be done just with observational data of atmospheric pressure and sea level. The aim will be to identify which of the conclusions outlined by the analytical and numerical models used in previous studies to explain the meteotsunami occurrence are consistent with the observations and which conclusions need from more investigation. We expect to identify some key features in the meteotsunami generation mechanism that motivate further research.

With the available observational data, we will report the atmospheric conditions, trying to infer the generation and propagation mechanism for each event. Then, the atmospheric perturbation will be characterized by means of spectral analysis and computing its propagation velocity (see Sect. 3.2 for details in the used data analysis methods). The obtained characteristics of the atmospheric perturbation will be compared with the amplitude of the meteotsunami in the different ports of the Balearic Islands with the aim of discerning the effect of the atmospheric parameters into the meteotsunami amplitude. Finally, the technique introduced by Rabinovich (1997) to estimate the external sea level forcing at ports and harbours will be tested with the aim of characterizing the open sea forcing.

A secondary goal of this work is to present, for the first time, sea level observations during meteotsunami events from some ports on the Balearic Islands that did not have a tide gauge installed before. Although, the focus will be mainly in Ciutadella Harbour, since it is the port with the largest meteotsunamis, a first overview on the occurrence of meteotsunamis in other ports will be done.

Chapter 3

Data and Methods

The data used to study the meteotsunami events in Chap. 4 will be presented in this chapter (Sect. 3.1) together with the methods used to describe the meteotsunami events (Sect. 3.2).

3.1 Observational data

The data traditionally used to study meteotsunamis are sea level and atmospheric pressure time series. The sea level measurements capture the rapid sea level oscillations that are the result of the amplification of the sea wave caused by a high frequency atmospheric perturbation, which can be measured by barographs. It is necessary to have high temporal resolution ($\Delta t \leq 1$ min) observations of these variables in order to characterize the meteotsunamis since we must be able to capture important oscillations with time scale between 5 and 120 min. To complement the direct observation of the meteotsunami effects, some other atmospheric variables can be used to study the origin of the atmospheric pressure perturbations as temperature and humidity from soundings or numerical reanalyses.

3.1.1 Sea level data

The sea level data is measured by tide gauges installed in different ports and harbours. Different governmental and scientific institutions have installed several tide gauges all around the Balearic Islands: Puertos del Estado (PdE) has deployed 5 tide gauges (Formentera, Eivissa, Palma, Alcúdia and Maó), the Balearic Island Coastal Observation and Forecasting System (SOCIB) has deployed 6 instruments (Sant Antoni, Sa Rapita, Andratx, Porto Cristo, Colonia de Sant Pere and Pollensa), the Spanish Institute of Oceanography (IEO) has one tide gauge at Palma, Ports de les Illes Balears has deployed a tide gauge within Ciutadella Harbour and the Instituto Geográfico Nacional (IGN) installed an instrument at Son Blanc dike near the entrance of Ciutadella Harbour. The location of all these devices has been plotted in the map of Fig. 3.1 (yellow triangles), and their characteristics are listed in Tab. 3.1.

This tide gauge network has been extended during 2020-2021 by the tide gauges installed by the project VENOM. The Spatial Variability of Sea Level in the Western Mediterranean (VENOM) project is being carried out by the Physics Department of the University of the Balearic Islands (UIB) and the Spanish Institute of Oceanography (IEO).
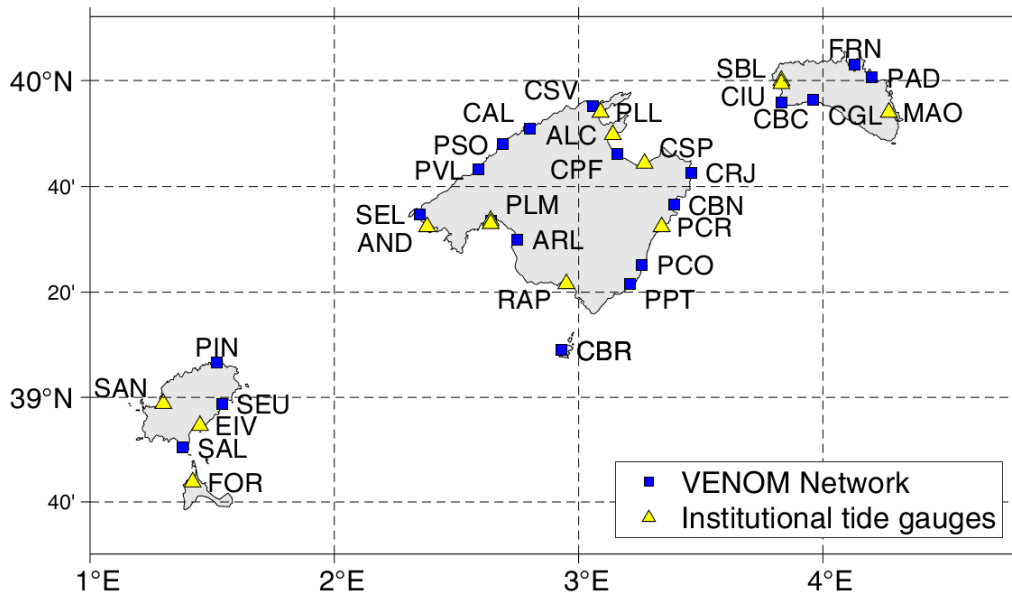
Figure 3.1: Map of all the tide gauges deployed in the Balearic Islands. Blue squares represent the VENOM instruments, and yellow triangles represent the instruments runned by other institutions. Every tide gauge is labelled with an identification code, the equivalence can be found in Tab. 3.1.

One of the goals of the project is to increase the spatial resolution of the sea level observing system existing in the Balearic Islands. With this aim, a new prototype of low-cost tide gauge has been developed and deployed along the Balearic coast.

A. The VENOM network

This new network has 21 tide gauges that have been mounted and deployed by the Sea Level and Climate research group of the UIB-IEO during 2020 and 2021. The goal was to build an ultra-dense network of sea level observations capable of capturing sea level processes with small spatial scales. Thus, the deployment of the network was planned to cover all the Balearic coast in an homogeneous way, with a maximum separation between instruments of 30 km.

Building this ultra-dense network with commercial devices (5000 - 10000€) would have required from a huge economic investment, therefore a new low-cost tide gauge was designed using the Arduino environment (https://www.arduino.cc). Arduino is a platform of electronic hardware and software that allows the development of simple and customizable electronic devices. The prototype consists of three main parts: an acoustic sensor that measures the vertical distance from the device to the sea water; a datalogger, formed by an Arduino Pro Mini microprocessor that reads the sensor output and saves 1 min averaged data into a micro-SD card; and a transmitter, built with the same Arduino microprocessor; and a cellular phone, that every 10 min sends an averaged sea level measurement which allows the remote monitoring of the performance of each instrument. All the system is powered by a 5000 mAh Lithium battery that is charged by a solar panel that provides autonomy to the whole device. The circuit board containing

all electronic components is stored in a watertight box that is mounted on a steel bar anchored to a dock at the deployment location. The sensor and solar panel are mounted out of the box, the first pointing vertically to the sea, and the second orientated to have the maximum exposition to solar light. In Fig. 3.2 we show two of the installed tide gauges, in Portocolom (PCO) and in Cabrera (CBR). In Tab. 3.1 all the 21 VENOM tide gauges installed are listed with its corresponded code, coordinates and deployment time. They are also plotted (blue squares) in Fig. 3.1.
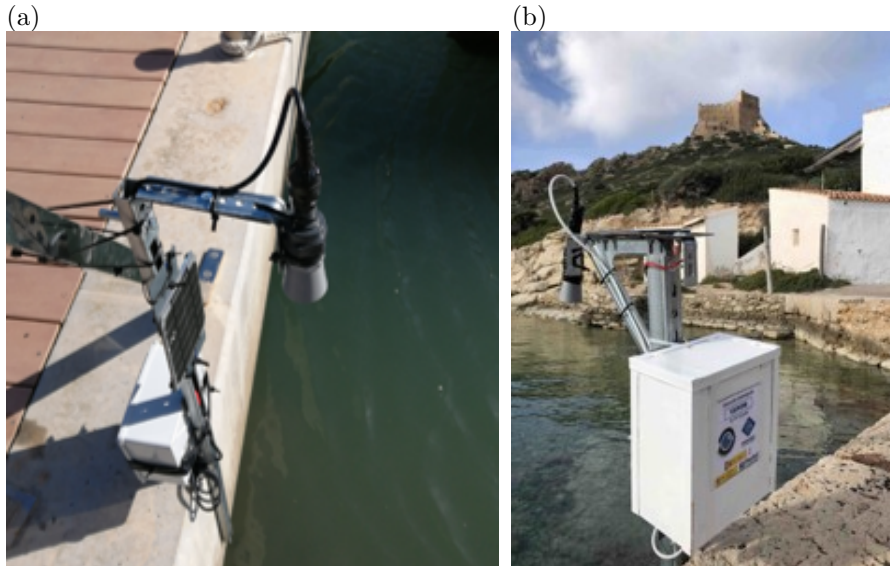

Figure 3.2: Images of VENOM tide gauges deployed at Portcolom (a) and Cabrera (b).

The prototype have suffered from several software and hardware updates since the first devices were installed, one of the advantages of the designed instrument is that all components are easy to replace and reuse allowing a constant improving at low cost. It has been estimated that the cost of all components necessary to build one of the VENOM tide gauges is of 300€. Additionally, the cost linked to the time required for the assembling of the devices and the maintenance of the network should be also considered, but in any case it is much lower than commercial instruments.

The performance of the new tide gauges has been tested by comparing the measurements of a VENOM device with the Puertos del Estado Palma tide gauge data, the instruments were located side by side. A correlation higher than 0.95 between the time series has been found, with a negligible RMSE of ~ 9 mm. These results confirm the good performance of the VENOM tide gauges.

3.1.2 Atmospheric pressure data

The atmospheric pressure data used in this work comes from the amateur meteorological network of BalearsMeteo (http://balearsmeteo.com/), that accounts 71 stations all over the Balearic Islands. The high number of meteorological stations allows us to have high spatial resolution measurements of the atmospheric pressure at surface levels. The data collected by these stations has been standardized and each station uploads its measurements to a common server every 10 seconds. Thus, we will use the atmospheric pressure measured by this dense barograph network with a very high temporal resolution (10 seconds of sampling period). The barographs have a resolution of 0.1 hPa.

Location	Code	Island	Institution	Lat.	Long.	Deployment date
Fornells	FRN	Menorca	VENOM	40.05	4.13	19/08/2020
Port d'Addaia	PAD	Menorca	VENOM	40.01	4.20	26/03/2021
Ciutadella	CIU	Menorca	PortsIB	40.00	3.83	N/A
Son Blanc	SBL	Menorca	IGN	39.99	3.83	23/10/2017
Cala Galdana	CGL	Menorca	VENOM	39.94	3.96	19/08/2020
Cala'n Bosch	CBC	Menorca	VENOM	39.93	3.83	25/03/2021
Maó	MAH	Menorca	PdE	39.90	4.27	02/11/2009
Cala Sant Vicens	CSV	Mallorca	VENOM	39.92	3.06	02/06/2021
Pollensa	PLL	Mallorca	SOCIB	39.90	3.09	01/07/2011
Sa Calobra	CAL	Mallorca	VENOM	39.85	2.80	07/02/2021
Alcúdia	ALC	Mallorca	PdE	39.83	3.14	14/09/2009
Port de Sóller	PSO	Mallorca	VENOM	39.80	2.69	19/06/2020
Can Picafort	CPF	Mallorca	VENOM	39.77	3.16	03/03/2021
Colonia de Sant Pere	CSP	Mallorca	SOCIB	39.74	3.27	28/10/2015
Port de Valldemossa	PVL	Mallorca	VENOM	39.72	2.59	09/07/2020
Cala Ratjada	CRJ	Mallorca	VENOM	39.71	3.46	11/03/2020
Cala Bona	CBN	Mallorca	VENOM	39.61	3.39	24/02/2021
Sant Elm	SEL	Mallorca	VENOM	39.58	2.35	09/07/2020
Palma	PLM	Mallorca	VENOM	39.56	2.64	21/01/2021
Palma	PLM	Mallorca	PdE	39.56	2.64	14/09/2009
Palma	PLM	Mallorca	IEO	39.55	2.64	1963
Andratx	AND	Mallorca	SOCIB	39.54	2.38	02/06/2011
Porto Cristo	PCR	Mallorca	SOCIB	39.54	3.34	16/02/2016
S'Arenal	ARL	Mallorca	VENOM	39.50	2.75	22/01/2021
Portocolom	PCO	Mallorca	VENOM	39.42	3.26	27/02/2020
Portopetro	PPT	Mallorca	VENOM	39.36	3.21	23/06/2020
Sa Rapita	RAP	Mallorca	SOCIB	39.36	2.95	05/05/2011
Cabrera (1)	CBR	Cabrera	VENOM	39.15	2.93	25/06/2020
Cabrera (2)	CBR	Cabrera	VENOM	39.15	2.93	12/11/2020
Portinatx	PIN	Eivissa	VENOM	39.11	1.52	28/06/2021
Santa Eulària	SEU	Eivissa	VENOM	38.98	1.54	10/03/2021
Sant Antoni	SAN	Eivissa	SOCIB	38.98	1.30	05/03/2015
Eivissa	EIV	Eivissa	PdE	38.91	1.45	01/01/2003
Ses Salines	SAL	Eivissa	VENOM	38.84	1.38	29/06/2021
Formentera	FOR	Formentera	PdE	38.73	1.42	28/09/2009

Table 3.1: List of the tide gauges deployed in the Balearic Islands.

Although the number of stations is very large, it is very usual that some of them have temporal measurement errors that have to be detected when processing the data. Then, the number of stations with usable data during the meteotsunami events will not be as large as the total number of stations but will allow a good mapping of the atmospheric pressure disturbance characteristics over the Balearic Islands. In Fig. 3.3 the locations of all the meteorological stations have been plotted. As it can be seen, most of the stations are located in Mallorca and, unfortunately, in Menorca there are only 2 stations.
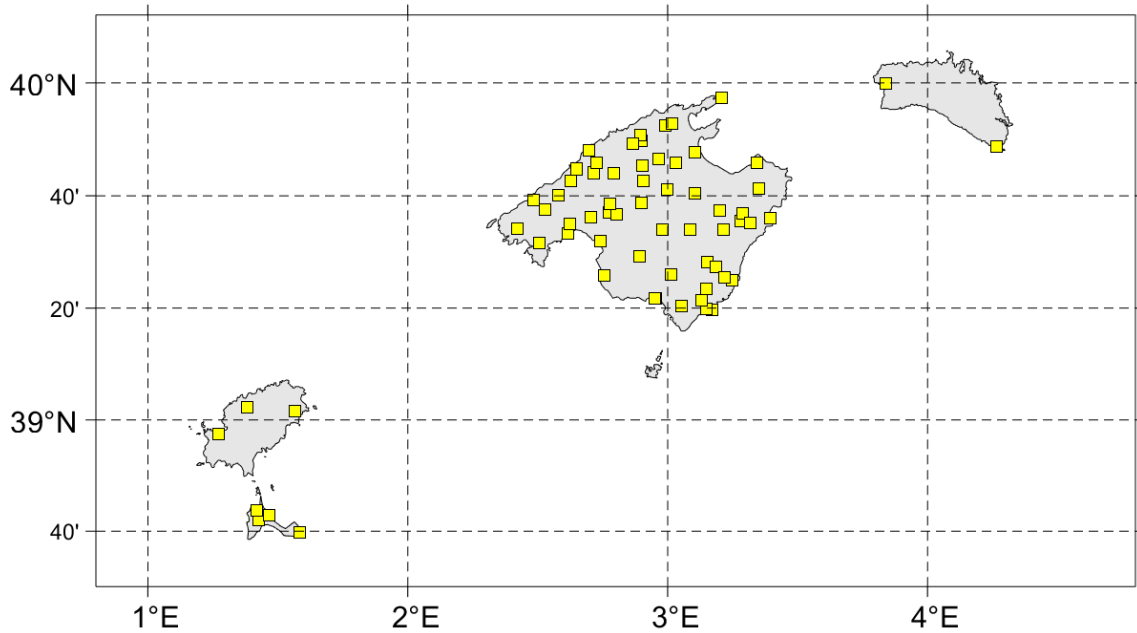
Figure 3.3: Map of all meteorological stations of the BalearsMeteo network.

3.1.3   Data processing

The data from VENOM tide gauges need from some quality control before its scientific use. In first place we have to take into account that the saved information is the distance between the acoustic sensor and the sea surface, thus, to obtain the sea level variation we must subtract the mean and invert the measurements because when the sea level rises the distance between the sea surface and the sensor decreases. A quality control is applied to all time series with the following steps:

i. Removing all point with values lower than a threshold, which indicates either mal-functioning or that something contaminated the measurement (e.g. boats anchored below the sensor).

ii. Remove outliers which deviate further than 6 σ from the whole time series.

iii. Remove outliers that deviate more than 3 σ using a moving averaging window of 3 hours over the sea level time series.

iv. Remove outliers that deviate more than 3 σ using a moving averaging window of 3 hours over the time derivative of sea level records.

The gaps in the time series are filled with NaNs (Not a Number) to have the same time vector, with 1 minute sampling rate, for all observed time series. The data from the institutional tide gauges does not need the application of this quality control since quality control has been previously applied by the institutions running the devices. The same time vector is used for the VENOM and institutional tide gauges data.

The same data processing steps applied to the sea level time series from VENOM tide gauges are used with the atmospheric pressure time series from the BalearsMeteo stations. Then, the time series will be used to study the meteotsunami events and, if any tide gauge or barograph station have more than a 5% of NaNs during the meteotsunami

time interval, it is not taken into account for the study of that event. Finally, gaps shorter than 3 min in the time series are filled with an autoregressive fit.

3.1.4   ERA5 Reanalysis

To study the atmospheric conditions beyond the surface pressure during the meteotsunami events reported here we use the ERA5 reanalysis. This product is constructed by assimilating all the *a posteriori* available observational data into a numerical atmospheric model with hourly outputs to obtain the best possible estimation for the atmospheric state. The reanalysis is obtained by using a 4D-Var assimilation method in combination with a numerical forecast model of the European Center for Medium-Range Weather Forecasting (ECMWF). It provides the atmospheric state variables in 37 pressure levels and other 2D variables at single levels, as for example the atmospheric pressure at sea level. The fields have constant spatial resolution of 0.25°of latitude and longitude, which is a resolution around 30 km in linear distance in our spatial domain.

This reconstructed atmospheric states reproduce correctly the synoptic scale but, due to that it lacks the spatial and temporal resolution required, they cannot resolve the smaller scale processes which are determinant to the formation of meteotsunamis. In Fig. 3.4 we compare a vertical profile measured by a sounding at Palma with the vertical atmospheric profile provided by ERA5 at its closer grid point for 18 July 2018 at 0000 UTC. We can see that the agreement between the measurements and reanalysis is very high, specially in temperature and at upper levels (above 500 hPa). In temperature, we see that the sounding measures a larger gradient of temperature between 900 and 850 hPa. This difference is small but may affect the stability of that layer which is a key parameter to the formation of a wave duct, as has been introduced in Sect. 2.1.2. The differences in wind speed and direction are also larger in the lower levels than in the upper ones, but the shape of the profile is very similar. Unfortunately, we do not have access to soundings measured during the meteotsunami events reported here, which would allowed us to compare the relevance of these differences between ERA5 reanalysis and sounding data during meteotsunami events.

3.2   Methods

In this section the data processing methods that have been used to study the meteotsunami events are described in detail.

3.2.1   Spectral analysis tools

The goal of spectral analysis is to separate the contribution of each frequency to the total variance of a time series. To do it we use the following tools that allow us to quantify the spectral power of the signal:

A. Welch Periodogram

The most common tool to analyse the spectral energy of a signal is the *periodogram*, which is an estimation of the Power Spectral Density (PSD) of the time series, understanding power as the energy per unit time. The simplest way to compute the periodogram of a signal y_n with N samples taken at time t_n, $n \in [0, N-1]$, being $t_n = t_0 + n\Delta t$ (Δt
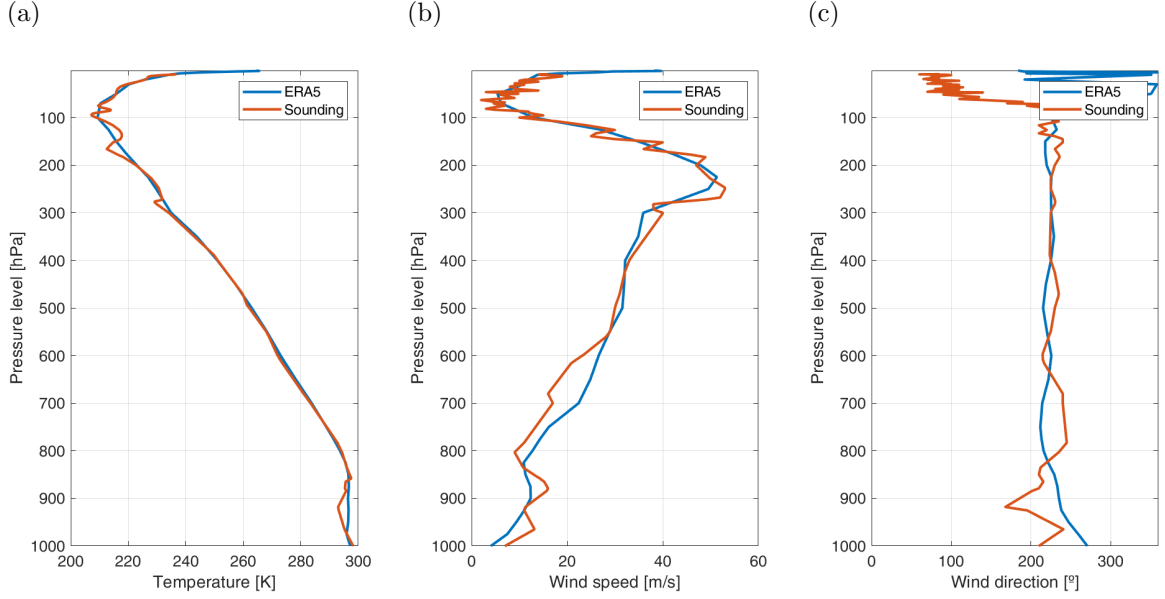
Figure 3.4: Comparison of ERA5 vertical profiles with observations from a sounding: (a) Temperature, (b) wind speed and (c) wind direction. The sounding was launched from Palma at 0000 UTC 16 July 2018 and the ERA5 profile has been taken from the closest grid point at the same time.

is the sampling period) is applying the following equation, that computes the *one-sided* periodogram:

$$G(f_k) = \frac{2}{N\Delta t}\left|\sum_{n=0}^{N-1} y_n e^{-2\pi i f_k t_n}\right|^2, \tag{3.1}$$

where $f_k = \frac{k}{N\Delta t}$, with $k = 0, 1, \ldots, \frac{N}{2}$, are the frequencies that we can sample. The maximum frequency that we can represent in the periodogram is called Nysquist frequency and depends on the sampling period, $f_N = \frac{1}{2\Delta t}$, and the frequency resolution depends on the length of the measured time series, $\Delta f = \frac{1}{N\Delta t}$. Then, in the case of meteotsunamis we want to study a phenomenon with time scales that go from 5 min to a couple of hours, so we must choose a sampling period that fulfils $f_N > \frac{1}{2 \cdot 5 min}$. That is why the sampling period of 1 min of our sea level time series is appropriate. From Eq. 3.1, we can see that the periodogram is proportional to the squared absolute value of the discrete Fourier transform of the signal $y(t)$. Thus, the Fast Fourier Transform algorithms allow us to reduce the computational cost of this computation (Emery and Thomson, 2001).

The way of computing the periodogram presented in Eq. 3.1 may result in some problems. In the first place, the fact that the time series is finite acts negatively on the estimated PSD since the time series is confined in a finite period of time which is the same that saying that it has been multiplied by a rectangular box car function ($w(t) = 1$ within the time interval, $w(t) = 0$ otherwise); this phenomenon is called windowing. This multiplication by a box car function in the time space results in a convolution product by a *sinc* function in the Fourier space, which causes an important leakage of energy from peaks in the PSD to its nearby frequencies. To reduce the effects of this windowing, we can change the box car function to another *window* that reduces the energy leakage of the spectral peaks. We will use a Keiser-Bessel window which according to Emery and Thomson (2001) is the *top performer* window.

31

The second problem is the small statistical significance of each of the spectral estimations $G(f_k)$ since each spectral sample can be considered as a random variable with a chi-squared probability function with only two degrees of freedom (ν=DoF). To increase the statistical significance of the obtained spectrum we can increase the DoFs by using the Welch technique to average the periodogram by blocks (Welch, 1967). We divide the time series in blocks of 512 min ($N = 512$) that overlap with the 50% of the points of the previous block; a Keiser-Bessel window is applied to every block and the periodogram of every block is computed using Eq. 3.1. Finally, the obtained periodograms are averaged to obtain our estimation of the PSD with high statistical significance. The result of this process is still noisy in high frequencies, reason why, we apply a logarithmic averaging window that is larger in the higher frequencies than in the lower ones.

The detailed Welch periodogram will be used to compute the spectra of sea level time series and to apply the forcing estimation technique detailed in Sect. 3.2.2.

B. Wavelet power spectrum

The Welch periodogram computes the average PSD of a whole time series, so it assumes that the energetic content of each frequency does not change with time. If we want to compute the spectral energy of a non-stationary time series there are better tools as the *wavelet power spectrum*. The information and the codes used for the computations of the wavelet power spectra and its related products has been obtained from the work of Torrence and Compo (1998).

The wavelet transform consists on computing the convolution of our time series by a *mother* wavelet function. In our case we will choose a Morlet wavelet function as this *mother* wavelet:

$$g(t) = \pi^{-1/4} e^{-t^2/2} e^{i\omega_0 t}, \tag{3.2}$$

where ω_0 is a non-dimensional frequency chosen to be 6. Then the wavelet transform can be written as:

$$W(a,\tau) = \frac{1}{\sqrt{a}} \sum_{n=0}^{N-1} y(t_n) g^* \left(\frac{t_n - \tau}{a} \right) \tag{3.3}$$

where the index (*) indicates the complex conjugate, τ is the time when the wavelet is centred, and a is a parameter, called scale, related to the period of the oscillations of the wavelet function.

With the aim of reducing the computational cost, the algorithm that computes the wavelet transform does the computation in the Fourier space to avoid the convolution product present in Eq. 3.3. In the Fourier space, the wavelet transform is written as:

$$W(a,\tau) = \frac{1}{\sqrt{a}} \sum_{k=0}^{N-1} Y(\omega_k) G^*(a\omega_k) e^{i\omega_k \tau} \tag{3.4}$$

where $\omega_k = 2\pi f_k$. Finally, we can compute the wavelet power spectrum as $|W(a,\tau)|^2$, which is proportional to the spectral energy as function of time and frequency. The parameter a can be related to the oscillation period at the Fourier space by the following expression:

$$T_j = \frac{4\pi a_j}{\omega_0 + \sqrt{2 + \omega_0^2}} \tag{3.5}$$

where a_j represents the discretization of the scale a used in the computation of the wavelet power spectrum. For convenience, the discretization of the scales is done as fractional powers of two:

$$a_j = a_0 2^{j\Delta j}, \quad j = 0, 1, \ldots, J, \tag{3.6}$$

where we have used $a_0 = 2\Delta t$, $\delta j = 1/12$ and $J = 96$.

Finally, in the wavelet power spectra presented in this work we have marked with a black contour (e.g. Fig. 4.4) the 95% percent significance level for a red noise, i.e., the power spectral energy above that level is, with a 95% certainty, result of the signal and not part of a background red noise.

C. Digital filter

As it has been introduced previously, we are interested in high frequency (5 - 120 min) sea level and atmospheric pressure oscillations. Consequently, we will use digital filters to remove from the signals the frequencies that are not of our interest as, for example, the tidal oscillations of the sea level and the synoptic scale cyclones and anticyclones of the atmospheric pressure. We have chosen a second order Butterworth filter to do this task. According to Emery and Thomson (2001), this filter is optimal for this task since it has a flat transfer function in the pass band, i.e. it does not change the amplitude of the passing frequencies, and it has a zero phase shift, i.e., the phase is also left untouched for the passing frequencies.

All time series presented in this work will be low-pass filtered to remove the energy content below 2 min to avoid high-frequency noise and 3 hour high-pass filtered to avoid the mentioned large-scale processes.

3.2.2 External forcing estimation method

Rabinovich (1997) introduced a method to estimate the spectral power of the sea level forcing at the entrance of a harbour. He considered that the observed spectrum in a harbour during a tsunami (or meteotsunami) event $S_{obs}(f)$ was the sum of the spectrum of the external forcing $S_f(f)$ plus the spectrum of some background oscillations $S_b(f)$:

$$S_{obs}(f) = S_f(f) + S_b(f). \tag{3.7}$$

Thus, if we assume that the topographic response $A(f)$ is linear, i.e. it only depends on the spectral distribution of the energy but not on its amplitude, we can write:

$$S_f(f) = A(f)E_f(f), \tag{3.8}$$
$$S_b(f) = A(f)E_b(f), \tag{3.9}$$

where $E_f(f)$ and $E_b(f)$ are the external forcing causing the event and the background forcing respectively. Then, we can define the spectral ratio $R(f)$ as the ratio between the observed spectrum and the background spectrum:

$$R(f) = \frac{S_{obs}(f)}{S_b(f)} = \frac{E_f(f)}{E_b(f)} + 1. \tag{3.10}$$

Thus, assuming that $E_b(f)$ is stationary, the spectral ratio $R(f)$ is a measure of the spectral power distribution of the forcing. This technique was applied by Monserrat et al.

(1998) and Marcos et al. (2009) to estimate the forcing energy during meteotsunami events at Ciutadella and other close locations and they concluded that during the events nearby tide gauges should provide very similar spectral ratios.

To properly apply this technique (from now on it will be called *background technique*) during meteotsunami events, first, we should find a good background spectrum for each of the tide gauges that we have. In Rabinovich (1997) the background spectrum is computed from time intervals when the observed sea level oscillations are weak. To select this weak oscillation intervals, we will compute the variance of the time series in 1 day averaging windows that will be displaced six hours each step. From the obtained variances we will choose the 10 days with smaller variance to compute the spectrum for each 1 day interval. The obtained spectrum has been computed with the Welch periodogram method detailed in Sect. 3.2.1 and each of them has between 80 DoFs at low frequency and 1040 at high frequency. Finally, we will average the 10 spectra obtaining the background spectrum for each tide gauge which will be stored and used to estimate the spectral ratio during meteotsunami events.
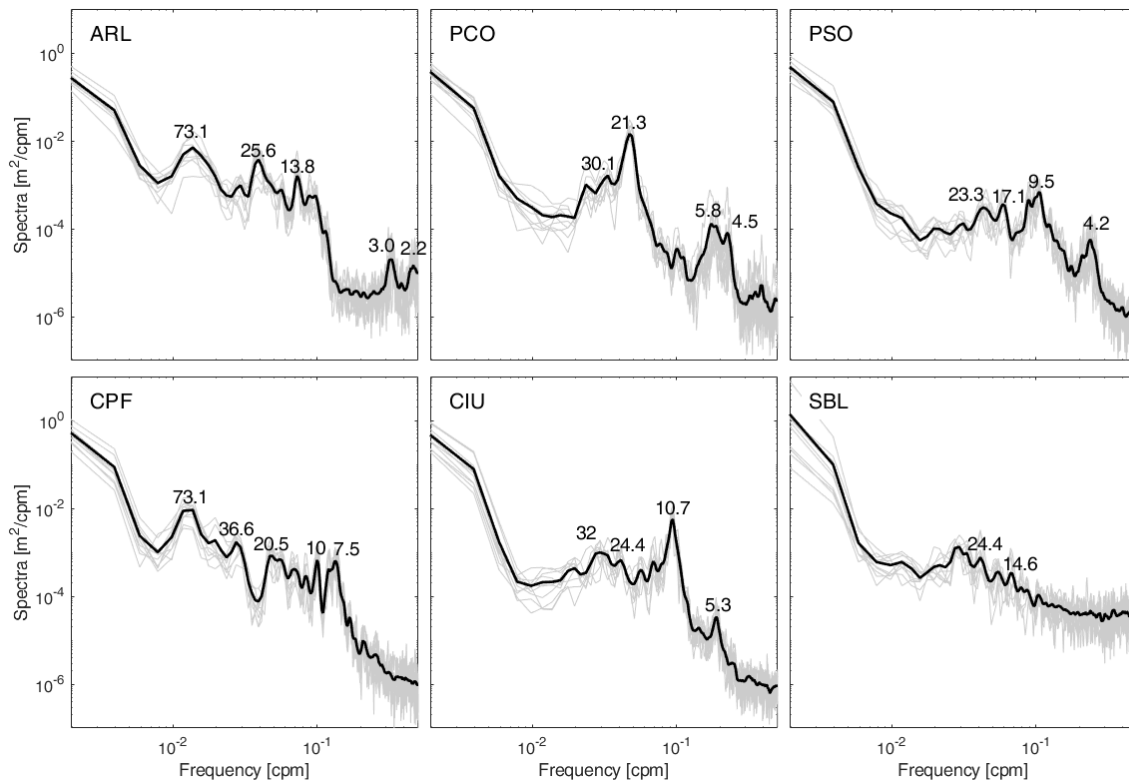

Figure 3.5: Background spectra estimated at different tide gauges (left to right and top to bottom): S'Arenal (ARL), Portocolom (PCO), Port de Sóller (PSO), Can Picafort (CPF), Ciutadella (CIU) and Son Blanc (SBL). The averaged background spectra are plotted in black solid lines and the 10 one-day spectra used to compute them are plotted in grey. The period of the most relevant spectral peaks is written in minutes.

Some estimated background spectra have been plotted in Fig. 3.5. The difference between the topographical response of the different ports can be observed: the naturals modes of PCO, PSO and CIU stand out at 21.3 min, 9.5 min and 10.7 min period, respectively; ARL and CPF have their energy distributed through several peaks; and SBL has a very weak spectral response. The variability of the estimated backgrounds spectra can be observed from the averaged 1 day spectra, plotted in grey.

34

3.2.3 Perturbation velocity estimation

We will use the atmospheric pressure measurements to estimate the propagation speed and direction of the atmospheric perturbations that cause the reported meteotsunami events. To do this, we will use the algorithm suggested by Orlic (1980) that used a cost function that provide a good estimation of the speed and direction of propagation of the atmospheric perturbation.

First, we must define the velocity vector of the perturbation as:

$$\vec{v} = (c\cos(\gamma), c\sin(\gamma)), \tag{3.11}$$

where c is the speed of the perturbation, and γ the angle between the velocity vector and the parallels (lines of constant latitude). Thus, for every couple of stations, denoted by the subindex i, we can define: Δt_i as the time that the perturbation takes to go from one station to the other; d_i, as the distance between the stations; and γ_i as the angle between the line connecting both stations and the parallels. In Fig. 3.6 a diagram of the described system is represented. d_i is computed as the length of the arc between the location of both stations, given in longitude-latitude coordinates (λ, longitude; ϕ, latitude). Then γ_i will be computed as follows:

$$\gamma_i = \arctan\left(\frac{\phi_{i,1} - \phi_{i,2}}{\cos(\phi_{i,1})(\lambda_{i,1} - \lambda_{i,2})}\right), \tag{3.12}$$

where we have used as projection over the x axis (west to east) $R_T\cos(\phi_{i,1})(\lambda_{i,1} - \lambda_{i,2})$, and over the y axis (south to north) $R_T(\phi_{i,1} - \phi_{i,2})$. Now, we can define the time that the perturbation needs to travel between the two stations as:

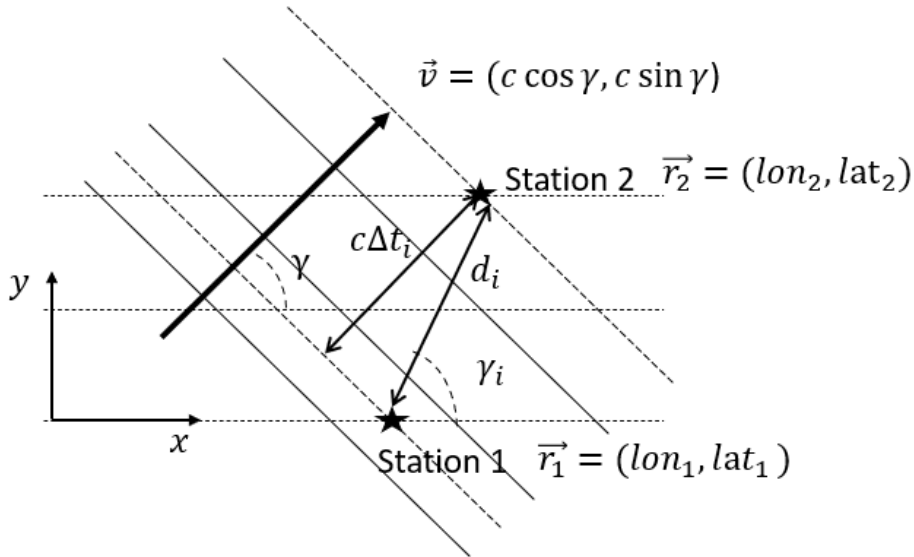$$\Delta t_i = \frac{d_i\cos(\gamma_i - \gamma)}{c}. \tag{3.13}$$

Figure 3.6: Diagram of the atmospheric disturbance propagation speed and direction estimation problem.

Finally, we need a way to measure the time that the perturbation needs to travel from one station to the other. To do it we will use the correlation between filtered atmospheric pressure time series $y_{i,1}$ and $y_{i,2}$:

$$\rho_{Y_{i,1},Y_{i,2}}(n) = \frac{\sum_{j=1}^{N-n}(y_{i,1_j} - \bar{y}_{i,1})(y_{i,2_{j+n}} - \bar{y}_{i,2})}{\sigma_{y_{i,1}}\sigma_{y_{i,2}}}, \tag{3.14}$$

where n is the temporal displacement, in number of points, between the two time series, and σ_y stands for the standard deviation of the time series. Then, we will define $\tilde{\Delta}t_i$ as the time displacement that presents a higher correlation between time series and ρ_i as the maximum correlation. From now on, $\tilde{\Delta}t_i$ is defined as the measured time lapse that the perturbation took when travelling between the two stations of the pair i.

Thus, we will minimize the following cost function to estimate the speed and the direction of propagation of the atmospheric perturbation:

$$f(c,\gamma) = \sum_{i=1}^{N_p} A_{\rho_i}\left(\frac{d_i\cos(\gamma_i - \gamma)}{c} - \bar{\Delta}t_i\right)^2, \tag{3.15}$$

where N_p is the number of station pairs that we use and A_{ρ_i} is a weight function assigned to each couple of stations as a function of the maximum value of the correlation between their time series. A_{ρ_i} is chosen arbitrarily as a Gaussian function centred at 1,

$$A_{\rho_i} = e^{-2\frac{(1-\rho_i)^2}{\sigma_\rho^2}}, \tag{3.16}$$

where ρ_i is the maximum value of the correlation function between the time series of atmospheric pressure of the couple of stations i, and σ_ρ is a parameter that modulates the width of the Gaussian. The weight function A_{ρ_i} is used to prioritize those couples of stations with high correlation between time series over those uncorrelated. After some test we have chosen $\sigma_\rho = 0.1$ since it has provided the most plausible results.

Finally, a Nelder-Mead optimization algorithm (Lagarias et al., 1998) is used to minimize the cost function of Eq. 3.15 providing the estimations of c and γ.

This algorithm may be applied to the measured time series in very different ways. In this work we are interested on studying the time evolution of the atmospheric perturbation, reason why, we will compute the propagation velocity every 10 min. At each time step, we will use time series of 2 hours around the central time. Furthermore, an estimation of the velocity will be provided for each meteorological station since only the stations at a distance shorter than 20 km will be used to avoid lower correlation coefficients between stations that are far apart. In Fig. 3.7 the estimated propagation velocity at each station has been plotted for Mallorca stations for two different instants during the meteotsunami event of 23 May 2021: Fig. 3.7a at 1200 UTC and Fig. 3.7b at 2300 UTC. In the figures it can be seen that at the same time most stations present very similar estimations of the speed and direction. However, larger difference is appreciated between the velocities estimated at different times. More results of perturbation propagation velocities estimates will be provided in Chap. 4.
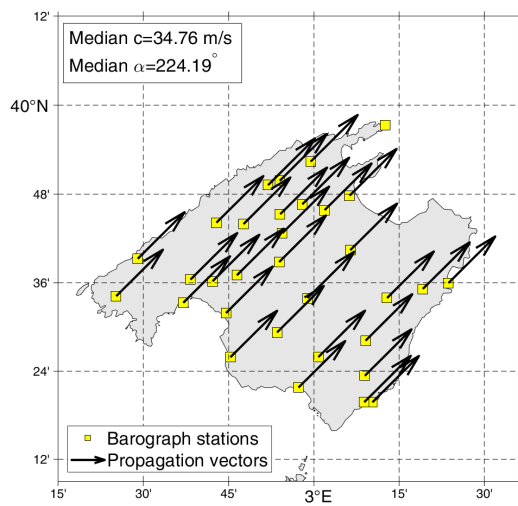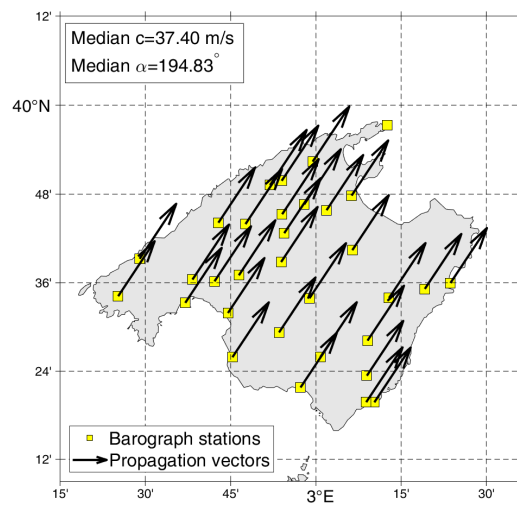
Figure 3.7: Map of the propagation velocity estimated at each BalearsMeteo stations over Mallorca. The median in speed and direction are written in the legend. (a) 1200 UTC 23 May 2021, (b) 2300 UTC 23 May 2021.

Chapter 4

Results

In the following chapter, the most relevant results for the meteotsunami events occurred during May-June 2021 will be provided (Fig. 4.1). The goal is to describe qualitatively the events using observational data from VENOM and Balearsmeteo networks, together with data coming from other institutional sources. As it has been introduced in Chap. 3, the use of these data offers an unprecedented opportunity to study meteotsunamis with high spatial and temporal resolution observations. First, the 23-24 May 2021 event will be analysed in detail using the tools presented in Chap. 3, then some remarks on other meteotsunami events registered during May-June 2021 will be given.
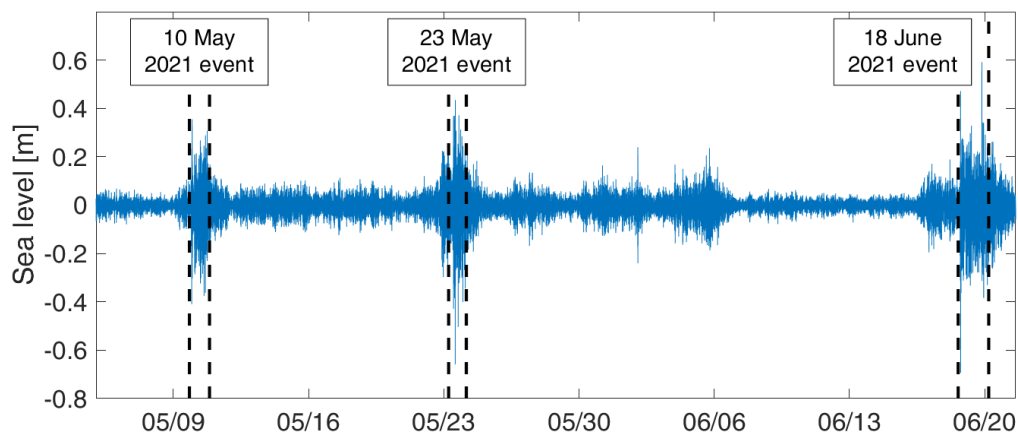

Figure 4.1: Sea level time series (m) measured in Ciutadella between 5 May 2021 and 21 June 2021. The meteotsunami events described in this chapter are delimited with dashed black lines.

4.1 Meteotsunami event: 23 May 2021

Between 0700 UTC 23 May and 0300 UTC 24 May 2021 important sea level oscillations were measured by several tide gauges along the Balearic Islands coast. Ciutadella (CIU) registered the maximum oscillation of 108 cm (trough-to-crest). Other important oscillations were registered in other harbours from the Balearic Islands such as Port de Sóller and Portocolom with 76 cm and 74 cm respectively. In Tab. 4.1, the maximum oscillation amplitude (defined as trough-to-crest) for every port with an operative tide gauge for this event is given. With the aim of studying in detail this event, we can divide it in

subevents since within the 20 hours that the event lasted different moments with different atmospheric perturbations and sea level responses are found. In Fig. 4.2, we can find the filtered time series (filter details can be found in Sect. 3.2.1) of the sea level and atmospheric pressure measured in Ciutadella. We also have plotted the wavelet power spectrum for each of the time series. In these plots, the selected subevents have been separated by vertical lines: **23S1** (1130-1350 UTC of May 23), **23S2** (1350-1450 UTC of May 23), **23S3** (1450-1640 UTC of May 23), **23S4** (1640-1830 UTC of May 23) and **23S5** (1830 May 23-0030 May 24). The choice of these particular subevents is quite arbitrary, it has been done by visual inspection of the sea level and pressure time series to facilitate the description of the whole event. When studying the event for Mallorca Island we will consider the subevents to be the same, but the division times will be delayed because the atmospheric perturbation is travelling from the southwest, which implies that it will cross Mallorca approximately half an hour before arriving to Ciutadella.

Tide gauges	Code	Island	Owner	WH (cm)	Time UTC	Period (min)
Sant Antoni	SAN	Eivissa	SOCIB	58.8	05/23 11:40	19.7
Sa Ràpita	RAP	Mallorca	SOCIB	42.7	05/23 20:02	52.5
Portopetro	PPT	Mallorca	VENOM	31.2	05/23 18:26	10.4
Portocolom	PCO	Mallorca	VENOM	74.3	05/23 19:18	20.8
S'Arenal	ARL	Mallorca	VENOM	47.8	05/23 14:54	78.6
Porto Cristo	PCR	Mallorca	SOCIB	43.0	05/23 17:08	41.7
Andratx	AND	Mallorca	SOCIB	40.4	05/23 16:41	13.9
Palma	PLM	Mallorca	VENOM	40.9	05/23 18:59	62.4
Cala Bona	CBN	Mallorca	VENOM	36.2	05/23 18:13	41.7
Cala Rajada	CRJ	Mallorca	VENOM	36.9	05/23 17:47	7.0
Can Picafort	CPF	Mallorca	VENOM	59.5	05/23 15:32	83.3
Port de Sóller	PSO	Mallorca	VENOM	76.2	05/23 16:16	11.0
Cala'n Bosch	CBC	Menorca	VENOM	26.1	05/23 14:34	16.5
Cala Galdana	CGL	Menorca	VENOM	44.7	05/23 14:18	7.0
Son Blanc	SBL	Menorca	IGN	44.8	05/23 14:19	15.6
Ciutadella	CIU	Menorca	Ports IB	109.3	05/23 14:20	11.7
Port d'Addaia	PAD	Menorca	VENOM	27.8	05/23 14:43	20.8
Fornells	FRN	Menorca	VENOM	22.7	05/23 17:41	44.1

Table 4.1: All tide gauges (south to north) with recorded sea level during the 23 May 2021 meteotsunami are listed, the columns are: its identification code, the island where they are located, the running institution, the maximum wave height (WH), the time of the maximum wave height and the most energetic period during the maximum wave height.

A. Event in Ciutadella

Focusing our attention on Ciutadella's time series for sea level and atmospheric pressure (Fig. 4.2) we can clearly identify the differences between the defined subevents:

23S1 The first local maximum in the sea level oscillations (Fig. 4.2b) is found at approximately 1130 UTC with a wave height of more than 70 cm. This first subevent is
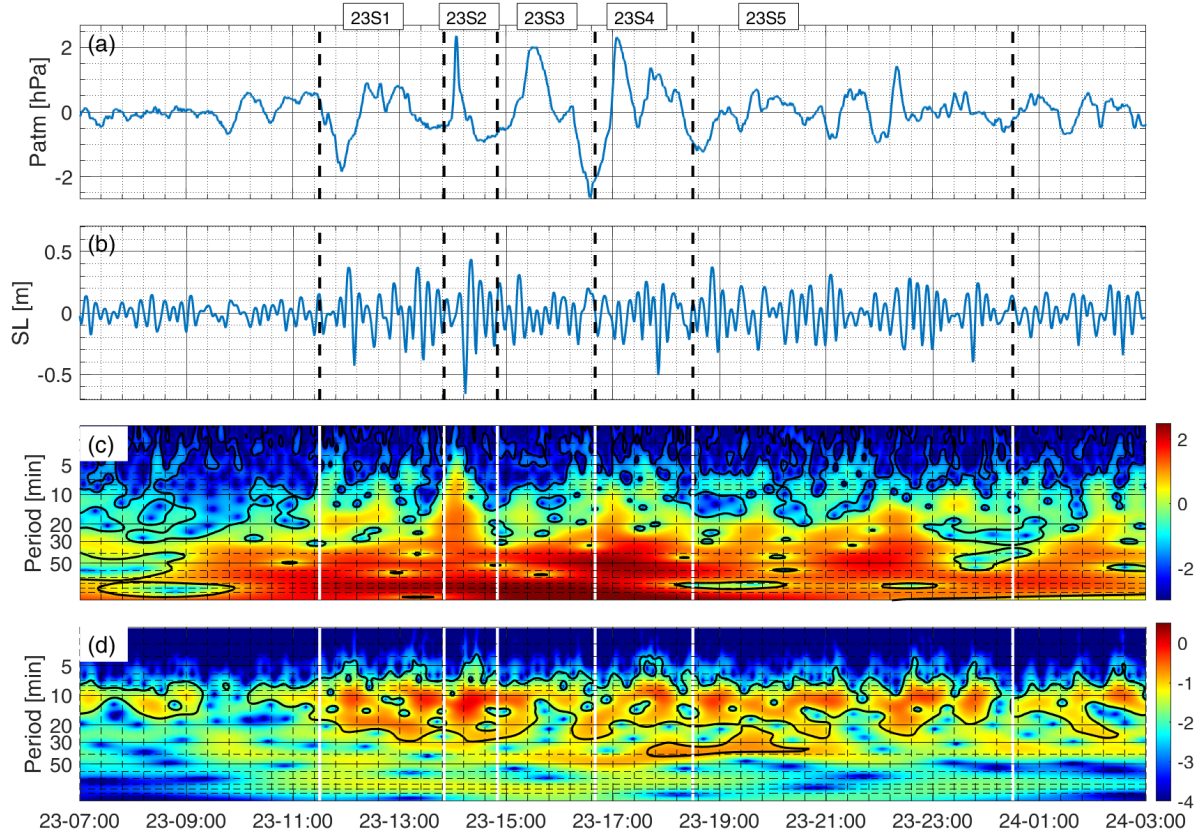
Figure 4.2: (a) Filtered atmospheric pressure time series (hPa) measured at Ciutadella between 0700 UTC 23 May 2021 and 0300 UTC 24 May 2021, this time is shared by all subplots. (b) Filtered sea level time series (m) measured by the tide gauge within Ciutadella Harbour. (c) Wavelet power spectrum of the measured atmospheric pressure (colour scale in $\log_{10}([\text{hPa}^2])$). (d) Wavelet power spectrum of the measured sea level (colour scale in $\log_{10}([\text{m}^2])$). The vertical lines, dashed black lines in the time series, (a) and (b), and white lines in the power wavelet spectra, (c) and (d), separate the chosen subevents. The black contour in the wavelet power spectra denotes the 95% significance level.

simultaneous with the pass of a rapid atmospheric pressure depression of 2 hPa (Fig. 4.2a); the minimum in atmospheric pressure corresponds with the local maximum in sea level oscillation at 1130 UTC. It is followed by small oscillations, of around 1 hPa of amplitude, that also produces a meteotsunami of more than 70 cm at 1330 UTC. In Fig. 4.2c we can see how for this subevent the atmospheric perturbation has a spectral peak around the 20 min period, which coincides with twice the normal period of Ciutadella Harbour.

23S2 The largest sea level oscillation for this meteotsunami event is found in the second subevent, at 1420 UTC, when a very quick pressure jump passes over Ciutadella. In the wavelet spectrum of the atmospheric perturbation (Fig. 4.2c), it can be seen how the energy content of this pressure peak goes from periods of 1 hour to 5 min, matching the 10.5 min natural period of Ciutadella Harbour.

23S3 In this third event, we find a 2 hPa atmospheric pressure jump, that raises for 40 min, and then a fall of another 2 hPa. The sea level response is less intense than in the previous subevents, a maximum oscillation of less than 50 cm at 1530 UTC

is observed. The cause of this weaker oscillation can be found in the wavelet power spectrum of the atmospheric perturbation, since during this subevent the spectral energy in periods below 30 min is very low, except at the moment of maximum amplitude of the sea wave (around 1530 UTC).

23S4 After the decrease in atmospheric pressure at the end of the previous subevent, there is a fast 4 hPa increase, that lasts 30 min, followed by another oscillation of 1.5 hPa with spectral energy at 1 hour period. We see how, although the initial atmospheric pressure jump has energy close to the 10 min, the sea level response is very weak at this moment. Later, after the atmospheric wave oscillation, the sea level oscillation reaches an amplitude of 60 cm.

23S5 In this last subevent, the amplitude of the atmospheric pressure perturbation is smaller than in the previous ones, without any jump larger than 2 hPa. However, its wavelet power spectrum shows an important amount of energy near the 20 min period, which is comparable to the energy at these frequencies found in 23S1 and 23S4. This causes sea level oscillation of more than 50 cm. It is particularly interesting to compare the sea level response to atmospheric pressure jump of around 2 hPa produced at 2230 UTC with the response to the later atmospheric wave (2300-0000 UTC), which has 3 oscillations of less than 1 hPa but with period closer to 10 min. The amplitude of the atmospheric perturbation in the second part is half the amplitude of the first one, but the sea level response is larger in the second part ($\sim$ 2350 UTC).

All in all, during the whole event different atmospheric perturbations pass over Ciutadella generating different sea level responses depending on the perturbation characteristics. The maximum oscillation has an amplitude of 109 cm and it is produced during 23S2. Several large oscillations of more than 60 cm are measured in the other subevents in response to different atmospheric pressure perturbations. The spectral energy of the atmospheric disturbance has an important variability in time, which conditions the sea level response. Otherwise, the spectral response of Ciutadella Harbour is almost constant, since most part of its spectral energy is concentrated on its normal period of 10.5 min.

B. Event in Mallorca

As it can be seen in Tab. 4.1, this atmospheric perturbation also caused important sea level oscillations in other ports of the Balearic Islands. For this particular event the VENOM network offers sea level observations for 12 different locations that, added to the tide gauges installed by other institutions, lead to a total of 18 active tide gauges. Thus, we can characterize the spatial impact of this event.

In Fig. 4.3, we have plotted some sea level time series of the tide gauges that have measured the largest oscillations in Mallorca. The wavelet power spectra have been plotted in Fig. 4.4 for the same locations as in Fig. 4.3. With a quick look to Fig. 4.3 and 4.4, one can notice large differences between the sea level signal at each tide gauge. First, the response to atmospheric forcing is different as a consequence of the different harbours topographies that lead to the amplification of different eigen modes. From Fig. 4.4 we can identify the natural modes of Andratx (AND), S'Arenal (ARN), Port de Sóller (PSO), Portocolom (PCO) and Can Picafort (CPF) around 14 min, 25 min, 10 min, 21 min and 17 min, respectively. Some energy bands around the eigen modes are thin and sharp as the

21 min for PCO and CIU (10.5 min, see Fig. 4.2d) but most of the other ports have the energy distributed in a broader frequency band with numerous energy peaks. There are some ports that have important energy peaks at larger periods that correspond to modes trapped within a bay or a shelf. This is the case for ARN that have a thick peak between 60 and 80 min period shared with the Palma tide gauge (not shown), both located in the Palma Bay. CPF also has a peak around 74 min which is the natural oscillation period of the Alcúdia Bay (not shown) and AND also presents important energy content at 34 min that could correspond to an edge wave mode as suggested in Liu et al. (2002). Finally, in the port of Cala Ratjada (CRJ) the wavelet power spectrum does not show any clear natural response, the small dimensions of the port and the fact that it is not located in any major harbour or bay reduces the amplification by harbour resonance. Therefore, the sea level measured in CRJ, and in other locations with similar characteristics as Cala Bona (CBN), Cala'n Bosch (CBC) or Son Blanc (SBL), is more similar to the sea level at the outer shelf.

By looking at Fig. 4.3, one can observe the high spatial variability of sea level oscillation amplitudes and of the timings. During 23S3 the maximum of spectral energy is found close to the 1 hour period (Fig. 4.5), this period is close to the normal modes of Palma and Alcúdia bays which results in maximum sea level oscillations in ARL (Palma Bay) and in CPF (Alcúdia Bay) during this subevent. PSO is, after CIU, the second port with the largest oscillations. In 23S1 the amplitude of the sea level oscillation in PSO reaches 40 cm simultaneously to a 2 hPa pressure jump (Fig. 4.5). Later, the pressure spike of 23S2 does not seem to have any important response in PSO sea level which is surprising since this subevent produces the maximum sea level oscillation in Ciutadella and both ports have their normal oscillation mode at a similar period, close to 10 min. The maxima, with more than 70 cm of sea level change, are produced as consequence the rapid 2 hPa jumps of 23S3 and 23S4. During this whole period, the oscillations are maintained with an amplitude larger than 40 cm.

The other port with major sea level oscillations, over 70 cm, is Portocolom (PCO). In the wavelet spectrum (Fig. 4.4) it is clear that all the spectral energy for the oscillations within this port is gathered around its 21 min normal period. The difference with the other ports is that the oscillation are maintained for several cycles (5-10) and the maxima are given after a long time interval of energy accumulation inside the harbour. We can see how during 23S1, when the atmospheric perturbation has energy at low periods but for a short time interval, no major oscillations are observed in this harbour. However, the largest oscillations are given in 23S3 and 23S4 where the atmosphere has an important amount of energy between 20 and 40 min during more than 3 hours, leading to a maximum oscillation of 74 cm at 1918 UTC. It is worth noticing that this long time of large oscillations is interrupted around 1650 UTC without any appreciable cause in the atmospheric counterpart.

Finally, AND and CRJ present smaller oscillation (40 cm) than the other port, and it is hard to identify the direct relation between the sea level response and the simultaneous atmospheric perturbation structure.

To summarize, we have observed very different sea level signals at the different ports due to the high importance of the topographical response of each one of them. PSO and PCO registered severe oscillations of more than 70 cm, and the oscillations also surpassed the 50 cm in ARN and CPF. The idea of observing an outer sea level perturbation propagating along the coast of Mallorca from these measurements have been discarded. To do it, some data treatment should be used to eliminate the effect of the harbours'
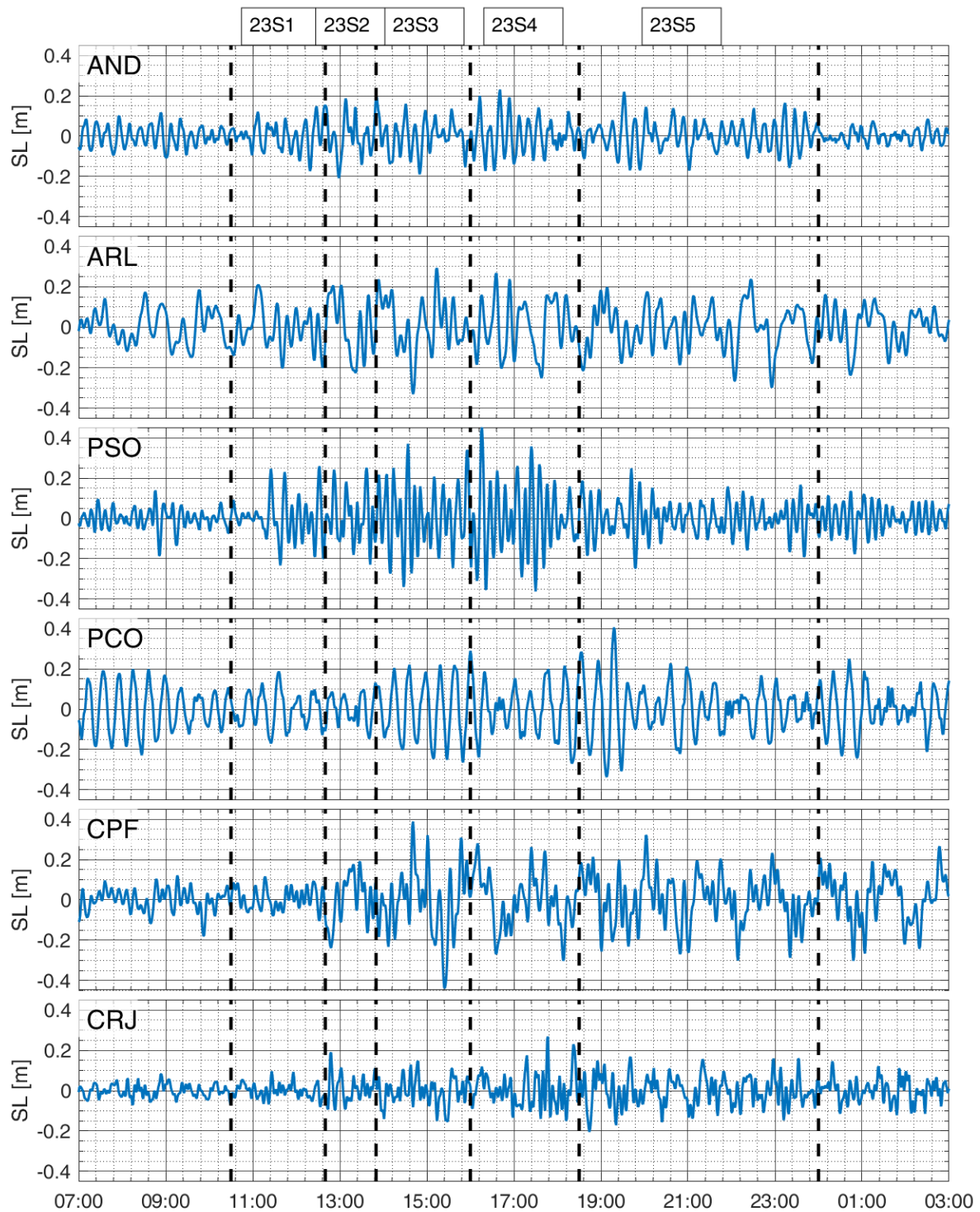
Figure 4.3: Filtered sea level time series (m) measured at different tide gauges of Mallorca between 0700 UTC 23 May 2021 and 0300 UTC 24 May 2021. The tide gauges are sorted from south (top) to north (bottom): Andratx (AND), S'Arenal (ARL), Port de Sóller (PSO), Portocolom (PCO), Can Picafort (CPF) and Cala Ratjada (CRJ). The black dashed vertical lines separate the chosen subevents.
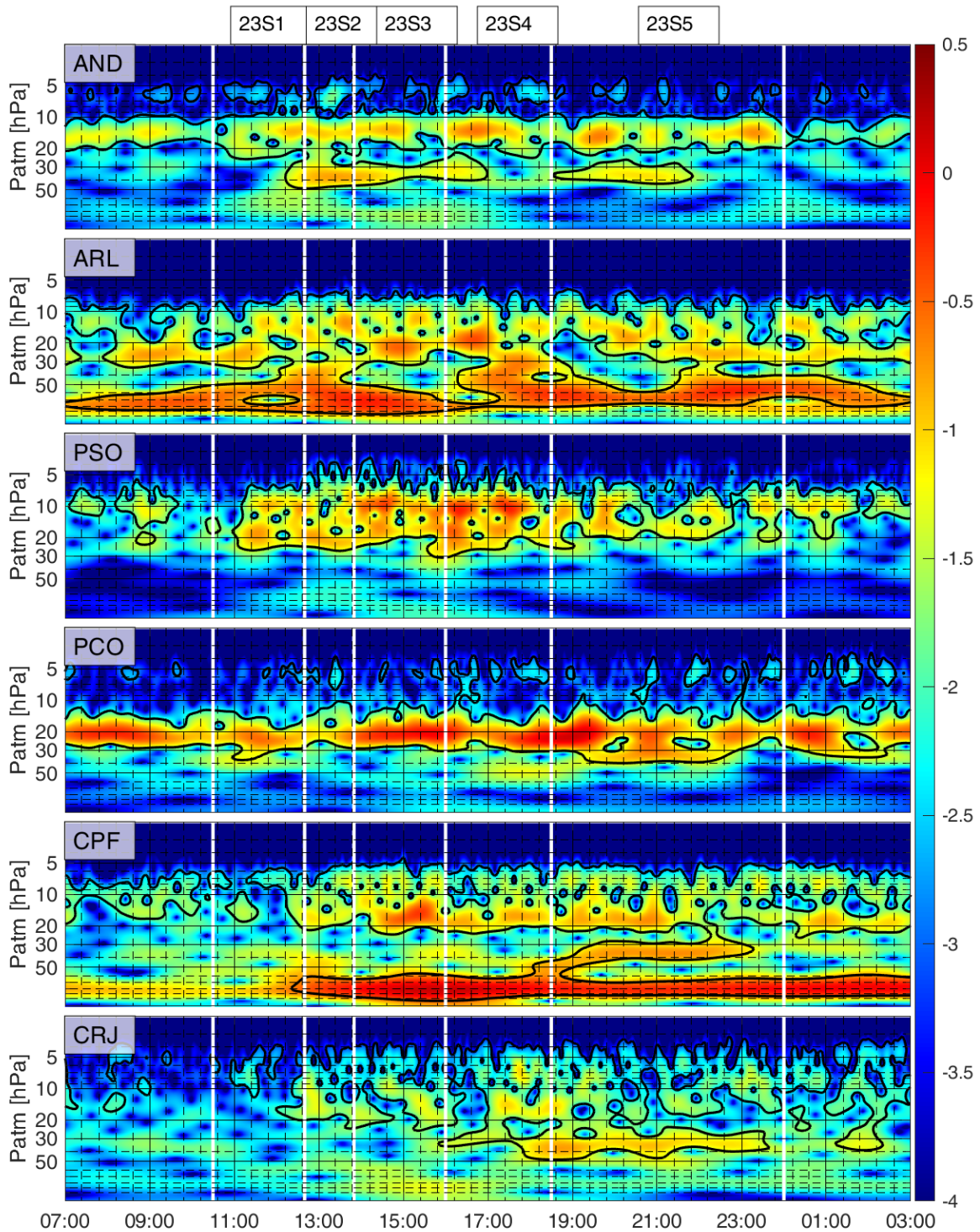
natural response.

Figure 4.4: Wavelet power spectrum of the measured sea level at different tide gauges of Mallorca between 0700 UTC 23 May 2021 and 0300 UTC 24 May 2021 (colour scale in $\log_{10}([m^2])$). The tide gauges are sorted from south (top) to north (bottom): Andratx (AND), S'Arenal (ARL), Port de Sóller (PSO), Portocolom (PCO), Can Picafort (CPF) and Cala Ratjada (CRJ). The white vertical lines separate the chosen subevents. The black contour in the wavelet power spectra denotes the 95% significance level.
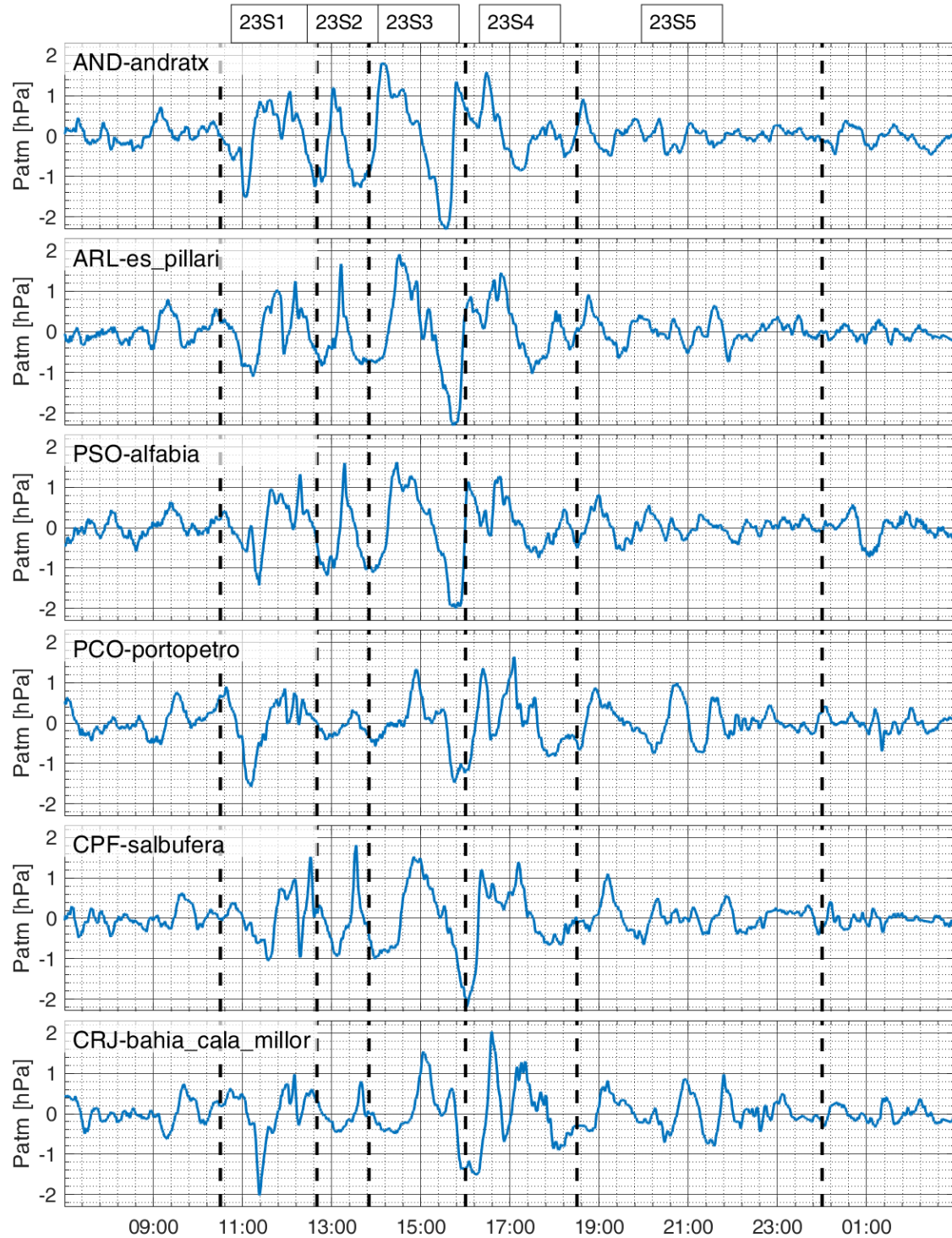
Figure 4.5: Filtered atmospheric pressure time series (hPa) measured at the closer barograph to each of the tide gauges of Fig. 4.3, between 0700 UTC 23 May 2021 and 0300 UTC 24 May 2021. The barograph stations are sorted from south (top) to north (bottom): Andratx (AND), Es Pil·larí (ARL), Alfàbia (PSO), Portopetro (PCO), S'Albufera (CPF) and Badia de Cala Millor (CRJ). The black dashed vertical lines separate the chosen subevents.

C. Spatial variability of the atmospheric perturbation

One of the factors that may affect the difference in the spatial impact of meteotsunami events is the spatial variability of the atmospheric mesoscale perturbations. In Fig. 4.5 we
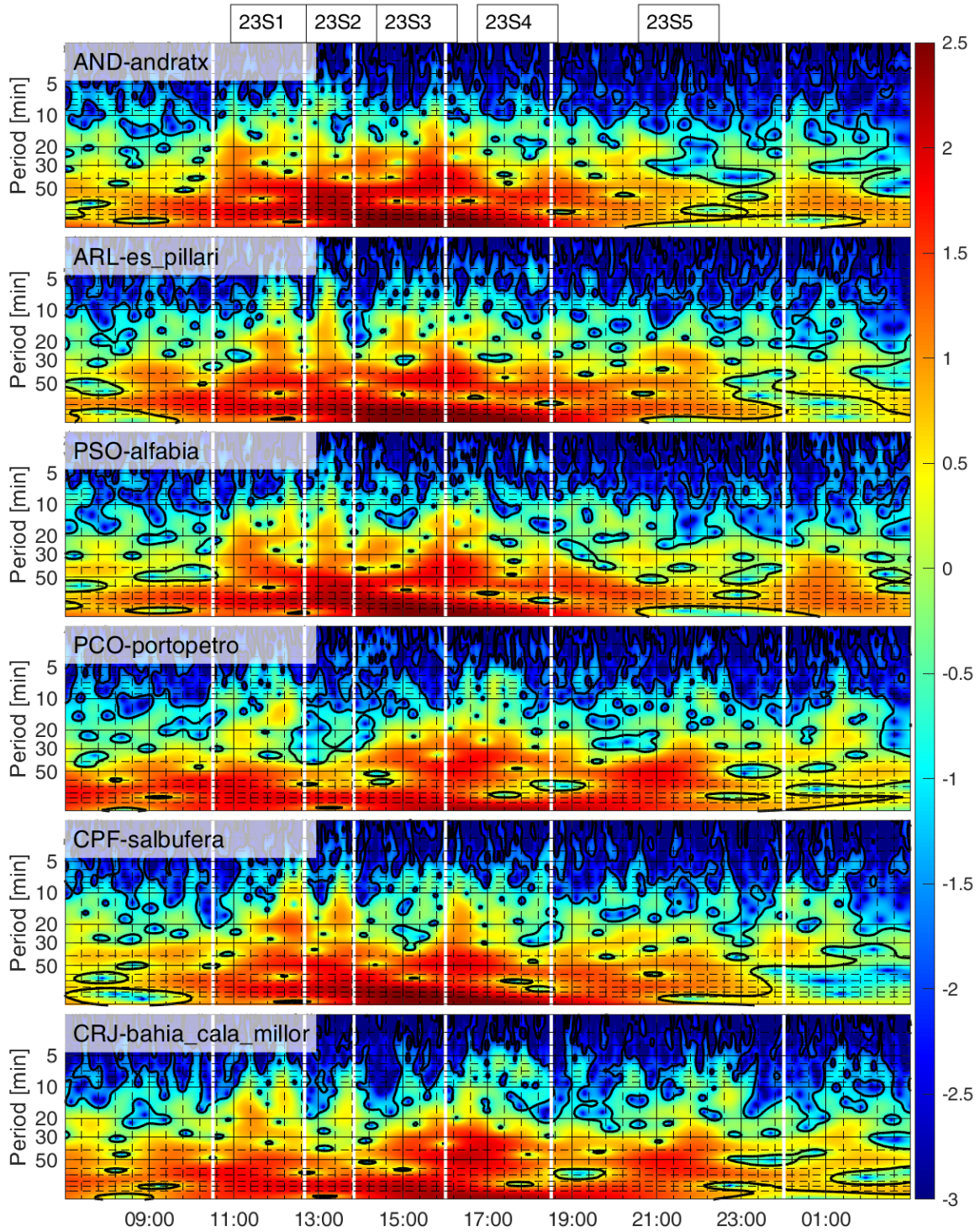
46

Figure 4.6: Wavelet power spectrum of the measured atmospheric pressure at the closer barograph to each of the tide gauges of Fig. 4.3, between 0700 UTC 23 May 2021 and 0300 UTC 24 May 2021 (colour scale in $\log_{10}([\text{hPa}^2])$). The barograph stations are sorted from south (top) to north (bottom): Andratx (AND), Es Pil·larí (ARL), Alfàbia (PSO), Portopetro (PCO), S'Albufera (CPF) and Badia de Cala Millor (CRJ). The white vertical lines separate the chosen subevents. The black contour in the wavelet power spectra denotes the 95% significance level.

have plotted the filtered time series of atmospheric pressure measured in the BalerasMeteo

stations closer to each of the tide gauges shown in Fig. 4.3, and their correspondent wavelet power spectrum are plotted in Fig. 4.6. From these figures, we can analyse the spatial variability of the atmospheric perturbation that causes the meteotsunamis; the same subevents defined for the Ciutadella's time series are used here:

23S1 In the first subevent a first trough of 1-2hPa is found followed by a quick oscillation (Fig. 4.5). At the east coast (Portopetro and Cala Millor) the first depression is deeper than at the north (Andratx and Alfàbia) or centre (Es Pil·larí and S'Albufera) of the Mallorca. The energy at low periods increases at the north-east of the island being Alfàbia and s'Albufera the stations with larger energy at periods between 10 and 20 min.

23S2 The second subevent is characterized by a spike in atmospheric pressure of more than 2 hPa that caused the major meteotsunami in Ciutadella. In the atmospheric pressure records, we can see that this peak is not observed in all stations: the eastern stations (Portopetro and Cala Millor) do not register any important peak for this subevent. We also can see that from Andratx to Ciutadella (Fig. 4.2) the peak have become thinner, increasing its energy at higher frequencies as it moves towards the north-east, i.e., towards Ciutadella.

23S3 This subevent consists of a first quick jump and a subsequent fall in atmospheric pressure. Again, we can observe important differences between the eastern coast stations (PCO and CRJ) and the other ones. At the east, the first jump is smaller (1.5 hPa) than at the north and the centre (2.5 hPa). The subsequent pressure fall is continuous with some small oscillations in the north and centre and interrupted by a step at the east.

23S4 Although here we find a first rapid jump of 3 hPa which is common in all the stations, later, there are differences in the oscillation that comes just after the jump. The amplitude of these oscillations will be larger at the east, surpassing 1 hPa of amplitude and with a period around 30 min.

23S5 The last subevent starts with a small peak of 1 hPa common in all the stations, followed by small oscillations. At the east (PCO and CRJ), two 1.5 hPa oscillation appear between 2030 and 2100 UTC with 30-40 min period. Similar oscillations with smaller magnitude can be seen in Es Pil·larí and S'Albufera. However, these oscillations are not noticeable at the northern stations (AND and PSO).

Although all stations are detecting high frequency (5 - 120 min) atmospheric perturbations, the shapes and the spectral energy change in space with could cause differences in the sea level response from one location to the other.

After this qualitative description of the differences for the atmospheric perturbation at different locations over Mallorca, we can try to quantify the spatial variability of the atmospheric perturbations. To do that, we compute the correlation between measured time series of atmospheric pressure. Fig. 4.7 shows the maximum correlation coefficients between the time series of measured atmospheric pressure as function of the distance between stations in different frequency bands. The correlation function between the time series has been computed and for every pair of stations. Then, the correlation coefficient plotted is that of the lag with higher correlation to take into account the movement of the atmospheric perturbation over the Balearic Islands. For the highest frequency band 5 -

25 min the measurements are decorrelated at a very short distance, only at distance lower than 25 km we can find correlation coefficient over 0.8. When decreasing the frequency of the perturbation, the correlation between time series increases to large distances: for periods between 20 and 40 min high correlations over 0.8 are found between stations 50 km apart and there are no stations with correlations coefficients lower than 0.6 at distances shorter than 25 km. At the bands of 35 - 55 min and 50 - 70 min the correlation is very high ($\rho > 0.8$) for close stations, separated by less than 30 km, and the correlation is higher than 0.5 for distances smaller than 50 km. These results show how the spatial variability is larger for high-frequency perturbations, although, even for long periods (larger than 50 min), the correlation decreases below 0.5 at distances larger than 100 km.
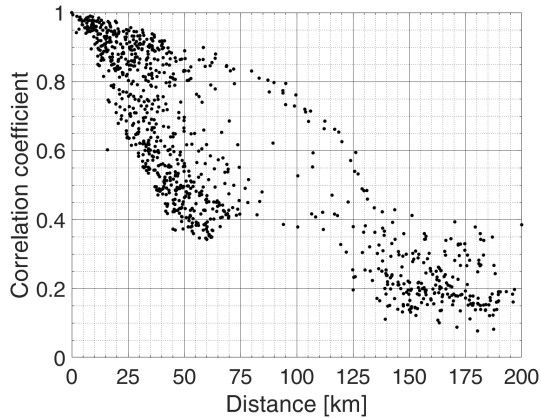
(a) 5 to 25 min periods
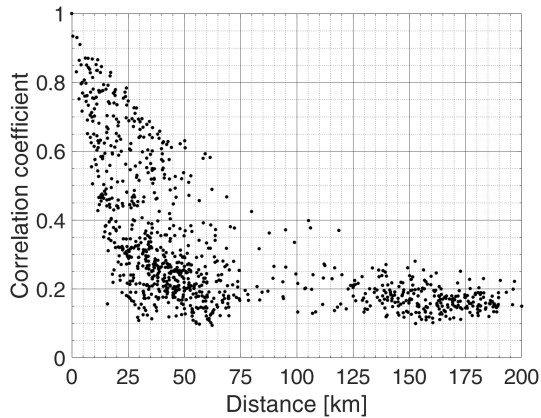
(b) 20 to 40 min periods
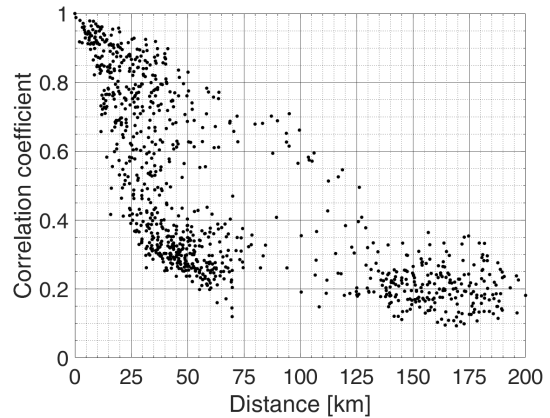
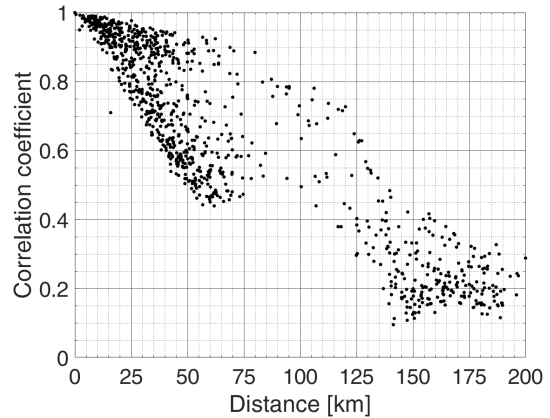(c) 35 to 55 min periods

(d) 50 to 70 min periods

Figure 4.7: Maximum correlation coefficient between filtered atmospheric pressure time series in two different stations. The correlation at the lag of maximum correlation have been plotted for each pair of stations as a function of the distance (km) between stations. In each subplot the correlations have been computed, filtering the time series for a different frequency band: (a) 5 min $< T < 25$ min; (b) 20 min $< T < 40$ min; (c) 35 min $< T < 55$ min; and (d) 50 min $< T < 70$ min.

In Fig. 4.7b, 4.7c and 4.7d it can be noticed that most points of correlation as function of distance follow an exponential law with the correlation quickly falling with distances larger than 30 km. However, some stations maintain high correlations at distances larger than 50 km. This can be explained by the existences of large zones at the east and centre of Mallorca, with no major topographical accidents that allow the propagation of the

perturbation large distances. This separation in zones can also be observed from Fig. 4.5 where the stations from the north (AND and PSO) from the centre (ARL and CPF) and from the east (PCO and CRJ) have more similarities between them than with those from other regions.

D. Atmospheric perturbation propagation

As introduced in Chap. 2 the atmospheric perturbation speed and propagation direction are key parameters that condition the meteotsunami amplitude. The algorithm to compute the atmospheric perturbation velocity introduced in Chap. 3 has been applied for this case study. We have computed the perturbation speed and direction every 10 minutes by applying the algorithm to a moving 2 hours window over the filtered time series of atmospheric pressure. The results are shown in Fig. 4.8. We can observe how during the whole event the speed of the perturbation has values between 30 and 35 m/s which would amplify by Proudman resonance when propagating over open sea with depth between 90 and 125 meters. The obtained direction of propagation oscillates from 210° to 270°. Both the speed and direction of propagation are in agreement with those obtained in previous case studies (Jansa et al., 2007) and in numerical studies (Vilibić et al., 2008; Ličer et al., 2017) for meteotsunami generation in Ciutadella. However, significant variations in speed ($\sim$7 m/s) and in direction ($\sim$80°) occur within the same event. Furthermore, the percentile lines (blue) show the wide distribution of the velocity estimates for different stations, which also changes with time. Although part of this variability could be a result from the error in the velocity estimation by our algorithm, we also capture the *natural* variability of the atmospheric perturbation with time and space that could condition the resulting meteotsunami amplitude. Up to our knowledge, there are not published studies analysing how the heterogeneities in the atmospheric perturbation can affect the Proudman resonance at the open sea.

Comparing the velocity estimations of Fig. 4.8 with the sea level response we can see how the subevents 23S1, 23S2, 23S3 and 23S4, that have the largest sea level oscillations, correspond with the periods of high coherence, i.e. small spreading, of the speed and direction estimates. At the beginning and end of the event, when the atmospheric perturbation is weaker, we can observe how the dispersion between the estimations made on different stations is larger.

Finally, in Fig. 4.8, we also have plotted the wind speed and direction at 500 hPa for the grid point closer to Palma (green markers). This is a way to validate our method of velocity estimation since, according to the wave duct and wave-CISK theories (Sect. 2.1.2), the existence of a critical level at the upper level is key to favour the perturbation propagation. At the critical level the perturbation velocities matches the wind velocity, in other word the perturbation velocity should be the same that the wind velocity at the critical level. Thus, finding similar values for the wind speed at 500 hPa and for the propagation velocity is physically consistent with the existence of the wave duct and the wave-CISK mechanisms.

E. Synoptic pattern and atmospheric profile

As introduced in Chap. 2 these atmospheric perturbations need from a certain atmospheric environment to form and propagate through large distances. In Fig. 4.9 we have plotted the ERA5 reanalysis for the temperature at 850 hPa (Fig. 4.9a) and the wind
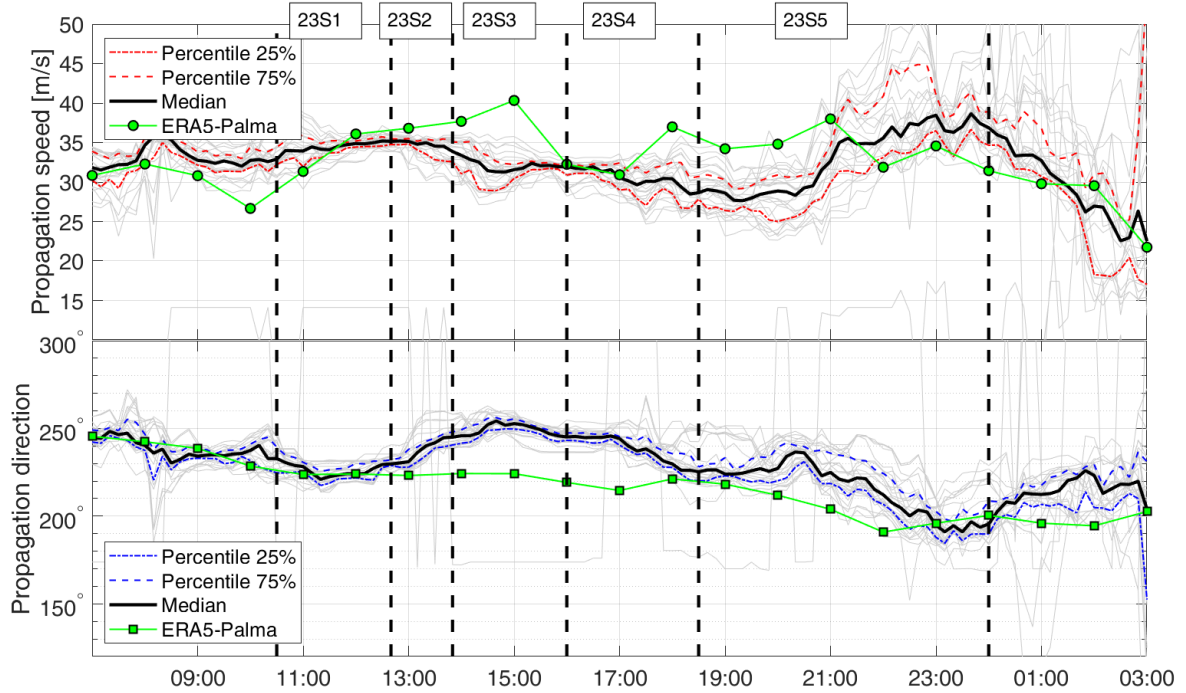
Figure 4.8: Estimated propagation speed (m/s) (top) and direction (degrees from the north) (bottom) between 0700 23 May 2021 and 0300 24 May 2021. The estimation for all stations have been plotted in grey, the median is plotted with the black solid line and the dashed (red for the speed and blue for the direction) lines mark the 25% and 75% percentiles. The green markers represent the speed (top) and direction (bottom) of the wind speed provided by ERA5 reanalysis at 500 hPa at the grid point closest to Palma. The black dashed vertical lines separate the chosen subevents.

at 500 hPa (Fig. 4.9b) fields at 1300 UTC 23 May 2021, which are typically shown in the literature (e.q. Šepic et al. (2015); Zemunik et al. (2021)) to illustrate the synoptic conditions during meteotsunami events. As introduced in Chap. 2, we need an entrance of warm and dry Saharan air at low levels to stabilize the lower troposphere and from a strong jet at higher levels to make the upper layers unstable due to the generated wind shear, which facilitates the existence of a critical level where the atmospheric perturbation velocity matches the wind velocity. According to the Lindzen (1974) wave ducting theory, when this critical level is given in an unstable layer with Richardson number lower than 0.25 the critical level overreflects the energy of the perturbation back to the lower atmospheric layers, allowing its propagation along long distances.

Fig. 4.9 proves the fulfilment of the classical synoptic pattern for meteotsunamis since Fig. 4.9a shows a mass of warm air reaching the Balearic Islands. In the figure, it is observed that the air temperature at the Islands is lower than at the north of Africa, but observing the vertical profile of temperature (not shown), the thermal increase caused by the entrance of the African air is enough to cause a thermal inversion around 850 hPa. In Fig. 4.9b we see that a strong jet, with wind speed of 35-40 m/s and pointing towards the north-east, is located over the Balearic Islands. This also satisfies the known synoptic pattern that lead to meteotsunamis.

Just from looking at these maps, there is some information that we are missing. For instance, we need the jet to be located in an unstable layer in order to generate an optimal wave duct. In Fig. 4.10, we have plotted the 2D atmospheric stability and wind profiles
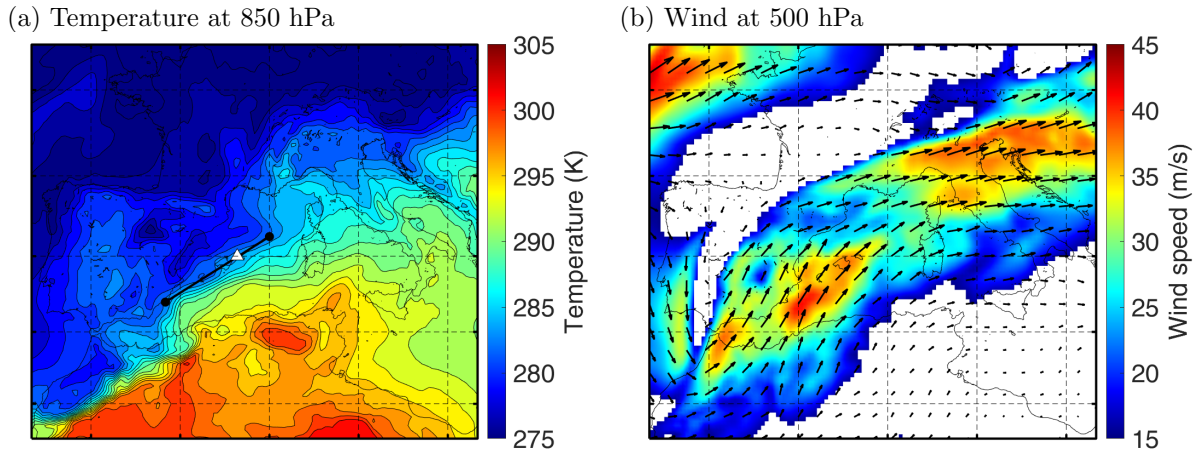
(a) Temperature at 850 hPa

(b) Wind at 500 hPa

Figure 4.9: Synoptic atmospheric conditions at the Western Mediterranean from ERA5 data at 1300 UTC 23 May 2021. (a) temperature (K) at 850 hPa. The black line marks the section shown in Fig. 4.10 and the white triangle the location of Ciutadella. (b) wind at 500 hPa, the wind speed (m/s) is indicated with the plot colour, in the white areas the wind speeds are below 15 m/s.
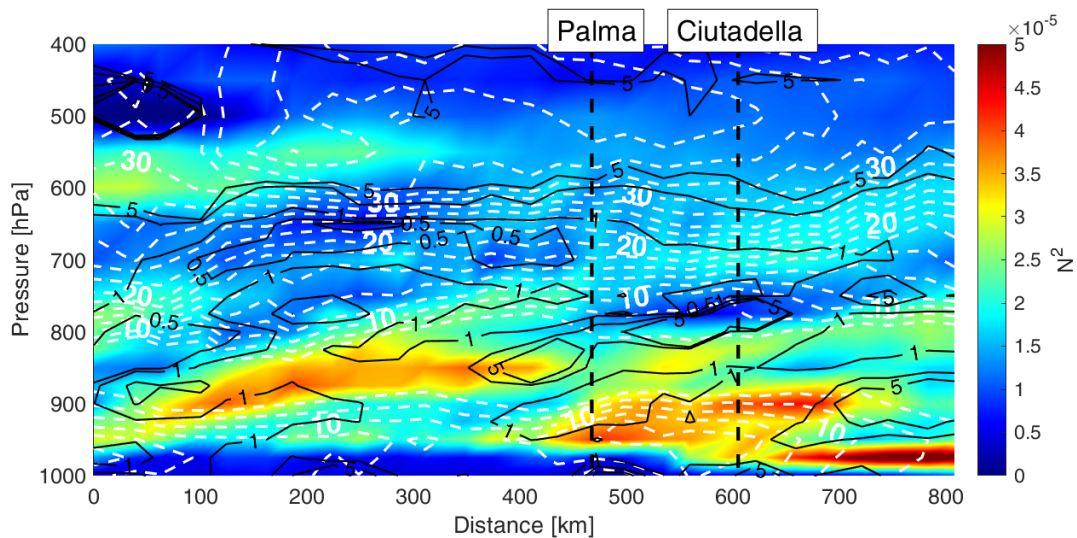

Figure 4.10: Vertical 2D atmospheric profile for the section indicated in Fig. 4.9 at 1300 UTC 23 May 2021. The shown variables are the Brunt-Väisälä frequency (N^2) in s^{-1} (plot colour); the Richardson number (black contours; levels 0.25, 0.5, 1 and 5 are indicated); and the wind speed at the direction 228°, the direction of entrance of the Ciutadella Harbour (white contours, every 2 m/s). The two dashed lines show the location of Palma, Mallorca, and Ciutadella, Menorca, from left to right.

for the section indicated in Fig. 4.9a at 1300 UTC 23 May 2021. From these profiles we can outline the following features:

- There exists a stable layer with higher N^2 than its surrounding layers between the ground and 800 hPa over Mallorca and Menorca. The wind at this layer is weak, close to 10 m/s.

- Between 800 and 500 hPa there is a strong wind shear where the wind changes from 10 m/s to 36 m/s.

52

- The Richardson number does not fall below the 0.25 threshold that leads to unstable turbulent flow. However, in Stull (1988), it is noted that when computing the Ri with discrete data we are averaging the gradient, which may lead to higher values of the Ri. This causes the appearance of instabilities at higher Ri. Hence, layers with Ri lower than 0.5 or 1 are candidates to be, in fact, unstable layers where an overreflecting critical level may exist. In Fig. 4.10 between 100 and 700 km and 800 and 600 hPa we have a layer with a strong wind shear and an estimated Ri below 1: this layer is a good candidate to be a reflecting layer with a critical level that would trap the energy of perturbation travelling at a speed between 20 and 36 m/s close to the surface.

Finally, it is worth noticing that the vertical structure is by far more complex than the analytical models proposed in Chap. 2 to explain the atmospheric perturbations propagation. This complicates the application of analytical models to relate the observed atmospheric structure to the meteotsunami amplitude.

F. Sea wave amplification

One of the advantages of the new VENOM tide gauge network is that the large number of available sea level observations will include measurements from tide gauges located at exposed locations, where the topographical effects will be weaker than in the largest ports or bays. Unfortunately, in this work the observations from Sant Elm, Sa Calobra or Port de Valldemossa, which are exposed tide gauges, are not available. However, we dispose from the observations from Son Blanc tide gauge (SBL), located at the entrance of Ciutadella Harbour (see Fig. 2.2). The topographical effects at this location are very weak in comparison with the harbour amplification produced within Ciutadella Harbour, as it can be seen in the background spectrum plotted in Fig. 3.5. Thus, considering the SBL signal as *proxy* of the external forcing of Ciutadella Harbour, we can differentiate the amplification at open sea, before arriving to SBL, from the amplification by harbour resonance within Ciutadella.

Comparing the sea level measurements between CIU and SBL (Fig. 4.11b and c) it is observed how each peak in wave height in Ciutadella Harbour is preceded by a peak in SBL. For example, the first peak at 1200 UTC of 79 cm in CIU was preceded by a wave of 27 cm at SBL, the one at 1330 of 75 by a 32 cm wave at SBL, and the largest meteotsunami wave, with an amplitude of 109 cm, was forced by a 45 cm wave in SBL. There are some more peaks between 1800 UTC and 0030 UTC with wave height around 70 cm all of them were excited by waves around 30 cm at SBL. Consequently, the amplification induced by harbour resonance in Ciutadella Harbour is of a factor 2-3.

Now we are interested on quantifying the effect of the open sea amplification. First, we should take into account that the wave measured at SBL have suffered from amplification by shoaling since the depth of the Menorca Channel changes from 80-120, at the centre of the channel, to 5-10 meters, at the coast (i.e. in SBL), increasing its amplitude by a factor ~ 2. Some other topographic effects may cause more amplification, but the fact that this tide gauge is located at the outer part of the dike suggests that these effects are weak. To quantify the open sea amplification that have preceded the largest sea wave of 45 cm, first we must subtract the amplification of a factor 2 by shoaling. Then, taking into account that the atmospheric source is a pressure peak of 2.7 hPa that should cause a barotropic sea level response of approximately 2.7 cm, it results in an amplification factor ~ 8. By applying the analytical relationship introduced in Eq. 2.21 that quantifies
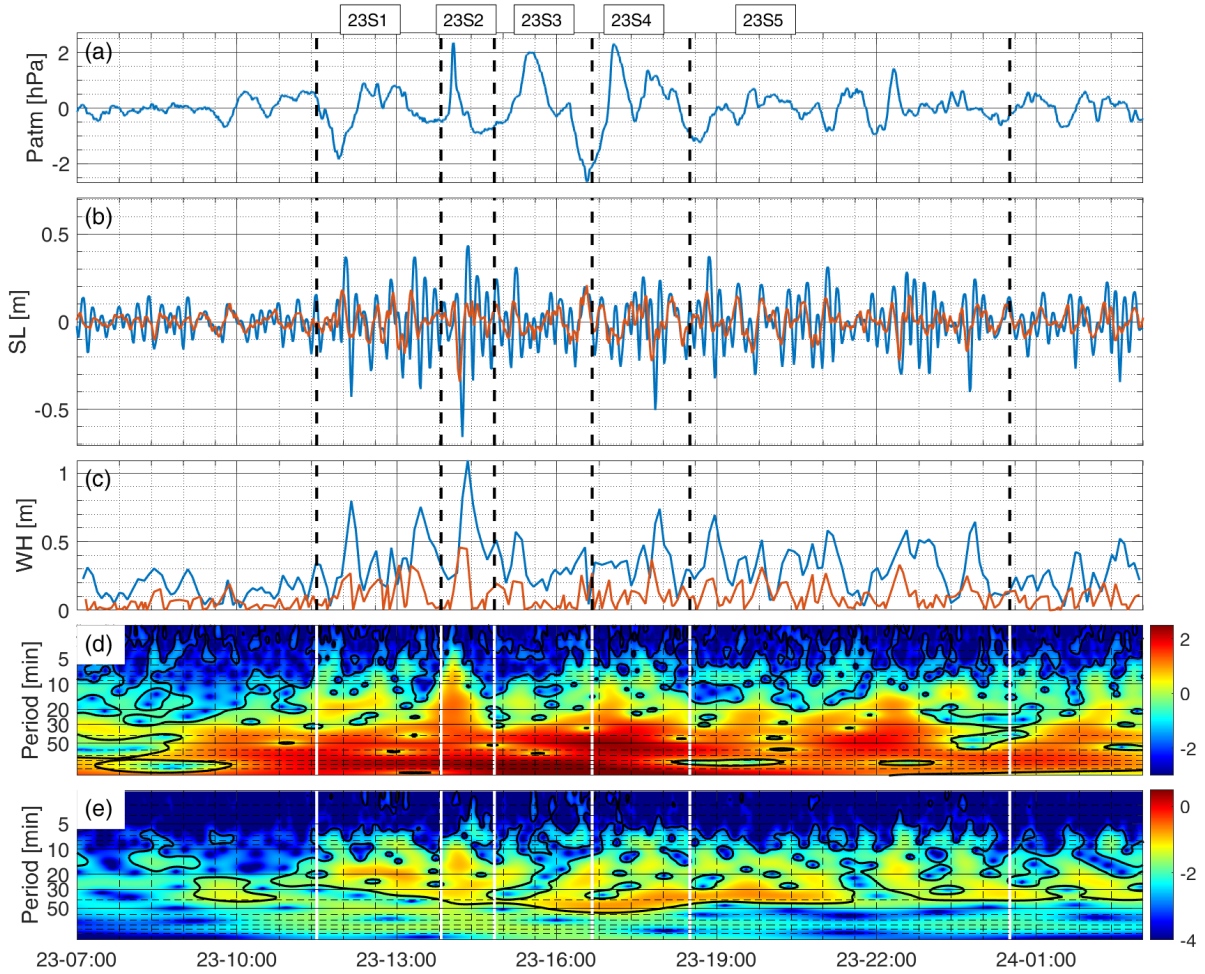
Figure 4.11: Time series measured between 0700 UTC 23 May 2021 and 0300 UTC 24 May 2021. (a) Filtered atmospheric pressure time series measured in Ciutadella and (d) its wavelet power spectrum (colour scale in $\log_{10}([hPa^2])$). (b) the sea level measured CIU (blue) and at SBL (red). (c) the wave height, computed as the difference between maxima and minima in sea level, for CIU (blue) and SBL (red) time series. (e) the wavelet power spectrum for the SBL time series (colour scale in $\log_{10}([m^2])$). The vertical lines, black dashed lines in the time series, (a), (b) and (c), and white lines in the power wavelet spectra, (d) and (e), separate the chosen subevents. The black contour in the wavelet power spectra denotes the 95% significance level.

the amplification produced by Proudman resonance, to this perturbation, that have the following characteristics: the jump lasts 5 min and travels at a speed of ∼35 m/s; we obtain that the perturbation should travel more than 160 km over a shallow sea with optimal conditions for Proudman resonance to amplify the initial wave by a factor 8. This distance is too large for the Balearic basin. The Menorca Channel from Alcúdia Bay to Ciutadella is only 60 km long. Even considering that the perturbation could amplify along the Mallorca shelf, the distance travelled from Cabrera to Ciutadella would be 120 km and from Andratx to Ciutadella the path would be around 140 km long. Similar estimations can be made by estimating the amplification factor at other moments of the event, obtaining amplifications factors 5-10. Hence, some amplification mechanism complementary to Proudman resonance have to contribute to the sea wave measured in SBL.

Another interesting feature to study of the SBL sea wave is its spectral energy distribu-

54

tion in comparison with the spectral energy distribution of the atmospheric perturbation. From Fig. 4.11d and 4.11e, we can infer that the propagating sea wave amplifies majorly the periods between 50 and 5 min, since the energy content of the atmospheric perturbation over 50 min is very important, yet, the sea level measured in SBL have little energy at these periods in comparison with the higher frequencies. In the higher frequencies, we can find similarities between the wavelet power spectrums, for example, at 23S1 most the concentration of energy around 20 min is found for both atmospheric pressure and sea level and the peak of 23S2 with energy between 20 and 10 min can also be found in both wavelet power spectra.

G. Sea wave propagation

One of the goals of the ultra-dense VENOM network is to characterize the sea wave propagation along the Balearic coast. As it has been seen above, the sea level signal measured by the tide gauges in the ports is the response of the port to an external forcing. The topographic response of the port is independent of the external forcing, which mean that the spectral natural response of a particular port or bay can be computed from calm periods (Rabinovich, 1997). Once we have computed the spectral response of the port when no forcing is present, we will call it *background* spectrum, we can estimate the spectral energy of the external forcing by dividing the spectrum computed during the event by the previously computed *background* spectrum for that port. Then, the obtained spectral ratio is, theoretically, an estimation of the spectral energy of the external forcing. Further details on this technique are provided in Chap. 3.

This spectral technique have been applied to time series measured during this meteotsunami event (Fig. 4.12). Theoretically, nearby tide gauges should have a very similar external forcing because the atmospheric forcing maintain their structure at short distances. Fig. 4.12 shows the estimated external forcings for relatively close tide gauges at each subplot. Fig. 4.12a and e contain forcings from quite separated port as are AND, PLM and PSO (a) and CRJ, CPF and SBL (e). These port have different orientations, are located in different bays, and even in different islands. Therefore, it is reasonable that they present that different spectral ratios, though some common energy peaks are found as the 14 min and 7.5 min peaks shared by AND and PSO and the 16 min peak shared by CRJ, CPF and SBL. The other subplots show the spectral ratios of nearby tide gauges where the external forcing should be shared. In panel b the ARL and PLM spectral ratios are plotted showing a large difference in the external forcing for periods below 30 min which is quite surprising since both tide gauges are located within the same bay and the same external forcing is expected. In panel c PCO and PCR have a similar spectral ratio over 14 min, but then a large difference is observed at higher frequencies. Panel d shows the forcings for the last three tide gauges of the eastern coast of Mallorca; PCR, CBN and CRJ from south to north. The line that connects all three tide gauges is just 21 km long, therefore, we expect to find similar forcings for the three ports. Indeed, the plot shows similar forcings for all three instruments with most of the spectral energy concentrated between 5 and 20 min period, although most of the peaks are not located at common frequencies. Finally, in panel f, we plot together the estimated forcing computed from Ciutadella Harbour tide gauge (CIU) and the tide gauges located at the port entrance, in the Son Blanc Port (SBL), only 1.6 km apart. Both spectral ratios have the same peaks at the same frequencies, although the energy is much larger in CIU. For low frequencies the agreement is quite good, but below 15 min the energy in CIU is 1 order of magnitude

larger. This result is not natural, since the obtained spectral ratios should be almost the same.

The large differences between the external forcings estimated by nearby tide gauges cast doubts on the performance of this technique. More research is needed to determine what is going wrong in the application of this technique, since previous studies obtained very similar spectral ratio estimations for nearby tide gauges (Monserrat et al., 1998; Marcos et al., 2009).
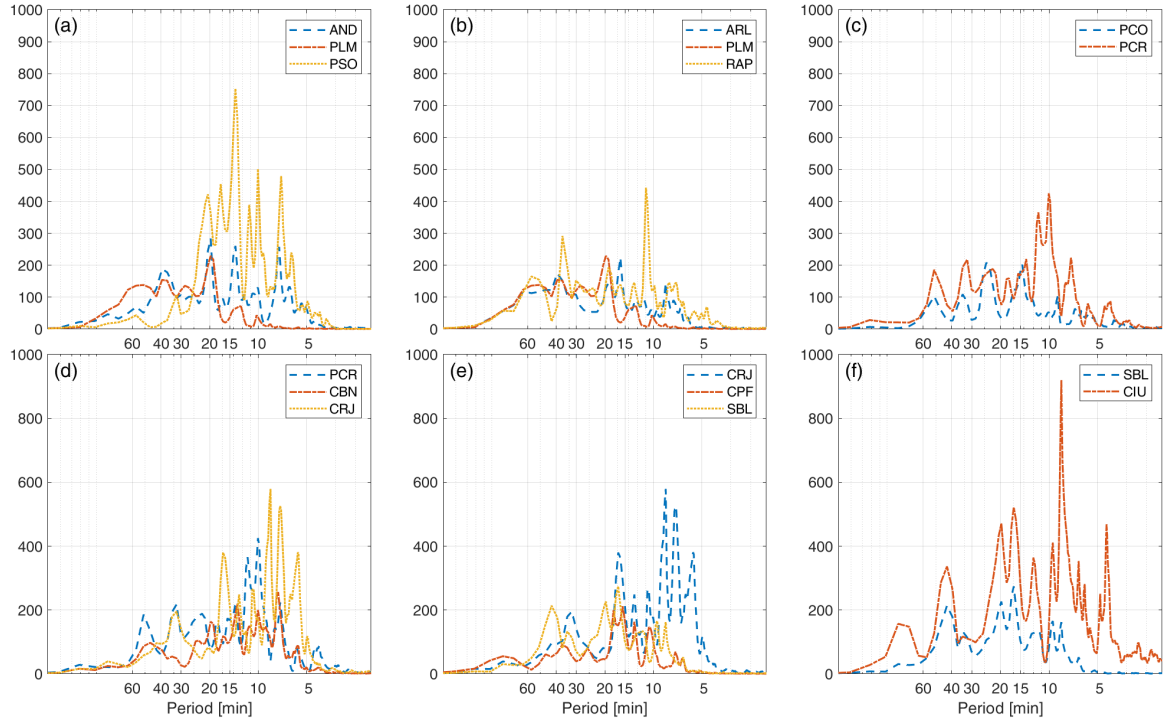

Figure 4.12: Spectral ratios computed during the 23 May 2021 meteotsunami event. The spectral ratios at each subplot are from: (a) AND (blue), PLM (red) and PSO (yellow); (b) ARL (blue), PLM (red) and RAP (yellow); (c) PCO (blue), PCR (red); (d) PCR (blue), CBN (red) and CRJ (yellow); (e) CRJ (blue), CPF (red) and SBL (yellow); and (f) SBL (blue), CIU (red).

One of the weaknesses of this kind of analysis is that they do not take into account the temporal variability of the sea level and atmospheric pressure signals and they take the whole event as more or less stationary. From the analysis of the atmospheric pressure time series, we know that this is an important simplification, since the temporal variations of the atmospheric perturbation generate different sea level responses. Hence, a way to compute the sea level forcings out of the ports taking into account their temporal variability is to apply the same technique used for traditional spectra to the wavelet power spectra instead. The idea is the same, first, we compute a background wavelet power spectrum by averaging in time several wavelet power spectra computed in calm periods (the same criterion to select the calm intervals has been used than for the traditional spectra), then, we compute the wavelet power spectrum for the sea level time series (e.g. Fig. 4.4), and, finally, we divide by the *background* at each time. The result of applying this technique is shown for 6 different tide gauges in Fig. 4.13.

The wavelet spectral ratios, as happens with the averaged spectra computed in Fig. 4.12, should be very similar for nearby tide gauges that are affected by the same atmospheric disturbance. In Fig. 4.13 the estimated wavelet spectral ratios have been plotted
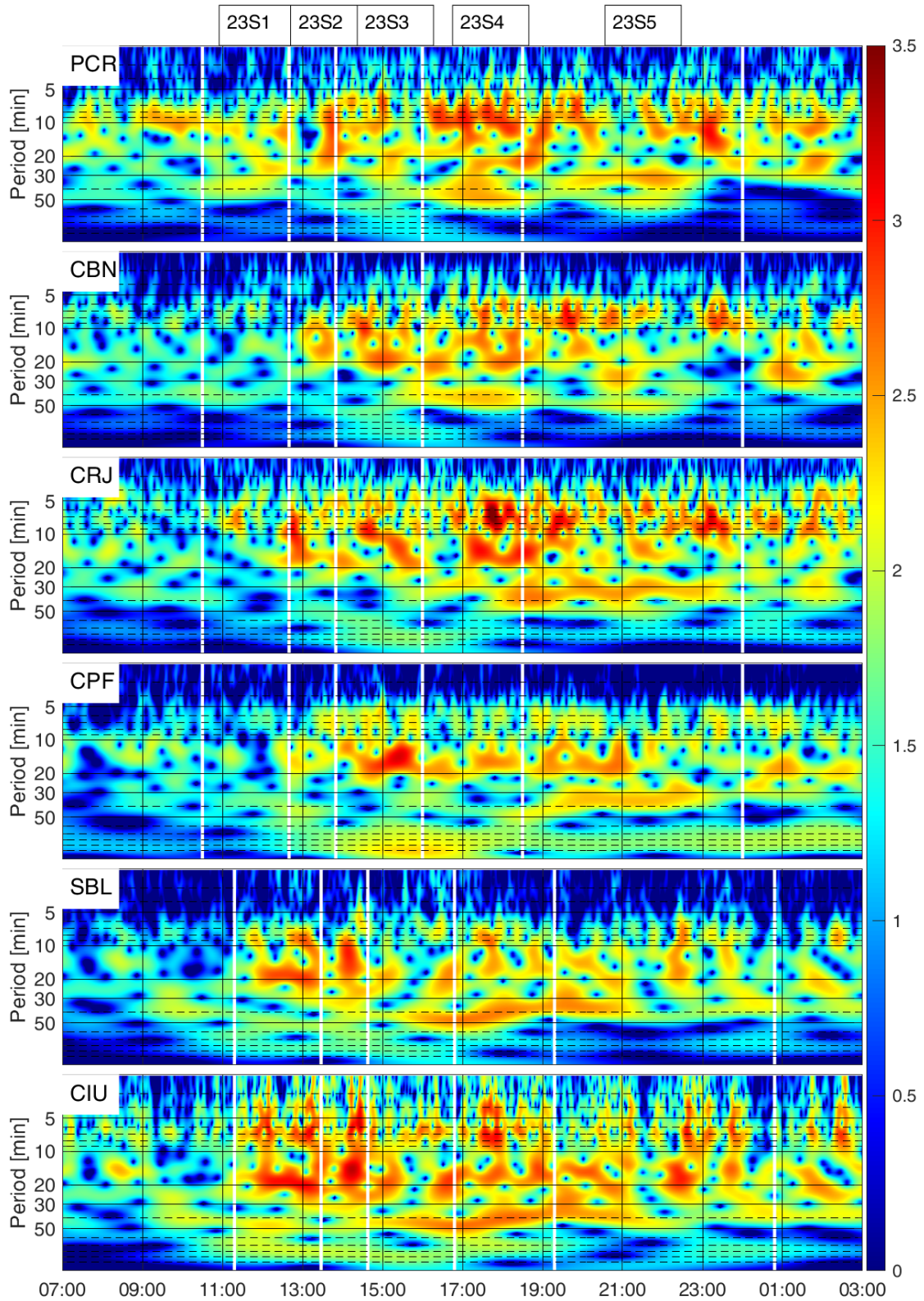
Figure 4.13: Wavelet spectral ratios for the sea level measurements at different ports computed between 0700 UTC 23 May 2021 and 0300 UTC 24 May 2021. The tide gauges are located at, from south (top) to north (bottom): Porto Cristo (PCR), Cala Bona (CBN), Cala Ratjada (CRJ), Colònia de Sant Pere (CSP), Son Blanc (SBL), and Ciutadella (CIU). The wavelet spectral ratio is computed by dividing, in every time step, the wavelet power spectrum measured during the meteotsunami event by the wavelet spectral background of each port (plot colour in logarithmic scale). The white vertical lines separate the chosen subevents.

for tide gauges located at the north-east of Mallorca (PCR, CBN, CRJ and CPF) and at the west of Menorca (SBL and CIU). The first three stations located at the north of the east coast of Mallorca show similar patterns in the wavelet spectral ratios but with noticeable differences. During 23S1 any port presents noticeable forcings, in 23S2 they have a similar structure between 10 and 20 min. If the same external forcing was propagating with the atmospheric perturbation towards the north-east, the spectral energy peak should appear first in PCR, later in CBN and, finally, in CRJ but the plot shows the spectral peak in CRJ before than in CBN. Later, for subevents 23S3, 23S4 and 23S5 the forcing energy is always located between 10 and 30 min but no common peak can be observed. When comparing CPF with the previous tide gauges, there is not much in common, since CPF is far from the others and it is located in the Alcúdia Bay with a different entrance orientation. However, in subevent 23S5 a line of intense energy around 30 min appears simultaneously in CPF and in CRJ that could be a sign of a shared forcing. Finally, we compare again the estimated forcing in SBL and in CIU. The same results are the same as those found in Fig. 4.12f: they share the same energy peaks, in this case not just at the same frequencies also at the same times, except for the periods below 15 min where the energy inside the Ciutadella Harbour is much larger for some unclear reason.

4.2 More meteotsunami events

In this section we are going to present some result from two other meteotsunami events (10 May 2021 and 18 June 2021) for comparison between the different events in the discussion that will be made in Chap. 5. Only the most relevant details of these events will be provided.

4.2.1 10 May 2021

From 2200 UTC of 9 May to 1900 UTC of 10 May 2021 several oscillations of more than 50 cm were measured by the tide gauge of Ciutadella Harbour, being the maximum oscillation of an amplitude of 65 cm. Compared with the event of 23 May 2021, this one is much weaker and it is not even considered a meteotsunami by the AEMET warning system because its amplitude was smaller than 70 cm. The oscillations are not significantly intense in other ports, being PSO the second port with larger oscillation with 52 cm of amplitude. Nevertheless, the fact that this event is weaker can help us to discern some features that intensify the meteotsunami oscillations in the 23 May and 18 June 2021 by comparing the events. In Tab. 4.2 all maximum oscillations are listed for the tide gauges active during this event.

There are interesting features to be reviewed from this event in the sea level record in CIU and SBL and its simultaneous atmospheric pressure perturbation (Fig. 4.14). As it can be seen in Fig. 4.14, we have also divided this event in arbitrary subevents to describe it. 10S1 (2200 - 0030 UTC) presents the largest sea level oscillations caused by a rapid pressure jump of 2.5 hPa. There are two peaks in wave height: one simultaneous to the pressure jump and the other with the fall. In this subevent, we find the maximum of the atmospheric perturbation energy at high frequency, 5 to 20 min period. In 10S2 (0130 - 0500 UTC) a quick pressure jump is also found with its subsequent fall, both of 1.5 hPa. They cause a similar response as 10S1 but weaker. Although 10S3 (0700 - 1130 UTC), 10S4 (1130 - 1630 UTC)a and 10S5 (1630 - 2000) do not seem to have important

Tide Gauge	Code	Island	Owner	WH (cm)	Time UTC	Period (min)
santantoni_socib	SAN	Eivissa	SOCIB	38.9	05/10 01:51	22.0
sarapita_socib	RAP	Mallorca	SOCIB	29.3	05/10 04:19	52.5
Portopetro	PPT	Mallorca	VENOM	24.9	05/10 02:01	-
Portocolom	PCO	Mallorca	VENOM	45.7	05/10 01:02	22.1
S'Arenal	ARL	Mallorca	VENOM	36.2	05/10 03:05	62.4
portocristo_socib	PCR	Mallorca	SOCIB	44.0	05/10 02:50	11.0
andratx_socib	AND	Mallorca	SOCIB	28.0	05/10 08:56	13.9
Palma	PLM	Mallorca	VENOM	38.6	05/10 02:01	66.1
Cala Bona	CBN	Mallorca	VENOM	21.7	05/10 07:22	39.3
Cala Rajada	CRJ	Mallorca	VENOM	30.5	05/10 02:06	4.9
Can Picafort	CPF	Mallorca	VENOM	33.2	05/10 16:09	74.2
Port de Sóller	PSO	Mallorca	VENOM	52.3	05/10 12:13	9.8
Cala'n Bosch	CBC	Menorca	VENOM	16.0	05/09 23:20	-
Son Blanc	SBL	Menorca	VENOM	31.1	05/09 23:22	-
Ciutadella	CIU	Menorca	IGN	65.1	05/10 15:58	10.4
Port d'Addaia	PAD	Menorca	VENOM	17.6	05/10 00:14	-
Fornells	FRN	Menorca	VENOM	8.9	05/10 00:36	-

Table 4.2: All tide gauges (south to north) with recorded sea level during the 10 May 2021 meteotsunami are listed, the columns are: its identification code, the island where they are located, the running institution, the maximum wave height (WH), the time of the maximum wave height and the most energetic period during the maximum wave height.

atmospheric pressure oscillations, some oscillations of almost 60 cm are observed. A possible explanation to these strong responses for small atmospheric pressure perturbations is that constant oscillations of 40 cm are found within Ciutadella Harbour that do not need from a huge external forcing to grown until large 60 cm oscillations. More research is needed to explain these relatively large, in comparison with the pressure perturbations, amplitude meteotsunamis produced during 10S3, 10S4 and 10S5.

As has been said, for the other locations no major oscillations are detected, being the maximum wave heights detected of around 40 and 50 cm in PSO, PCO, CPF and ARL (Tab. 4.2). Looking at the atmospheric perturbation (Fig. 4.16) it is worth noticing that, as happens in 23 May, the perturbation is not the same at the north-west stations (PSO and AND), where the pressure jumps are not measured during 10S1 and 10S2, and in the rest of the Island. Then, here we can separate the stations of PSO and AND (north-west) from the rest that have similar perturbation except from smaller details. The propagation speed and direction of the atmospheric perturbation over Mallorca have also been estimated for this event (Fig. 4.15). The propagation speed is ~ 25 m/s during 10S1 and 10S2 and, later, it grows up to ~ 35 at 10S3, 10S4 and 10S5. The estimated direction oscillates between 210° and 250° during the whole event being quite constant during 10S1 (250°), 10S3 (210°) and 10S5 (210°) and with rapid changes in 10S2 (210° to 250°) and in 10S4 (240° to 200°). Thus, the estimated speeds and directions fall within the know range of values that can generate Proudman resonance (Vilibić et al., 2008). We also observe that again the estimated velocity is quite close to the wind velocity at 500 hPa.

The measured atmospheric pressure time series show large differences between the perturbations causing the 10 May and the 23 May meteotsunamis. We now compare the
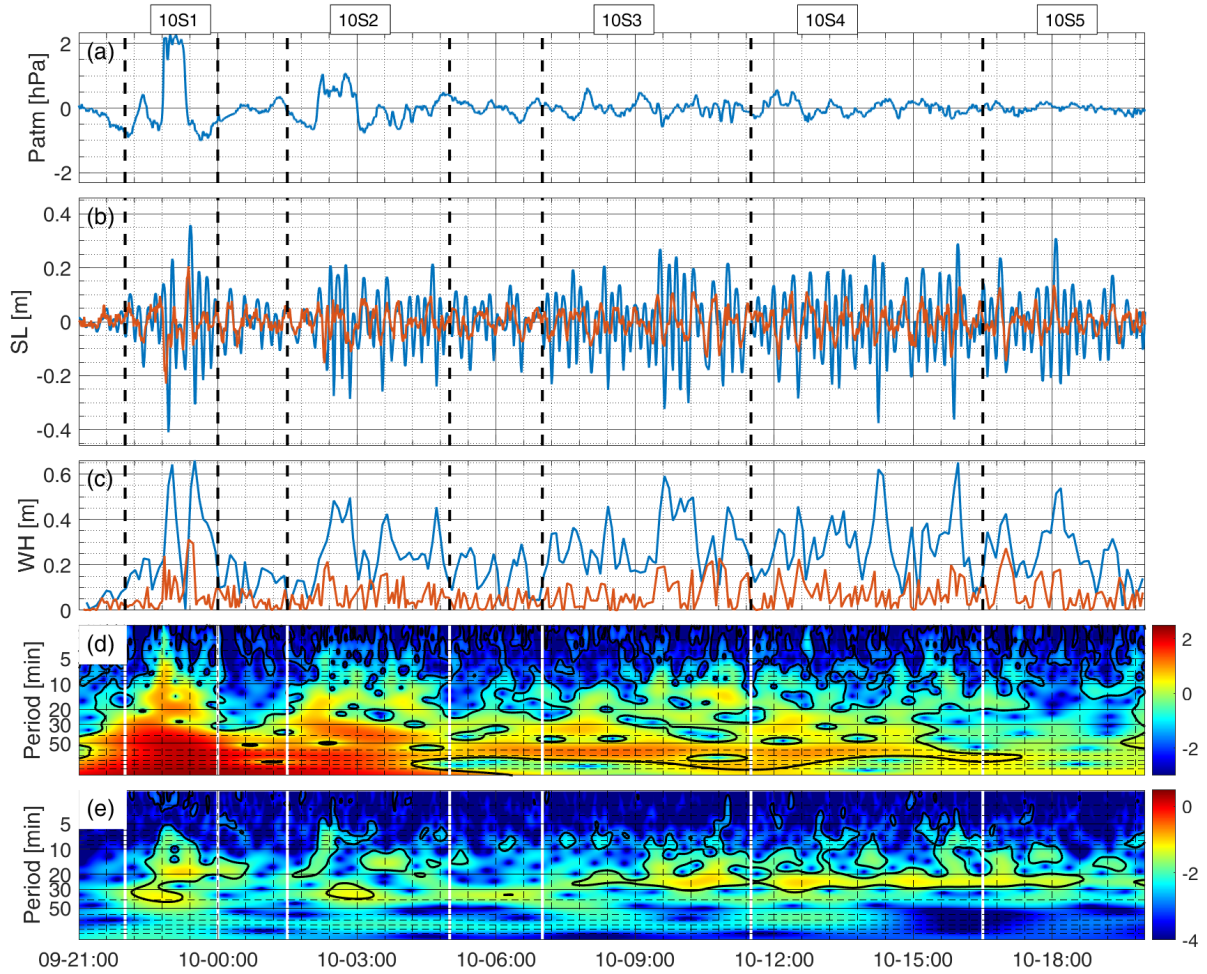
Figure 4.14: Time series measured between 2100 UTC 9 May 2021 and 2000 UTC 10 May 2021. (a) Filtered atmospheric pressure time series measured in Ciutadella and (d) its wavelet power spectrum (colour scale in $\log_{10}([\text{hPa}^2])$). (b) the sea level measured CIU (blue) and at SBL (red). (c) the wave height, computed as the difference between maxima and minima in sea level, for CIU (blue) and SBL (red) time series. (e) the wavelet power spectrum for the SBL time series (colour scale in $\log_{10}([\text{m}^2])$). The vertical lines, black dashed lines in the time series, (a), (b) and (c), and white lines in the power wavelet spectra, (d) and (e), separate the chosen subevents. The black contour in the wavelet power spectra denotes the 95% significance level.

synoptic situation of 10 May with the one observed during 23 May: in Fig. 4.17 we have plotted again the ERA5 reanalysis for the temperature at 850 hPa at (Fig. 4.17a and 4.17c) and the wind at 500 hPa (Fig. 4.17b and 4.17d) for two different times within the 10 may event, at 2300 UTC 9 May (Fig. 4.17a and 4.17b) during 10S1 and at 1000 UTC 10 May (Fig. 4.17c and 4.17d) during 10S3. The plotted fields show the jet at 500 hPa and warm air entrance from the south, usual for meteotsunami events. Nevertheless, they do not coincide in time: at 2300 UTC the high-level jet has not arrived to the Balearic Islands yet, as the warm air has. Later, at 1000 UTC the strongest part of the wind jet has been placed over the Islands with wind speeds over 30 m/s, but the warm air has been displaced to the east and the temperature inversion that stabilizes the lower troposphere has disappeared.

More details on the atmospheric stability can be seen in the vertical sections shown in Fig. 4.18 for the same times as in Fig. 4.17. These atmospheric profiles differ clearly
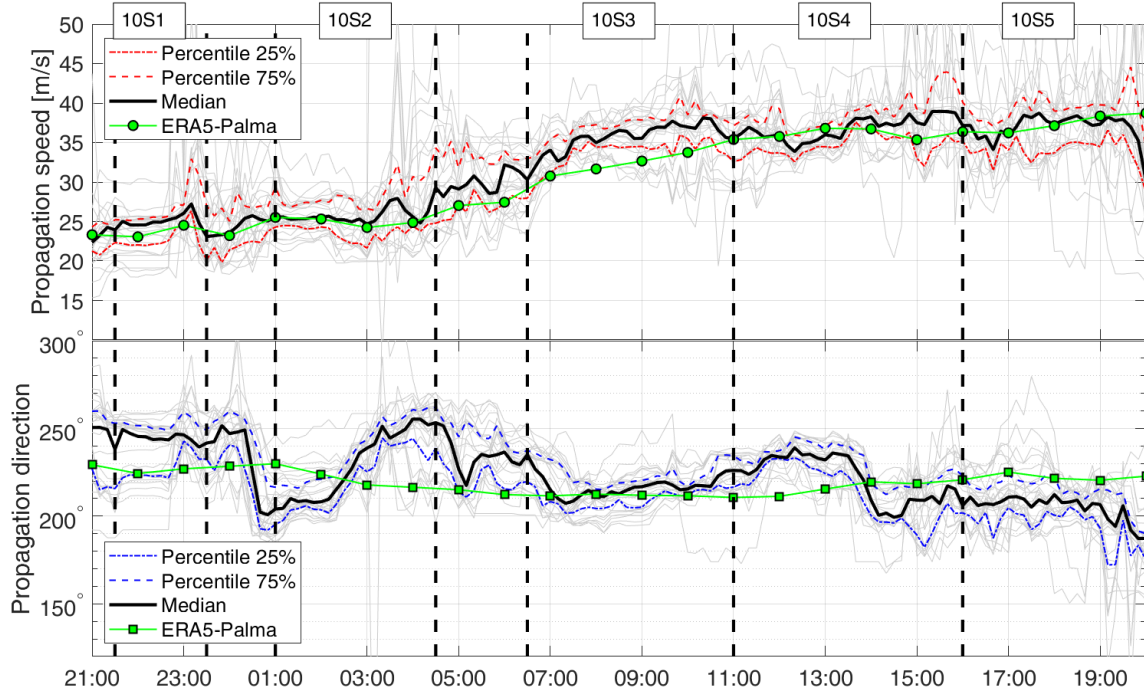
Figure 4.15: Estimated propagation speed (m/s) (top) and direction (degrees from the north) (bottom) between 2100 9 May 2021 and 2000 10 May 2021. The estimation for all stations have been plotted in grey, the median is plotted with the black solid line and the dashed (red for the speed and blue for the direction) lines mark the 25% and 75% percentiles. The green markers represent the speed (top) and direction (bottom) of the wind speed provided by ERA5 reanalysis at 500 hPa at the grid point closest to Palma. The black dashed vertical lines separate the chosen subevents.

from the one shown for the 23 May 2021 meteotsunami which could be related to the creation of a wave duct that allowed the propagation of the atmospheric perturbation. In this case, we see how at 2300 UTC there is a thin stable layer between the surface and 850 hPa over the Balearic Islands followed by a very unstable layer between 850 and 750 with $Ri < 0.5$ but with no important wind shear. Then, between 700 and 600 hPa there is a smooth wind shear that goes from 16 to 24 m/s, it coincides with a Ri below 0.5. It is not clear that this situation can generate a wave duct, since the stable layer is very thin and the wind shear is not too strong. However, the origin of the pressure jump observed on 10S1 may be related with convective activity, since the unstable layer between 850 and 700 is susceptible of developing important vertical air movements. In Fig. 4.19a, it can be seen that the air at the surface is moist and that there is an important amount of CAPE (Convective Available Potential Energy) which would result in a deep convective system if some initialization mechanism, as wind convergence at low levels or a moisture anomaly, appears. The resulting convective system would be responsible for the pressure jumps measured by the meteorological stations of the Balearic Islands at 10S1 and 10S2, and responsible for the sea level oscillations of the meteotsunami event.

Later, the profile of 1000 UTC does not show a situation appropriated for the generation of a wave duct since no stable layer is found near the surface. However, in the atmospheric pressure records some small oscillations appear, causing 50 cm oscillations in Ciutadella. From this vertical profiles, it is hard to find an explanation to the existence of these atmospheric waves beyond the fact that they could be generated by this
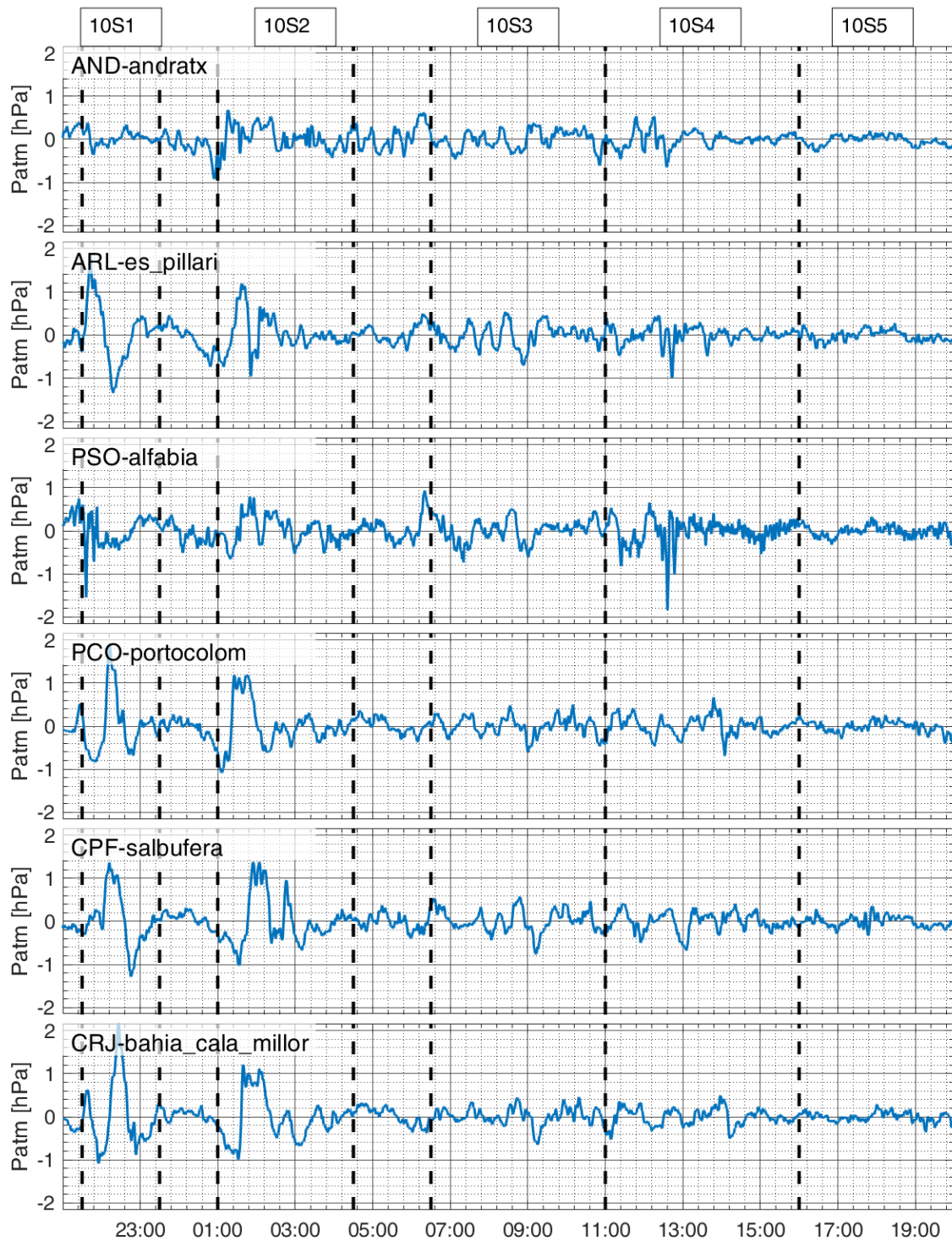
61

Figure 4.16: Filtered atmospheric pressure time series (hPa) measured at the closer barograph to each of the tide gauges of Fig. 4.3, between 2100 UTC 9 May 2021 and 2000 UTC 10 May 2021. The barograph stations are sorted from south (top) to north (bottom): Andratx (AND), Es Pil·larí (ARL), Alfàbia (PSO), Portocolom (PCO), S'Albufera (CPF) and Badia de Cala Millor (CRJ). The black dashed vertical lines separate the chosen subevents.

environment of atmospheric instability.

All in all, this event is an example of a small meteotsunami where the atmospheric

(a) Temperature at 850 hPa (2300 UTC 9 May) (b) Wind at 500 hPa (2300 UTC 9 May)

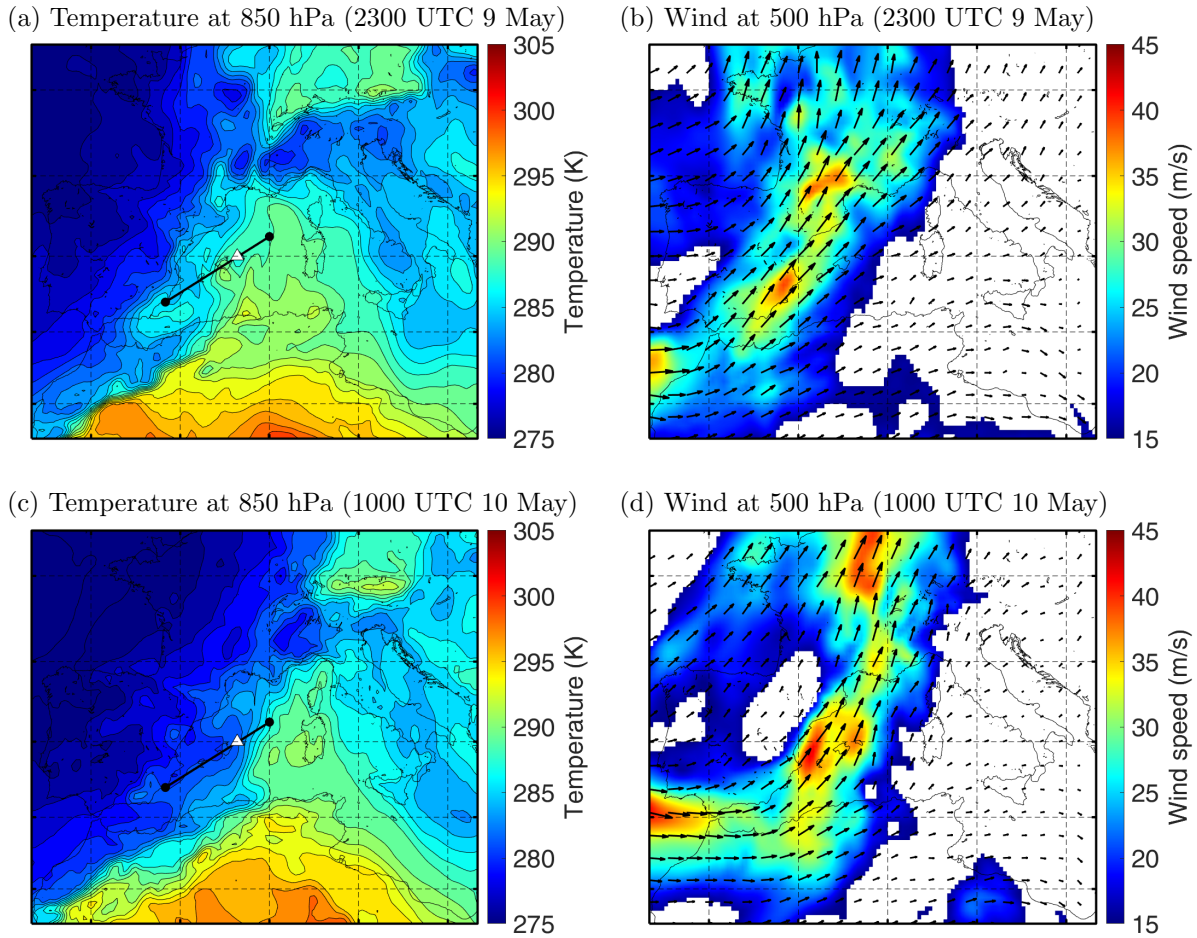(c) Temperature at 850 hPa (1000 UTC 10 May) (d) Wind at 500 hPa (1000 UTC 10 May)

Figure 4.17: Synoptic atmospheric conditions at the Western Mediterranean from ERA5 data, (a) and (b) at 2300 UTC 9 May 2021 and (c) and (d) at 1000 UTC 10 May 2021. (a) and (c) temperature (K) at 850 hPa. The black line marks the section shown in Fig. 4.18 and the white triangle the location of Ciutadella. (b) and (d) wind at 500 hPa, the wind speed (m/s) is indicated with the plot colour, in the white areas the wind speeds are below 15 m/s.

conditions do not seem the best to the meteotsunami generation. However, even for very small pressure oscillations which an unclear propagation mechanism, sea level oscillations of more than 50 cm are measured in Ciutadella.

4.2.2 18 June 2021

Finally, we include in this meteotsunami collection, the event occurred during the weekend that lasted from 18 to 20 of June 2021. Unfortunately, most of the data from VENOM tide gauges have not been recovered yet, therefore no detailed description of the event over the whole Balearic basin can be provided here. Nevertheless, the magnitude and the duration of the event are worth commenting.

In Fig. 4.20 we have plotted the time series for the sea level and the atmospheric perturbation measured in Ciutadella, there the subevents chosen to study the event have been market with vertical lines. The estimated speed and direction of the atmospheric perturbation for this event can be found in Fig. 4.21. We can see how the oscillations last for a long time, 36 hours, with amplitude over 40 cm without almost any interruption.

(a) 2300 UTC 9 May 2021
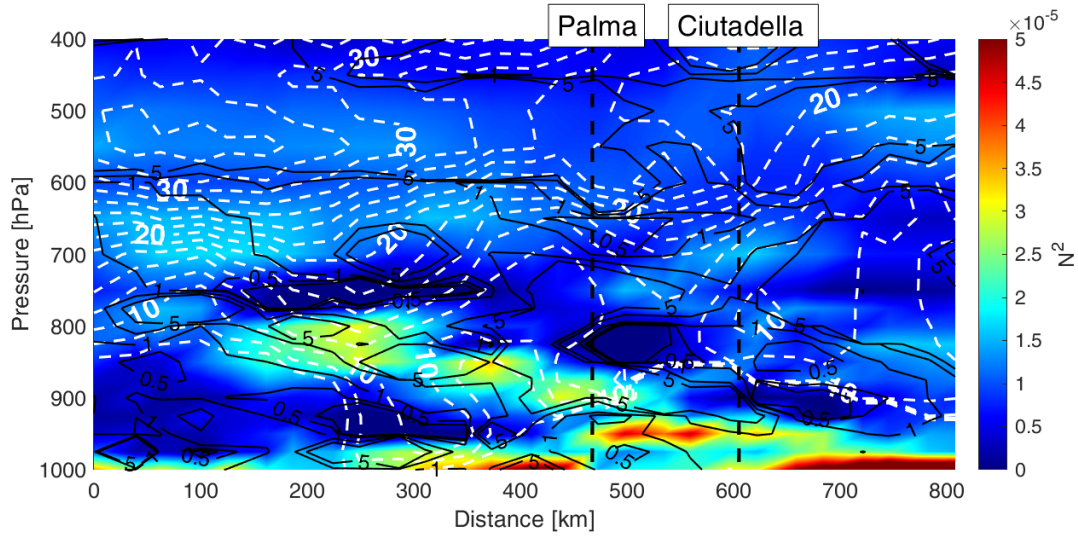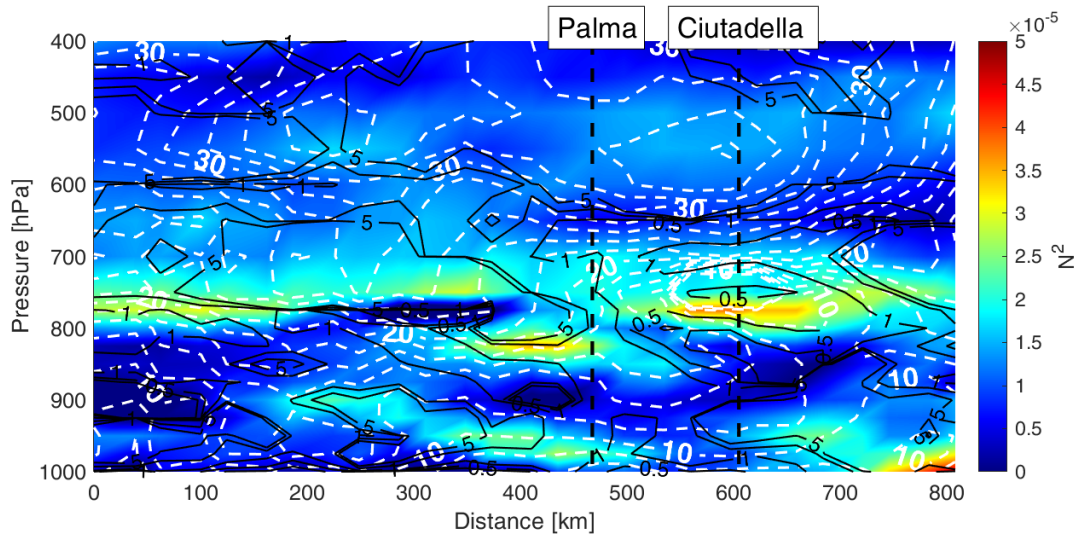

(b) 1000 UTC 10 May 2021

Figure 4.18: Vertical 2D atmospheric profile for the section indicated in Fig. 4.17, (a) at 2300 UTC 9 May 2021 and (b) at 1000 UTC 10 May 2021. The shown variables are the Brunt-Väisälä frequency (N^2) in s^{-1} (plot colour); the Richardson number (black contours; levels 0.25, 0.5, 1 and 5 are indicated); and the wind speed at the direction 228°, the direction of entrance of the Ciutadella Harbour (white contours, every 2 m/s). The two dashed lines show the location of Palma, Mallorca, and Ciutadella, Menorca, from left to right.

The event is characterized by two main peaks larger than 70 cm, the first one of 115 cm at 1800 UTC 18 June (18S1) and the second one of 90 cm at 2030 UTC 19 June (18S4). The large oscillation of 18S1 is caused by a 1 hPa amplitude atmospheric wave with energy between 20 and 10 min period with 30 m/s of phase speed and with direction 210° that has two complete cycles. This fact seems key to the large amplitude of this meteotsunami since the amplitude of the pressure oscillation is not extraordinary, therefore, the large amplitude could be caused by the accumulation of energy at the normal frequency of the harbour. The 18S4 oscillation is caused by a rapid 3 hPa pressure fall that travels at 30 m/s with direction 220°, and just one major oscillation occurs in Ciutadella. In 18S2 there are also two moments when the atmospheric perturbation has energy around 10 min when sea level oscillation reach 60 cm, at this subevent the perturbation propagation

64

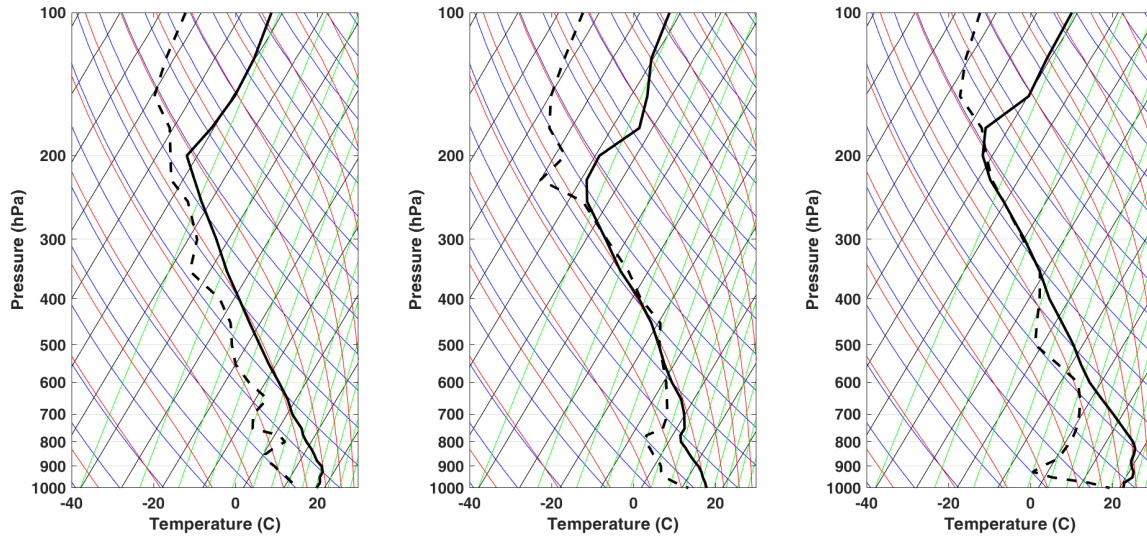(a) 2300 UTC 9 May 2021   (b) 1000 UTC 10 May 2021   (c) 1800 UTC 18 June 2021

Figure 4.19: Skew-T thermodynamic diagrams for the temperature (°C), black solid line, and the dew point temperature (°C), black dashed line, for the ERA5 vertical profile at the grid point closest to Ciutadella. The coloured lines are: isotherms (green), dry adiabatics (blue), and moist adiabatics (red). (a) at 2300 UTC 9 May 2021. (b) at 1000 UTC 10 May 2021. (c) at 1800 UTC 18 June 2021

speed oscillates between 28 and 30 m/s and the propagation direction changes between 200° and 220°. Finally, in 18S5 there is a quick pressure fall of 4 hPa with an estimated speed of 40 m/s and a direction of 220° that generates an oscillation of just 69 cm. We notice that the subevent with smaller oscillations, 18S3, is the one that has an estimated atmospheric perturbation propagation speed ($\sim$17 m/s) that does not match the free wave propagation speed in the Menorca Channel (24 - 36 m/s), which leads to a poor open sea amplification.

The observation of the synoptic situation for this event (Fig. 4.22 and Fig. 4.23) shows that there is an entrance of warm air over the Balearic Islands with temperature between 290 K and 295 K for two days from 0900 UTC 18 June to 0900 UTC 20 June. This situation cause a thermal inversion between 900 and 850 hPa that raises the stability of the lower layer of the troposphere. Then, at upper levels, a jet of wind pointing towards the north-east with values between 20 and 24 m/s is found. This jet may be accompanied by low Ri under 0.5 which leads to the conclusion that the conditions are suitable for the formation of a wave duct. Looking at the thermodynamic Skew-T diagrams for this event (Fig. 4.19c), it is also found that an important amount of CAPE is available, which could result in convective movements in the upper levels. This convection at upper levels can be initialized by atmospheric waves and provide energy to the wave propagation, resulting in wave propagation by wave-CISK interaction. All in all, for this event, we find that the atmospheric conditions are convenient to the formation of a wave duct and to wave-CISK mechanisms that favour the formation and propagation of the atmospheric perturbation that causes the observed meteotsunamis.

This third event is very interesting since it lasts during a large time interval with contains different atmospheric perturbations with different characteristics that condition the different amplitude of the sea level response. Comparing these subevents with those of
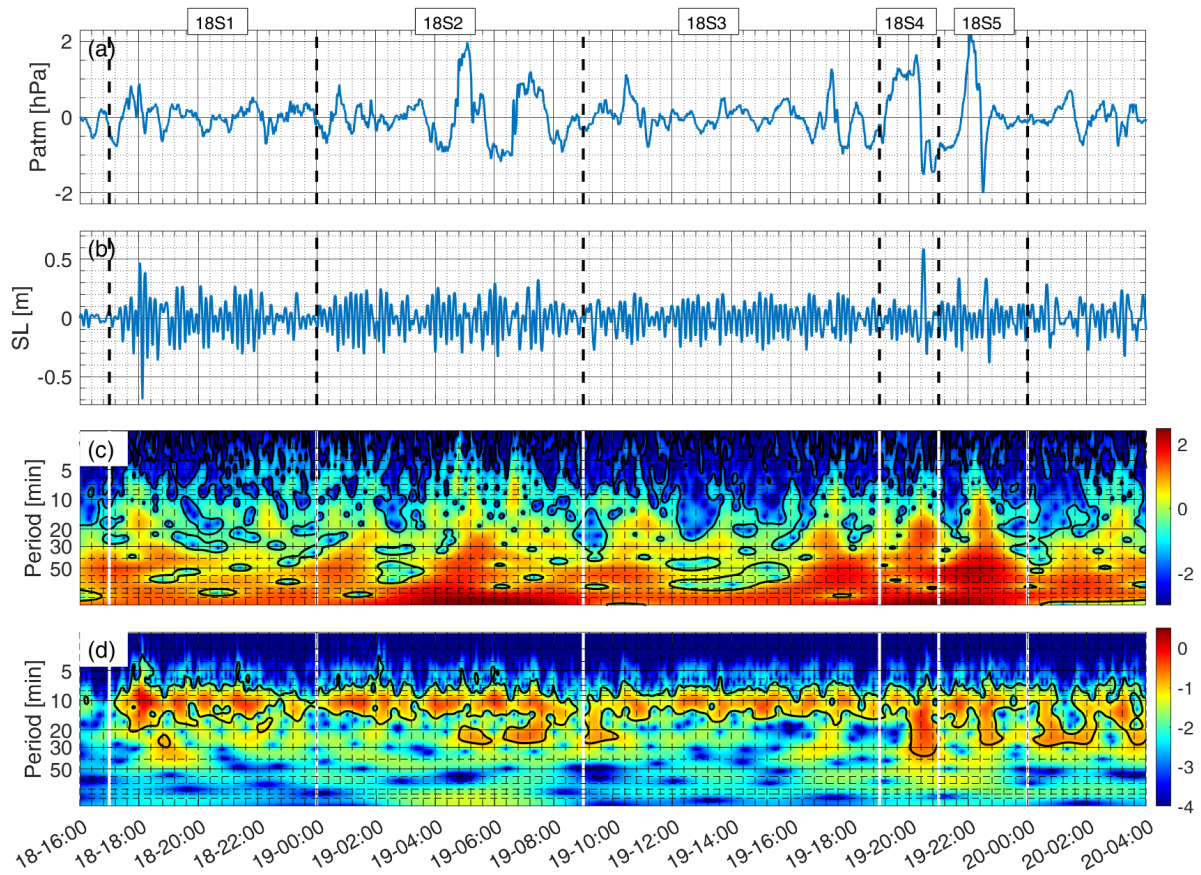
65

Figure 4.20: (a) Filtered atmospheric pressure time series (hPa) measured at Ciutadella between 1600 UTC 18 June 2021 and 0400 UTC 20 June 2021, this time is shared by all subplots. (b) Filtered sea level time series (m) measured by the tide gauge within Ciutadella Harbour. (c) Wavelet power spectrum of the measured atmospheric pressure (colour scale in $\log_{10}([\text{hPa}^2])$). (d) Wavelet power spectrum of the measured sea level (colour scale in $\log_{10}([\text{m}^2])$). The vertical lines, dashed black lines in the time series, (a) and (b), and white lines in the power wavelet spectra, (c) and (d), separate the chosen subevents. The black contour in the wavelet power spectra denotes the 95% significance level.

10 and 23 May 2021 the key features of the atmospheric perturbation that affect the meteotsunami amplitude will be addressed. With the three meteotsunami events presented, a good set of different atmospheric disturbances and subsequent sea level responses has been gathered to discuss if the observations are consistent with the generation mechanism presented in Chap. 2.
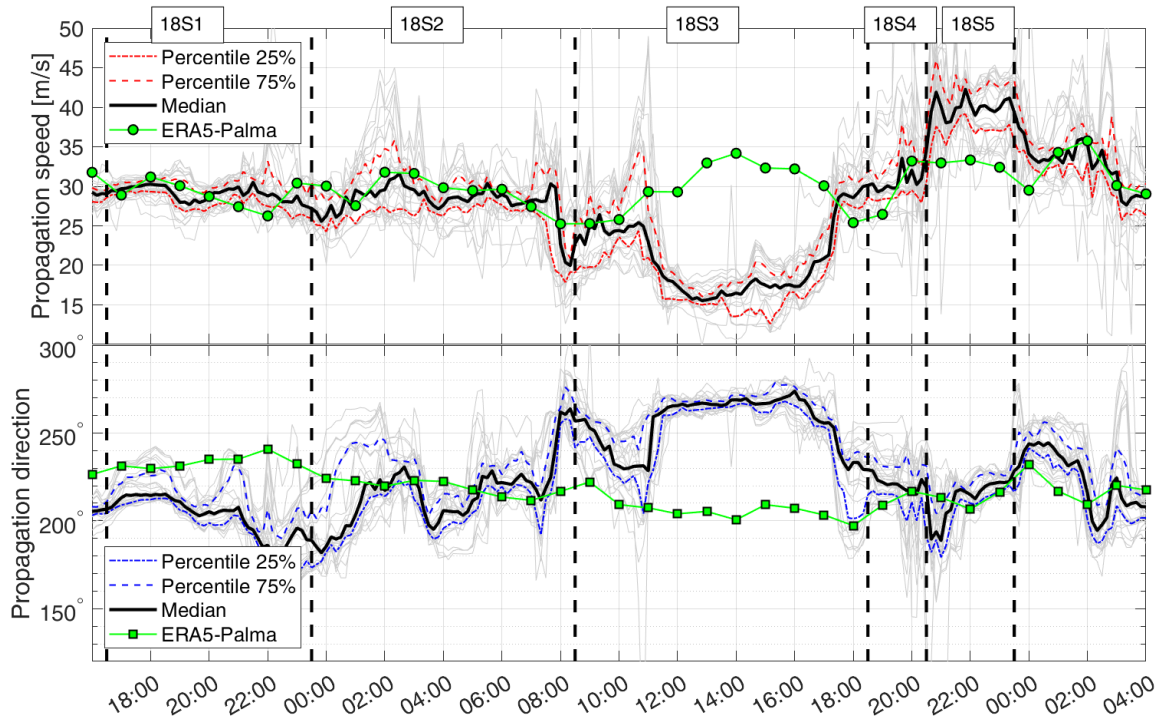
Figure 4.21: Estimated propagation speed (m/s) (top) and direction (degrees from the north) (bottom) between 1600 18 June 2021 and 0400 20 June 2021. The estimation for all stations have been plotted in grey, the median is plotted with the black solid line and the dashed (red for the speed and blue for the direction) lines mark the 25% and 75% percentiles. The green markers represent the speed (top) and direction (bottom) of the wind speed provided by ERA5 reanalysis at 500 hPa at the grid point closest to Palma. The black dashed vertical lines separate the chosen subevents.

(a) Temperature at 850 hPa (2300 UTC 9 May)   (b) Wind at 500 hPa (2300 UTC 9 May)
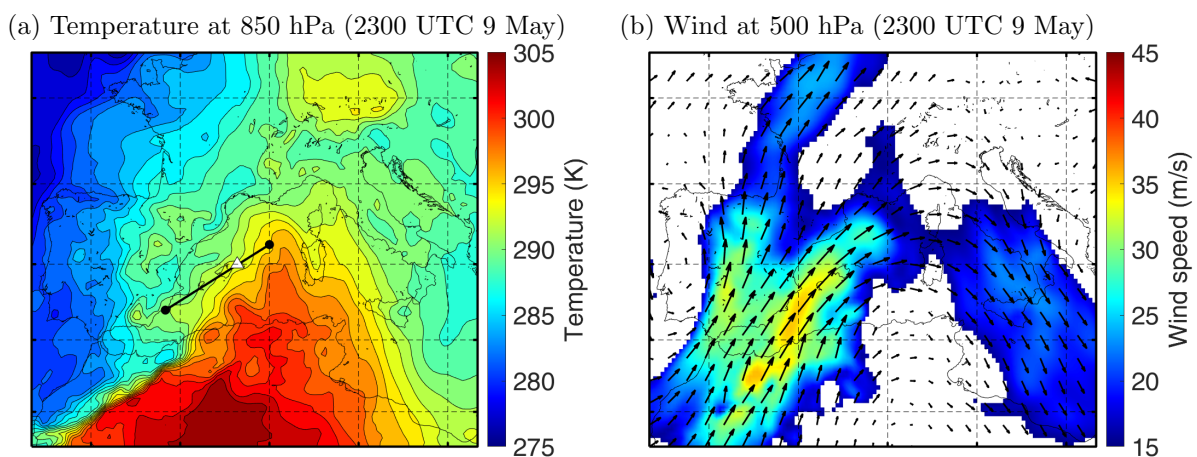
Figure 4.22: Synoptic atmospheric conditions at the Western Mediterranean from ERA5 data, at 1800 UTC 18 June 2021. (a) temperature (K) at 850 hPa. The black line marks the section shown in Fig. 4.23 and the white triangle the location of Ciutadella. (b) wind at 500 hPa, the wind speed (m/s) is indicated with the plot colour, in the white areas the wind speeds are below 15 m/s.
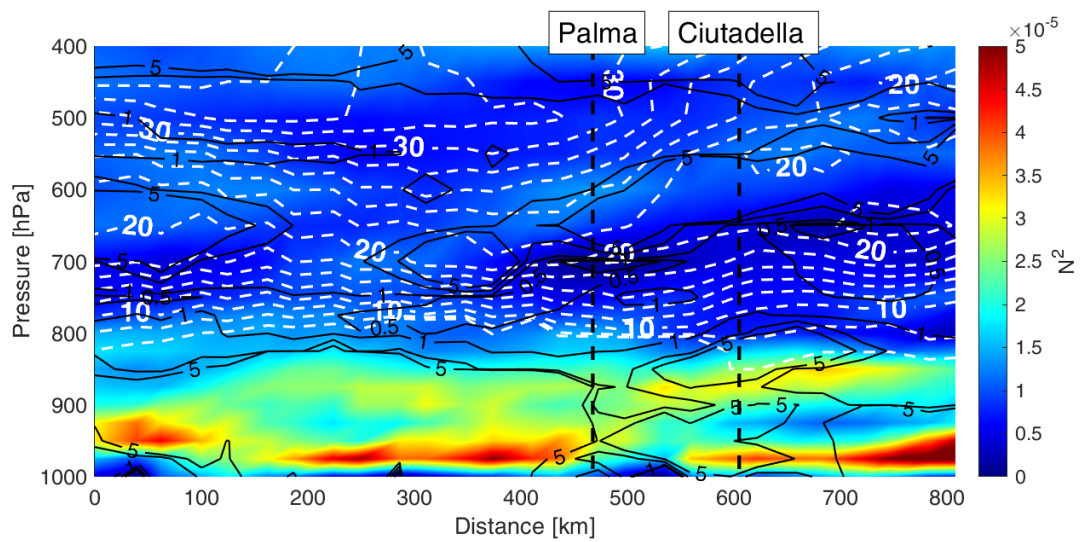
Figure 4.23: Vertical 2D atmospheric profile for the section indicated in Fig. 4.22, at 1800 UTC 18 June 2021. The shown variables are the Brunt-Väisälä frequency (N^2) in s^{-1} (plot colour); the Richardson number (black contours; levels 0.25, 0.5, 1 and 5 are indicated); and the wind speed at the direction 228°, the direction of entrance of the Ciutadella Harbour (white contours, every 2 m/s). The two dashed lines show the location of Palma, Mallorca, and Ciutadella, Menorca, from left to right.

Chapter 5

Discussion

Our goal in this chapter is to review if our new observations are consistent with the established meteotsunami generation mechanism (detailed in Chap. 2), and to outline the unclear features that should be addressed in further research. The atmospheric synoptic pattern and the mechanisms of generation and propagation of the observed atmospheric perturbations will be commented in Sect. 5.1. Then, in Sect. 5.2, the sea level response will be compared with its atmospheric counterpart, the importance of harbour resonance will be detailed and the study of the meteotsunami sea wave propagation will be analysed.

5.1   Atmospheric origin of the meteotsunamis

A. Synoptic pattern

For the three meteotsunami events reported in this work, the traditional synoptic pattern for meteotsunamis in Ciutadella, described in Sect. 2.1.1, has been recognized, at least to some point. For the three cases, an entrance of African warm air between 900 and 850 hPa is observed, being the event of 18 June the one with higher temperatures. In the 10 May event we can observe the clear relation between the amplitude of the atmospheric perturbation and the presence of this warm air that causes an inversion at the lower troposphere since for 10S1 and 10S2 the inversion is present and important pressure jumps are measured at the surface (1.5 - 2.5 hPa). Later, in 10S3, 10S4, and 10S5, when the warm air mass has been substituted by cooler air coming from the north-west, the amplitude of the atmospheric perturbations is clearly smaller (1 hPa).

The results obtained reinforce the idea that major or smaller fulfilment of the optimal synoptic conditions for the occurrence of the meteotsunami affects the final amplitude of the event. This idea was first explored in a quantitative way by Šepić et al. (2016), where an index that related the synoptic conditions from ERA-Interin data to the amplitude of the sea level oscillations in Ciutadella was created. The index took into account five factors: *i*) the vertical wind shear over Ciutadella, *ii*) the presence of a low pressure at surface level, *iii*) the difference of temperature between 850 hPa and 900hPa caused by the thermal inversion, *iv*) the moisture at high levels, and *v*) the geopotential gradient at high levels, related to the wind speed. They concluded that a certain threshold in the index had to be surpassed to the occurrence of meteotsunamis in Ciutadella. However, it is clearly not a sufficient condition, since only in the 20% of cases with the index surpassing the threshold a meteotsunami occurred. They also found that if the index increased, the provability of having a larger meteotsunami also increased. The 3 cases analysed in this

study follow that same rule, in the two cases with more optimal synoptic situations (23 May and 18 June) a larger meteotsunami occur than for 10 May. However, it has to be kept in mind that the number of cases analysed is not enough to fully confirm the Šepić et al. (2016) conclusions.

B. *Generation and propagation mechanisms*

The synoptic pattern offers the conditions for the appearance of generation and propagation mechanisms of atmospheric pressure perturbations. The main mechanisms for the propagation of atmospheric disturbances related to meteotsunamis are the wave ducting (Monserrat and Thorpe, 1996) and the wave-CISK (Belušić et al., 2007) (described in Sect. 2.1.2). One of our goals is to validate if the atmospheric environment is suitable for existence of at least one of these mechanisms during the reported meteotsunami events.

During most of the 23 May event it is clear that the vertical profile is adequate for the formation of a wave duct since a stable layer is found at lower levels capped by a layer of lower Ri and strong wind shear. According to the wave duct theory, the phase speed of the atmospheric perturbation has to equal the wind speed at some level within the capping unstable layer to create an overreflecting critical level. Thus, the estimated propagation velocity should be close to the wind velocities provided by ERA5 in the capping layer. Comparing the estimated velocity for the disturbance and the wind velocity at 500 hPa (Fig. 4.8) we see how this matching is confirmed during most part of the event, reinforcing the hypothesis of the existence of a wave duct. In some intervals, 23S3, 23S4 and 23S5, we find that the estimated velocity is smaller than the wind speed at 500, which indicates that the critical level is found below 500 hPa where the wind speed is smaller.

For 10 May the formation of a stable layer at the lower troposphere is only found during 10S1 and 10S2, and it is not as clear as in 23 May that the conditions for the formation of a wave duct are present. Meanwhile, the vertical thermodynamic profile (Fig. 4.19a) shows an important amount of available CAPE that could result in the formation of a convective system responsible for the rapid pressure jumps measured during 10S1 and 10S2. Finally, 18 June presents a lower stable layer capped by a layer with smaller Ri and a stronger wind shear that may form a wave duct. It is also observed that CAPE is available, which could lead into wave-CISK interaction as propagation mechanism in combination with the wave duct.

From ERA5 data we only can speculate on which could be the generation and propagation mechanism of the atmospheric perturbations from the description of the atmospheric environment, since the reduced resolution of the reanalysis (~ 30 km) does not allow us to see the small mesoscale perturbations that are measured by the barographs at the surface. More numerical experiments, like the performed by Belušić et al. (2007) and Šepić et al. (2009), could help to understand the generation of the atmospheric perturbation that cause meteotsunamis. However, even these high resolution numerical models have problems to reproduce the mesoscale atmospheric perturbations in detail, failing to reproduce the spectral energy distributions and the time distribution of the disturbances, as happens with the SOCIB's BRIFS (Mourre et al., 2020). The precise reproduction of the atmospherical disturbances by high-resolution numerical models is one of the issues to be tackled if we want to increase the reliability of the meteotsunami forecasting systems.

Summarizing, the synoptic pattern observed during the 3 events is the expected during Balearic meteotsunamis according to the previous studies (Ramis and Jansà, 1983; Šepić

et al., 2016). Furthermore, favourable conditions for the formation of the wave duct are clearly detected during 23 May and 18 June 2021 events. In these same events, the existence of the wave-CISK interaction can not be discarded, therefore both mechanism could be responsible for the perturbation propagation. Otherwise, during 10 May 2021 event the existence of a wave duct does not seem likely and the formation of the perturbations is provably caused by the propagation of a convective system.

5.2 Ocean wave amplification

A. Atmosphere-ocean energy transfer

One of the main issues that we want to address is how the different atmospheric perturbation parameters affect the final meteotsunami amplitude. As it is explained in detail in Chap 2, the meteotsunamis in Ciutadella are caused by atmospheric perturbations that have energy at periods close to 10.5 min (Rabinovich and Monserrat, 1998), the normal mode of the harbour; that travel towards the entrance of the harbour, with directions between 210° and 260°, with speed that matches the free wave speed in the Menorca Channel, 24 - 36 m/s (Vilibić et al., 2008; Ličer et al., 2017); and that are intense enough to produce strong sea level responses. Thus, we are going to analyse the characteristics of the atmospheric disturbances and how they affect the amplitude of the sea level oscillations in Ciutadella. First, we are going to observe if the spectral energy distribution is the expected. Second, the relationship between the propagation direction and speed of the perturbation and the meteotsunami amplitude will be outlined, and, finally, the role of the perturbation amplitude will be discussed.

A.1. Spectral energy distribution

The first step in the amplification mechanism of the sea wave is the amplification at open sea, mainly by Proudman resonance. Thus, we have to study how the spectrum of the sea response is affected by this process. According to the sea wave generation mechanism introduced in Sect. 2.2.1, the spectral energy distribution of the sea level response generated by inverse barometer should be the same as the one of the atmospheric perturbation. However, the amplification at open sea by Proudman resonance alter the spectral energy distribution of the sea response since the amplification is larger for the higher frequency modes. This result is obtained from Eq. 2.20, the perturbations with higher frequency (or steeper pressure jumps) will have a larger first derivative which will result in a larger amplification by Proudman. This phenomenon can be observed in ports with weak topographical response, as Son Blanc (SBL): in Fig. 4.11 and 4.14 the panels d and e show the wavelet power spectrum for the atmospheric perturbation and for the sea level, respectively, and it can be noticed that the peaks in the wavelet power spectrum of SBL only coincide with those peaks in the wavelet power spectrum of the atmospheric perturbation for periods below 50 min. Thus, Proudman resonance at open sea would act as a high pass filter that amplifies only the high-frequency modes in the sea level response. More research is needed to confirm this hypothesis because these results could also be the consequence of some topographical response that we are not taking into account.

The spectral energy distribution of the forcing is key when we are addressing harbour resonance. The largest amplification within a harbour is produced when the external forcing have a peak of energy at the normal oscillation frequency of the harbour. In the

case of Ciutadella Harbour, that has its normal period of oscillation at ~10.5 min, the amplification would be maxima when the forcing wave has a spectral peak at ~10.5 min of period. As it has been introduced above, the spectral energy of the incoming sea wave will depend on the spectral energy of the atmospheric disturbance, thus, there should be a direct relation between the spectral energy of the atmospheric perturbation at the normal period of the harbour and the amplification produced by harbour resonance. This idea was explored by Rabinovich and Monserrat (1998), they compared the variability of the atmospheric perturbation with period near 10.5 min with the variability of the sea level oscillation in Ciutadella for the same periods for one meteotsunami event of 7 days and for a calm period of 43 days. They obtained a 0.93 correlation coefficient between the sea level and the atmospheric variabilities at 10.5 min during the meteotsunami event, and a correlation coefficient of 0.53 for the calm period. Both correlations were higher than the correlation between the variabilities of the original time series.

We can repeat their experiment by defining the variability in a certain frequency band $[T_n - \Delta T/2, T_n + \Delta T/2]$ of the time series as:

$$\hat{\sigma}(t_k, T_n) = \left[\frac{1}{N} \sum_{i=k-N/2}^{k+N/2} \left(\sum_{T_j=T_n-\Delta T/2}^{T_n+\Delta T/2} |W(t_i, T_j)|^2 \right) \right]^{\frac{1}{2}} \tag{5.1}$$

where T_n is the central period, t_k is the moment in time, N is the length of the time window that we are using to average ($N\Delta t$ is the length in time), ΔT is the length of the period window, and $|W(t_i, T_j)^2|$ is the wavelet power as a function of time and period. $\hat{\sigma}$ is proportional to the square root of the energy around a certain period T_n at instant t_k. The technique used in Rabinovich and Monserrat (1998) was quite similar, and they used a time averaging window of 256 min. In Fig. 5.1 we have plotted the scatter plot of the sea level variability at a $T_n = 10$ min and with period window length $\Delta T = 10$ min as function of the variability (centred around the same period and period window) of the atmospheric pressure time series, both measured in Ciutadella between 1 November 2018 and 21 June 2021, which include 20 meteotsunami events. We have separated the meteotsunami events (blue) from the calm periods (red). The meteotsunami events have been selected by finding the point over the 98% percentile in sea level amplitude and selecting the period surrounding them as part of the event. The same plot has been made, changing the averaging window from 4 hours, in Fig. 5.1a, to 30 min, in Fig. 5.1b, and important differences can be appreciated.

Comparing the results from Fig. 5.1a with those of Rabinovich and Monserrat (1998), we note that the correlation obtained during meteotsunami events is higher in their experiment, because they have just only one meteotsunami event while here we consider 20 different meteotsunami events. Even so, the 0.81 obtained correlation between the variability of the atmospheric pressure and of the sea level around the 10.5 min period is a good proof of the importance of having a large amount of energy at this frequency to have a severe sea level response in Ciutadella. In calm periods, the correlation obtained here is higher than the one obtained by Rabinovich and Monserrat (1998), though it continues denoting an important decrease with respect to the periods with meteotsunamis. We also note that the different slopes in the regressions that clearly denote a major amplification during meteotsunami events. This could be a consequence of adding the amplification produced at open sea during meteotsunami events. When comparing Fig. 5.1a and Fig. 5.1b we see that when we reduce the averaging time interval length we lose correlation between both time series, from 0.81 to 0.64. It can also be observed in the cases presented

(a) 240 min averaging window
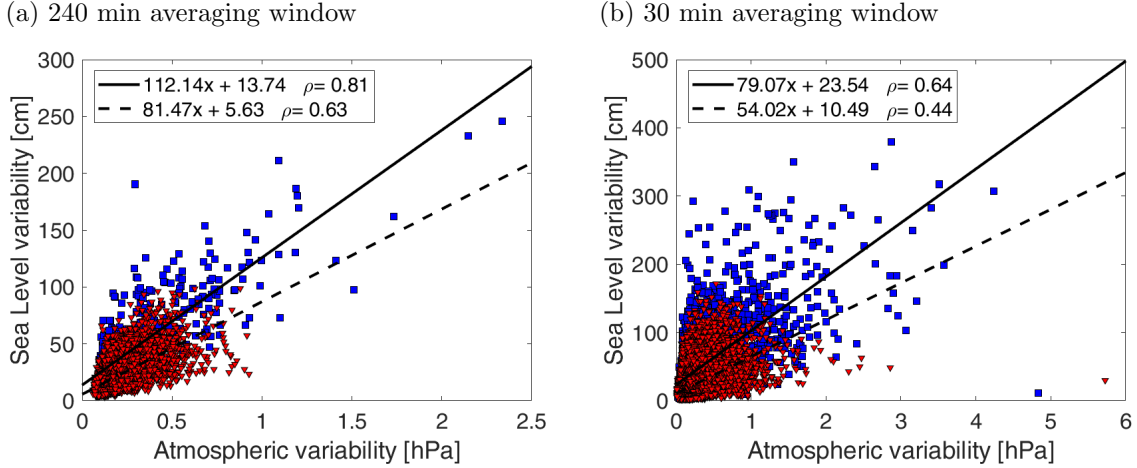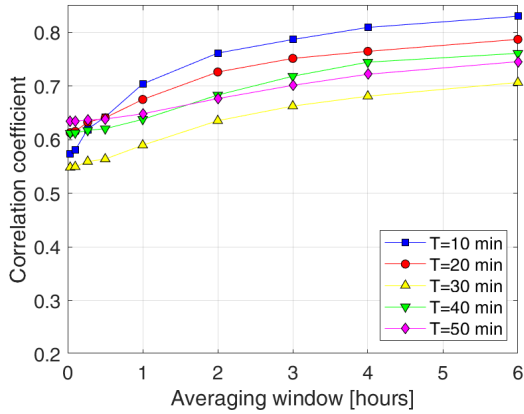
(b) 30 min averaging window

Figure 5.1: Sea level variability (cm) (for the time series measured between 1 November 2018 and 21 June 2021) as a function of the simultaneous atmospheric pressure variability (hPa) for the frequency band with periods between 5 and 15 min. Red triangles correspond to calm periods and blue squares correspond to the meteotsunami events. The solid black line is the linear regression for the meteotsunami events and the dashed black line the same for the calm periods. The regression coefficients are shown in the legend, together with the correlation coefficient for the meteotsunami events (above) and for the calm periods (below). (a) the averaging window length is 240 min ($N = 240$). (b) the averaging window length is 30 min ($N = 30$).

in Chap. 4, for instance, during 10S4 large oscillations are measured in CIU without any important energy close to 10 min in the atmospheric counterpart, and in 18S2 that has several energy peaks at high frequencies for the atmospheric perturbation that cause a weak sea level response. Using shorter averaging windows, the time series of sea level and atmospheric pressure variabilities show clear differences, some peaks coincide in time but have very different amplitude, and some other peaks in atmospheric pressure variabilities have no response in sea level, or vice versa. In other words, it looks like the energy in the atmosphere is transmitted to the sea sooner or later (i.e. when using a 4h window), but not necessarily instantaneously (i.e. when using the 30 min window there is lower correlation).

In Fig. 5.2, we have plotted the correlation (up) and regression (down) coefficients between the sea level and atmospheric pressure variabilities for different frequency bands and different averaging windows for meteotsunami events (left) and for calm periods (right). We can generalize the conclusions reached above analysing Fig. 5.1: if we increase the averaging window length the correlation coefficient and the regression coefficient also increases, and the correlation and the regression are both higher for meteotsunami events than for calm periods. When comparing frequency bands we can observe that the correlation decreases with the period except for the 30 min period that shows correlations smaller than the rest of frequency bands during meteotsunami events. We can also see that the correlation of the 20 min band is very high, close to the 10 min band, for the meteotsunami events and even larger for the calm periods. The regression coefficient is a measure of the amplification between the atmospheric pressure and the sea level: if no amplification was present, the regression coefficient should be around 1 since 1 hPa would cause a sea level response of 1 cm. The fact that for meteotsunami events, the regression coefficient for $T = 10$ min is around 100 means that a perturbation of 1 hPa with an oscillation period close to 10 min would cause a 1 m sea level response of Ciutadella. This

estimation is correct in order of magnitude but too large since we detect a lot of pressure jumps of around 2 hPa that just cause sea level response between 50 and 100 cm. The fact that the estimated regression coefficient is larger is caused by the integration in time that we have used to compute the variability. In the shown atmospheric pressure time series we can see how most atmospheric perturbations, as pressure jumps or large oscillations, are of short duration, meanwhile the sea level responses last longer since the oscillations get trapped within the harbour. This leads to an increase of the variability computed for the sea level in comparison with the computed for the atmospheric pressure as we increase the averaging time. From Fig. 5.2c and 5.2d it is also clear that the Ciutadella Harbour amplifies its natural mode at 10.5 min the most and that as the further we go from this mode the amplification is smaller. Comparing these two subplots, we can also observe the different in regression coefficients between meteotsunami events and calm periods, at least part of this amplification difference could be attributed to the presence of open sea amplification only during meteotsunami events.

(a) Meteotsunami events correlations

(b) Calm period correlations
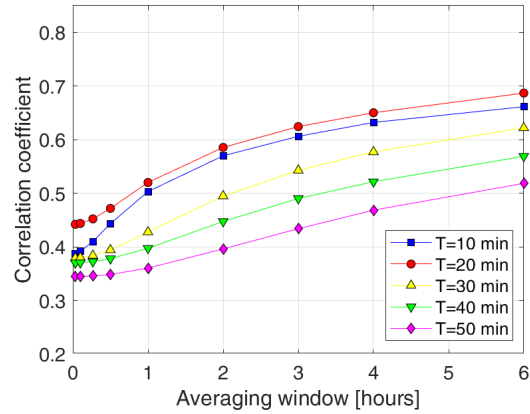
(c) Meteotsunami events regression slopes
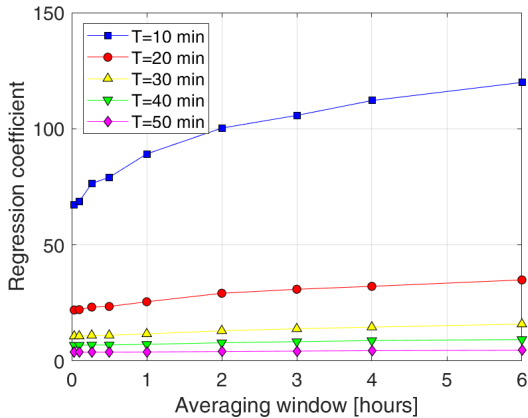
(d) Calm period regression slopes
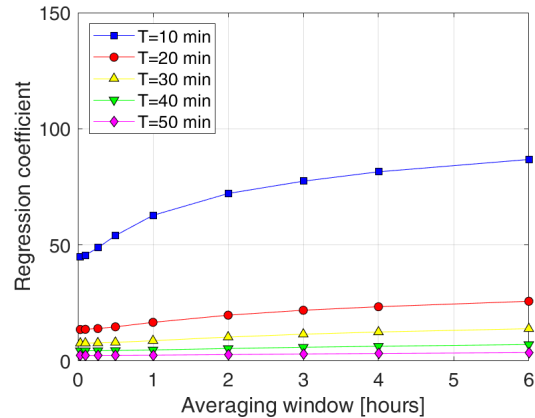
Figure 5.2: (a) and (b) show the correlation coefficient between the sea level variability and the atmospheric pressure variability (for the time series measured between 1 November 2018 and 21 June 2021) as function of the length of the averaging window. Five different frequency bands are plotted, all of them have a period window $\Delta T = 10$ min and the central periods are 10 min (blue), 20 min (red), 30 min (yellow), 40 min (green), 50 min (magenta). (c) and (d) show the regression slope between the sea level variability and the atmospheric pressure variability as function of the length of the averaging window for the same frequency bands.

A.2. Perturbation velocity

The amplification by Proudman resonance is determined by the matching between the perturbation velocity and the free sea wave velocity ($c = \sqrt{gh}$). Thus, thanks to the estimation of the atmospheric propagation velocity, we can analyse the effect of the propagation speed and direction on the meteotsunami amplitude. From previous numerical studies (e.g., Vilibić et al. (2008); Ličer et al. (2017)) we know that, *a priori*, the maximum amplification is given for atmospheric perturbations propagating with phase speed between 23 and 36 m/s and with propagation angles 210° - 260°. These results are consistent with the velocities estimated in other observational studies during meteotsunami events (Monserrat and Thorpe, 1992; Jansa et al., 2007). In the cases presented here, we have also computed the atmospheric perturbation velocity as function of time for each event (Fig. 4.8, 4.15 and 4.21) and the obtained speeds and directions fall within the known margin that allows the occurrence of Proudman resonance. The most noticeable exception is the subevent 18S5 for which the propagation speed has been estimated as 40 m/s, above the speeds acknowledged to produce large open sea amplifications (Vilibić et al., 2008). In fact, for this event, a pressure fall of 4 hPa causes a relatively small sea level response of 71 cm. Although that sea level oscillation is severe and can be considered as a moderate meteotsunami, during the same event oscillations of 1.5 hPa and 3 hPa had caused sea level responses of 115 and 90 cm, respectively.

One of the results obtained is the high variability on the propagation speed and direction of the perturbation. From the estimation of the propagation velocity for the atmospheric perturbation as function of time, we observe that during the event the direction and speed of the perturbation suffer from important changes. During 10 May the computed speed ranges from 22 to 37 m/s (Fig. 4.15), 23 May estimations go from 28 to 35 m/s (Fig. 4.8) and during the 18 June the perturbation velocity reaches minimum values around 17 m/s during 18S3 and maximum values around 40 m/s during 18S5 (Fig. 4.21). Therefore, it seems plausible to relate the weaker sea level oscillations measured for these two subevents to the fact that the atmospheric speed velocities fall beyond the interval of perturbation speed known to cause large Proudman amplifications in the Menorca Channel. In the literature, most observational studies compute the propagation velocity just once assuming that it is stationary for the whole event (e.g, Orlic (1980); Monserrat and Thorpe (1992); Jansa et al. (2007)) and in numerical simulations when artificial atmospheric perturbations are used, the introduced perturbation velocity also have constant speed and direction (e.g., Orlić et al. (2010); Ličer et al. (2017)). The results presented suggest that the assumption of a constant velocity is too restrictive, since we detect variations of 10 to 20 m/s in speed and 50° to 90° in direction within the same event for the median estimated velocity. These variations would be even larger if considering the spatial variability of the estimated velocities. Further research, using both observations and numerical models, should be carried out in order to reveal the sensitivity of the meteotsunami magnitude to the variability in the atmospheric perturbation velocity. Furthermore, it also would be interesting to test if the numerical high-resolution atmospherical models used to generate the meteotsunamigenic atmospheric disturbances are capable of reproducing this variability in the propagation speed and direction.

A.3. Perturbation amplitude

Finally, we will determine how the amplitude of the perturbation conditions the meteotsunami amplitude and the sea response to perturbations with similar amplitudes will be compared to outline the key features that affect the sea wave amplification. In Williams et al. (2021), it is suggested that the amplification factor induced by Proudman resonance on the sea wave does not depend on the magnitude of the atmospheric disturbance, but on other factors. Hence, a large magnitude atmospheric perturbation would generate a large sea level response that could lead to a severe meteotsunami only if the amplification conditions are optimal. We have some examples of this in the reported cases. In 23S2 a 2.5 hPa jump causes a sea level oscillation of 109 cm (a total amplification factor of ∼40), meanwhile in 23S4 there is a pressure jump of 4 hPa that have a response smaller than 40 cm. In this particular case we have two possible explanations for this difference. In first place the first jumps is much quicker which increases the resonance by Proudman according to Eq. 2.20, that implies that the amplification by Proudman is proportional to the first derivative of the perturbation. This does not explain completely the small response in 23S4, since in the wavelet power spectrum we can see an important amount of energy between 10 and 20 min for the atmospheric perturbation. If we go to Fig. 4.8, the speed (∼30 m/s) and the direction of propagation (∼230°) fall within the appropriated interval of values for the occurrence of maximum amplification in Ciutadella (Vilibić et al., 2008; Ličer et al., 2017). Hence, the hypothesis introduced here to explain the lack of sea level response of 23S4 is that there existed a 180° phase difference between the oscillation trapped in the port and the incoming sea wave that resulted in a destructive interference. In Fig. 4.11b it can be seen how there is, indeed, an incoming wave measured in SBL with ∼ 25 cm that is not amplified in CIU. Furthermore, just before 1700 UTC the CIU sea level time series loses its 10 min natural period, skipping a sea level trough and forming a 20 min oscillation. The confirmation of this hypothesis would add additional uncertainty to the estimation of the meteotsunami magnitude, since small errors in the forecasting of the pressure perturbation timing would lead to a completely different sea level response. This problem of the destructive interference should not affect the first meteotsunami oscillation that finds a Ciutadella Harbour in calm. However, during the event when oscillations between 30 and 50 cm are present within the port the phase difference between the forcing wave and the trapped wave could be critical, resulting in larger amplifications if they are in phase or in the wave destruction if they have opposite phase, as would be the case of 23S4. Further research should investigate the meteotsunami magnitude sensitivity to this phase difference.

Following the same idea of understanding why atmospheric perturbations with similar amplitudes have different sea level responses, we can compare the subevent 10S1 and 23S2. Although in both cases we can find a rapid pressure jump of 2.5 hPa with high energy between 5 and 20 min period, the sea level oscillation is more than a 50% larger for 23S2. The atmospheric perturbation speed estimated over Mallorca for 10S1 is ∼23 m/s with propagation direction 250° and for 23S2 it is ∼33 m/s with also 250° propagation direction. With this incoming angle an atmospheric perturbation impinging Ciutadella will pass over the northern part of the Menorca channel which is deeper (90 - 130 m) than the southern (∼ 80 m) resulting in optimal Proudman resonance for larger propagation speed. This reasoning is confirmed by the numerical experiment of Vilibić et al. (2008). They forced a numerical sea model with pressure jumps with different propagation speeds and directions. Their results show that the amplification produced by a perturbation

travelling at a 33 m/s speed is a factor 1.5 larger than the amplification of a perturbation travelling at a 23 m/s speed, both with a direction of 250°. These results are very similar to the difference in amplitude of the sea level response for 10S1 and 23S2 both with pressure jumps of 2.5 hPa and travelling with direction 250° but with different speed.

Another interesting observation is that the largest sea level oscillation reported here, the 115 cm oscillation in 18S1, was caused by an atmospheric perturbation of just 1hPa of amplitude. In Fig. 4.20c we can see how the spectral energy of the perturbation is found between 20 and 5 min and the perturbation velocity computed during this subevent is 30 m/s at a 210 direction. For this particular values Vilibić et al. (2008) and Ličer et al. (2017) results differ since according to Ličer et al. (2017) the amplification for a perturbation with this velocity is maxima while the results by Vilibić et al. (2008) suggest a very weak sea response. The perturbation used by Ličer et al. (2017) is sinusoidal, a shape closer to the atmospheric perturbation measured during this event than the pressure jump used in Vilibić et al. (2008). Although all the observed parameters lead to a large amplification, the key factor here to explain the huge amplification induced over a relatively small perturbation is the fact that the perturbation oscillation last for two complete cycles allowing the accumulation of energy at the proper frequency within Ciutadella Harbour.

Some attempts of quantifying the relation between these three parameters (atmospheric perturbation amplitude, speed and direction) and the final meteotsunami amplitude have been carried out without success. From the three presented meteotsunami events, we have been able to understand the complexity of this task. In some cases, we have found some explanations to the different sea level responses caused by apparently similar atmospheric perturbations, while in some other cases we cannot explain the sea level response resulting from its atmospheric counterpart. In further research, and with a larger meteotsunami data set, it could be interesting to work in the creation of an empirical index that includes, not only the synoptic conditions, but also the characteristics of the mesoscale perturbation.

B. Harbour amplification

As can be observed in Fig. 4.2 and 4.4 the harbour resonance completely conditions the spectral energy of the measured sea level within the ports and bays and it is a really important factor contributing to the sea level perturbation amplification. The three ports with higher observed oscillations, namely Ciutadella, Port de Sóller and Portocolom, are those that have a stronger normal mode which appear as the only relevant mode in the wavelet power spectra.

The most studied port is Ciutadella, with its well known ∼10.5 min normal mode. Some previous studies have attributed a Q-factor ∼ 10 to this harbour (Rabinovich et al., 2009). By applying Eq. 2.28 to the *background* spectrum for CIU we obtain a Q-factor ∼ 8 a bit smaller than the theoretical value. This difference could be caused by the assumption of $Q \gg 1$ that has to be made to reach Eq. 2.28 from Eq. 2.27. In Chap. 4 we have related the sea wave height in Son Blanc to the sea wave in Ciutadella, and we have observed a factor of amplification between 2 and 3 between SBL and CIU measurements. The fact that this factor is much lower than 10 is explained because we are computing the amplification factor using as forcing the sea level measured at SBL, which also has been amplified by the topography out of the harbour. Moreover, the amplification needs Q/π oscillation cycles to reach its maximum (Rabinovich et al., 2009) and in most cases the arriving sea wave have only one oscillation. It is worth noticing that this observed

amplification factor between SBL and CIU is quite constant when the incoming wave at SBL have energy for periods below 30 min. This means that once the wave has been amplified at open sea, its response in the harbour is quite constant.

For the other ports it is not realistic to apply the model of Eq. 2.27 since the natural response of the harbours is not characterized by a main peak, but it has several spectral peaks that contribute similarly to the final sea wave height.

C. Propagation along the Balearic basin

One of the goals of this work was to study the propagation of the meteotsunami sea perturbation along the Balearic Islands. A first glance to the sea level time series for different tide gauges during a meteotsunami event (Fig. 4.3) reveals that this may not be an easy task. Since harbour resonance strongly conditions the final spectral energy measured by our tide gauges, all ports present very different spectral energy distribution and the oscillation maxima are located at different times not showing any kind of propagation in the direction of propagation of the atmospheric perturbation.

Then, the idea was to apply the *background* technique to remove the natural response of each harbour and obtain the external forcing at each location. In theory, the resulting forcings should be quite similar between nearby ports where the atmospheric forcing is almost the same as, for example, in the ports of the east coast of Mallorca. The results obtained are, however, disappointing since, as it has been explained in detail in Chap. 4 for the results presented in Fig. 4.12, there are important differences in the estimated forcings, even for very close tide gauges. The most surprising result is the energy difference in the forcings of SBL and CIU which should be the same. Monserrat et al. (1998) applied this technique to the data measured by a tide gauge at the entrance of Ciutadella Harbour and a tide gauge within the harbour, obtaining very similar forcings for both instruments. Those good results make us think that there may be an error in the application of the *background* technique, however, none of the attempts to compute the *background* spectrum differently have led to better results. Marcos et al. (2009) used the same idea to compare the forcings at Cala Ratjada and at Ciutadella obtaining a high similitude which led them to clearly identify the propagation of the sea forcing from Mallorca to Menorca. The attempt of reproducing those results, shown in Fig. 4.12e, has also failed.

All in all, we do not discard that the technique may not have been correctly implemented, and that should be confirmed in the future. However, the doubts on the suitability of the technique raised from our results are legit and should be also taken into account since the theoretical reasoning behind it is based on certain unrealistic assumptions: it considers that the forcing is stationary, and it assumes that when the background spectrum is computed the existing forcing has a white noise spectrum. It may happen that for the selected calm periods a particular weak forcing very different from the forcing during the meteotsunami events is present, which could invalidate the use of the technique. Finally, the assumption of a non-stationary forcing have been tested translating the same technique to the wavelet power spectrum resulting in the same unclear results. In further research, numerical simulation could be used to better estimate the natural response of the harbours, thus avoiding the problem of poorly estimated *background* spectra.

Chapter 6

Conclusion

In this thesis we have described a series of meteotsunami events taking advantage of a new ultra-dense observational network: the event of 23 May 2021 has been analysed in detail and the most important features of the events of 10 May and 18 June 2021 have also been presented for comparison. The goal behind this analysis was to compare the observations with the known meteotsunami generation mechanisms, that have been gathered in Chap. 2. We have analysed the atmospheric synoptic conditions where the atmospheric perturbations have been generated and propagated, the characteristics of the atmospheric perturbation and the amplification of the meteotsunami wave. The events have been characterized through the analysis of time series of sea level and atmospheric pressure, and ERA5 reanalysis has been used to study the atmospheric synoptic conditions during the events. To these basic analysis we have added the estimation of the atmospheric perturbation propagation speed and direction. Finally, the *background* technique (Rabinovich, 1997) to estimate the external forcing has been implemented, and its suitability has been assessed.

The results have shown that the synoptic patterns observed during the three events are consistent with the established synoptic conditions for meteotsunamis in the Balearic Islands (Ramis and Jansà, 1983; Šepić et al., 2016). Regarding the mechanism favouring the propagation of the atmospheric disturbance during the 23 May and 18 June 2021 events, the formation of a wave duct seems plausible and convective activity could also contribute to the atmospheric perturbation propagation through wave-CISK. To discern which of the mechanisms is acting in these events, we would need higher resolution atmospheric data that could be obtained from high-resolution atmospherical simulations (Belušić et al., 2007; Šepić et al., 2009). During 10 May 2021 event, the formation of a wave duct seems unlikely, and the pressure perturbations are probably caused by a convective system. Unfortunately, the lack of spatial and temporal resolution of ERA5 data prevents from clearly discern the generation mechanism and specific numerical simulations would be required. We must take into account that even present numerical models do not reproduce exactly the atmospheric perturbation shape, so there is still room to investigate how the reproduction of these mesoscale perturbations could be improved.

The characteristics of the atmospheric perturbations have also been analysed through the time series, the wavelet power spectrum and the estimation of their velocity. A high degree of heterogeneity both in time and space has been detected among pressure time series measured in barographs around the Balearic Islands. The perturbation amplitude and shape changes along its path, and it may affect differently in different locations. The velocity of propagation also changes during the meteotsunami event. This is an

important result as in most of the previous numerical studies (e.g., (Orlić et al., 2010; Ličer et al., 2017)) the perturbations have been considered as uniform and stationary. Thus, more research is required to understand how the heterogeneity of the atmospheric perturbations impact on the meteotsunami generation and amplification.

Moreover, the importance of the spectral energy, the amplitude, the speed and the direction of the atmospheric disturbance in the amplitude of the sea level oscillation in Ciutadella has also been investigated. The use of a long time series of sea level and atmospheric pressure from Ciutadella (1 November 2018 - 21 June 2021) has allowed us to compare the atmospheric variability with the sea level variability, in different frequency bands. The results show a high correlation ($\rho > 0.75$) between them for the frequency band around 10 min, which includes the natural mode of Ciutadella (10.5 min), when we are using long averaging windows (> 2 hours) and during meteotsunami events. Otherwise, in calm periods, the correlation coefficient is always lower than during a meteotsunami event. Moreover, it is observed that the correlation decreases when the length of the averaging window is reduced. These results lead to the following conclusions: *i*) the presence of energy at these high frequencies in the atmosphere is necessary to generate large sea level oscillations in Ciutadella; *ii*) it may not be simultaneity, neither proportionality, between the high-frequency perturbation and the severe sea level response; *iii*) other parameters, as the perturbation velocity, are determinant to the occurrence of meteotsunamis. Thus, the perturbation velocity can explain the differences in the amplification produced by similar atmospheric forcings in some reported subevents. To generalize the results observed here, more meteotsunami events should be analysed with the goal to clearly define the ranges of speeds and directions of the perturbations that produce large amplifications, similarly to the numerical experiments from Vilibić et al. (2008) and Ličer et al. (2017). This methodology could also be extended to other harbours in the Balearic Islands thanks to the new observational data. The amplitude of the atmospheric disturbances is also found to be related to the meteotsunami amplitude, since large meteotsunamis are caused by large perturbations. Nevertheless, the spectrum and the velocity of the perturbation condition the amplification that the initial amplitude suffers, which may result in relatively small perturbations causing large meteotsunamis thanks to the existence of optimal amplification conditions, and vice versa.

The detailed inspection of the sea level and atmospheric pressure time series during the events has led us to detect the importance of the forcing duration, that can increase the amplification of the sea level oscillation through energy accumulation within the harbour, as happens during subevent 18S1. During subevents 23S3-23S4, it seems that the phase difference between the incoming wave and the standing oscillation within the harbour results in a destructive interference that avoid the meteotsunami amplification. The effect of both, perturbation duration and phase difference between the forcing wave and the harbour oscillations, have never been considered before as mechanisms that can influence the meteotsunami amplitude. Therefore, it would be interesting to quantify their impact by means of numerical experiments.

The effect of Proudman resonance has been described using the sea level data at Son Blanc, which tide gauge was located outside Ciutadella Harbour. It has been observed that the amplification factor at open sea is higher than that expected from Proudman resonance according to the analytical solution (Eq. 2.21). Thus, additional amplification mechanisms besides Proudman resonance must have influenced the wave amplification. On one hand, it may be that some topographical effects are not taken into account in Son Blanc. On the other hand, other amplification mechanism, as the lens effect on the

Menorca Channel mentioned in Ličer et al. (2017), may contribute to create amplifications higher than those by Proudman resonance. It is also outlined, from the analytical solution and contrasted with the wavelet power spectrum in Son Blanc, that the open sea amplification by Proudman produces higher amplifications in higher frequency perturbations. Paying more attention to Son Blanc sea level measurements to determine the part of the amplification that must be attributed to the topographical effects would help to clarify these hypotheses.

Finally, the harbour amplification in Ciutadella has been described by comparing the sea level measurements in the harbour with those of Son Blanc located outside the harbour. The results show an amplification factor of 2-3 due to harbour resonance. This factor is lower than the theoretical amplification factor, which has been estimated as 8-10. The reasons could be: *i*) that the sea level measured in Son Blanc has suffered from some kind of topographical amplification, and *ii*) that several cycles are required for the harbour oscillation to reach its maximum amplification. We also have tested the *background* technique (Rabinovich, 1997) to characterize the forcing outside the harbours, and to be able to describe the propagation of the open sea perturbations in the outer shelf. However, the obtained results are very poor which has cast doubts on the suitability of this technique. More work is needed to determine if this technique has been correctly applied during this work. Alternatively, in the future, the transfer function between outside perturbations and harbour response could be estimated using numerical modelling.

The results gathered by this Master thesis could be condensed in the creation of a new index that would relate the characteristics of the atmospheric perturbation (spectrum, speed, direction,...) to the meteotsunami amplitude, in the same way that the synoptic situation is related to the meteotsunami amplitude by the Šepić et al. (2016) index. To construct this new index, the examination of a large meteotsunami dataset is required, and the results from the suggested numerical experiments could be also incorporated. In future works, it would be interesting to take a closer look into the meteotsunamis occurring in other ports of the Balearic Islands to verify if their generation mechanisms are comparable to those described for Ciutadella. All this research would lead to a broader comprehension of the meteotsunami sensibility to different parameters from different spatial and temporal scales that would help to determine the meteotsunami predictability by the present numerical models and may help to improve the current early warning systems.

References

Bechle, A. J., and C. H. Wu, 2014: The lake michigan meteotsunamis of 1954 revisited. *Natural Hazards*, **74 (1)**, 155–177, doi:10.1007/s11069-014-1193-5, URL https://doi.org/10.1007/s11069-014-1193-5.

Belušić, D., B. Grisogono, and Z. B. Klaić, 2007: Atmospheric origin of the devastating coupled air-sea event in the east Adriatic. *Journal of Geophysical Research Atmospheres*, **112 (17)**, 1–14, doi:10.1029/2006JD008204.

Buchwald, V. T., and R. A. de Szoeke, 1973: The response of a continental shelf to travelling pressure disturbances. *Marine and Freshwater Research*, **24 (2)**, 143–158, doi:10.1071/MF9730143, URL https://doi.org/10.1071/MF9730143.

Candela, J., S. Mazzola, C. Sammari, R. Limeburner, C. J. Lozano, B. Patti, and A. Bonanno, 1999: The mad sea phenomenon in the strait of sicily. *Journal of Physical Oceanography*, **29 (9)**, 2210 – 2231, doi:10.1175/1520-0485(1999)029⟨2210:TMSPIT⟩2.0.CO;2, URL https://journals.ametsoc.org/view/journals/phoc/29/9/1520-0485_1999_029_2210_tmspit_2.0.co_2.xml.

Churchill, D. D., S. H. Houston, and N. A. Bond, 1995: The Daytona Beach Wave of 3-4 July 1992: A Shallow-Water Gravity Wave Forced by a Propagating Squall Line. *Bulletin of the American Meteorological Society*, **76 (1)**, 21–32, doi:https://doi.org/10.1175/1520-0477(1995)076⟨0021:TDBWOJ⟩2.0.CO;2, URL https://journals.ametsoc.org/view/journals/bams/76/1/1520-0477_1995_076_0021_tdbwoj_2_0_co_2.xml.

Denamiel, C., J. Šepić, D. Ivanković, and I. Vilibić, 2019: The adriatic sea and coast modelling suite: Evaluation of the meteotsunami forecast component. *Ocean Modelling*, **135**, 71–93, doi:https://doi.org/10.1016/j.ocemod.2019.02.003, URL https://www.sciencedirect.com/science/article/pii/S1463500318302464.

Donn, W. L., and M. Ewing, 1956: Stokes' edge waves in lake michigan. *Science*, **124 (3234)**, 1238–1242, doi:10.1126/science.124.3234.1238, URL https://science.sciencemag.org/content/124/3234/1238.

Drago, A., 2009: Sea level variability and the 'milghuba' seiche oscillations in the northern coast of malta, central mediterranean. *Physics and Chemistry of the Earth, Parts A/B/C*, **34 (17)**, 948–970, doi:https://doi.org/10.1016/j.pce.2009.10.002, URL https://www.sciencedirect.com/science/article/pii/S1474706509001156.

Emery, W. J., and R. E. Thomson, 2001: Chapter 5 - time-series analysis methods. *Data Analysis Methods in Physical Oceanography*, W. J. Emery, and R. E. Thomson, Eds., Elsevier Science, Amsterdam, 371 – 567, doi:https://doi.org/10.1016/

B978-044450756-3/50006-X, URL http://www.sciencedirect.com/science/article/pii/B978044450756350006X.

Ewing, M., F. Press, and W. L. Donn, 1954: An explanation of the lake michigan wave of 26 june 1954. *Science*, **120 (3122)**, 684–686, doi:10.1126/science.120.3122.684, URL https://science.sciencemag.org/content/120/3122/684.

Fontserè, E., 1934: Les seixes de la costa catalana. *Servei Meteorologic de Catalunya, Notes d'estudi*, 58.

Garcies, M., D. Gomis, and S. Monserrat, 1996: Pressure-forced seiches of large amplitude in inlets of the balearic islands: 2. observational study. *Journal of Geophysical Research: Oceans*, **101 (C3)**, 6453–6467, doi:https://doi.org/10.1029/95JC03626, URL https://agupubs.onlinelibrary.wiley.com/doi/abs/10.1029/95JC03626.

Gomis, D., S. Monserrat, and J. Tintoré, 1993: Pressure-forced seiches of large amplitude in inlets of the balearic islands. *Journal of Geophysical Research: Oceans*, **98 (C8)**, 14 437–14 445, doi:https://doi.org/10.1029/93JC00623, URL https://agupubs.onlinelibrary.wiley.com/doi/abs/10.1029/93JC00623.

Green, G., 1838: On the motion of waves in a variable canal of small depth and width. *Transactions of the Cambridge Philosophical Society*, **6**, 457.

Greenspan, H. P., 1956: The generation of edge waves by moving pressure distributions. *Journal of Fluid Mechanics*, **1 (6)**, 574–592, doi:10.1017/S002211205600038X.

Hibiya, T., and K. Kajiura, 1982: Origin of theabiki phenomenon (a kind of seiche) in nagasaki bay. *Journal of the Oceanographical Society of Japan*, **38 (3)**, 172–182, doi:10.1007/BF02110288, URL https://doi.org/10.1007/BF02110288.

Hodžić, M., 1979: Exceptional oscillations in the bay of vela luka and meteorological situation on the adriatic. *I Course International School of Meteorology of the Mediterranean*, Erice.

Honda, K., T. Terada, and D. Isitani, 1908: Viii. on the secondary undulations of oceanic tides. (an abstract.). *The London, Edinburgh, and Dublin Philosophical Magazine and Journal of Science*, **15 (85)**, 88–126, doi:10.1080/14786440809463750, URL https://doi.org/10.1080/14786440809463750.

Intergovernmental Oceanographic Commission, 2016: Tsunami glossary. Paris, UNESCO, 44 pp.

Jansa, A., S. Monserrat, and D. Gomis, 2007: The rissaga of 15 June 2006 in Ciutadella (Menorca), a meteorological tsunami. *Advances in Geosciences*, **12 (1983)**, 1–4, doi:10.5194/adgeo-12-1-2007.

Jansà, A., and C. Ramis, 2021: The balearic rissaga: from pioneering research to present-day knowledge. *Natural Hazards*, **106 (2)**, 1269–1297, doi:10.1007/s11069-020-04221-3, URL https://doi.org/10.1007/s11069-020-04221-3.

Jansà, A., 1986: Respuesta marina a perturbaciones mesometeorológicas: la rissaga de 21 de junio de 1984 en ciutadella (menorca). *Revista de Meteorología (AME)*, **3 (7)**, 5–29, URL http://hdl.handle.net/20.500.11765/1917.

Jansà, A., 1990: Servei experimental de predicció de rissagues, in les rissagues de ciutadella i altres oscil·lacions de nivel de la mar de gran amplitud a la mediterrània, textos de les comunicacions presentades a les i jornades, ciutadella de menorca, del 14 al 16 de maig de 1987. *IME Col·lecció Recerca*, **2**, 85–91, ISBN: 84-86752-05-1.

Jansà, A., and X. Jansà, 1980: Obra cultural de menorca, isbn 84-600-1438-x jansà. *Oceanografia, in enciclopèdia de Menorca*, Vol. 1, 161–235,.

Lagarias, J., J. Reeds, M. Wright, and P. Wright, 1998: Convergence properties of the nelder–mead simplex method in low dimensions. *SIAM Journal on Optimization*, **9**, 112–147, doi:10.1137/S1052623496303470.

Lindzen, R. S., 1974: Wave-cisk in the tropics. *Journal of Atmospheric Sciences*, **31 (1)**, 156 – 179, doi:10.1175/1520-0469(1974)031⟨0156:WCITT⟩2.0.CO;2, URL https://journals.ametsoc.org/view/journals/atsc/31/1/1520-0469_1974_031_0156_wcitt_2_0_co_2.xml.

Lindzen, R. S., and K.-K. Tung, 1976: Banded convective activity and ducted gravity waves. *Monthly Weather Review*, **104 (12)**, 1602 – 1617, doi:10.1175/1520-0493(1976)104⟨1602:BCAADG⟩2.0.CO;2, URL https://journals.ametsoc.org/view/journals/mwre/104/12/1520-0493_1976_104_1602_bcaadg_2_0_co_2.xml.

Liu, P. L.-F., S. Monserrat, and M. Marcos, 2002: Analytical simulation of edge waves observed around the balearic islands. *Geophysical Research Letters*, **29 (17)**, 28–1–28–4, doi:https://doi.org/10.1029/2002GL015555, URL https://agupubs.onlinelibrary.wiley.com/doi/abs/10.1029/2002GL015555.

Ličer, M., B. Mourre, C. Troupin, A. Krietemeyer, A. Jansá, and J. Tintoré, 2017: Numerical study of balearic meteotsunami generation and propagation under synthetic gravity wave forcing. *Ocean Modelling*, **111**, 38–45, doi:https://doi.org/10.1016/j.ocemod.2017.02.001, URL https://www.sciencedirect.com/science/article/pii/S1463500317300136.

Marcos, M., S. Monserrat, R. Medina, A. Orfila, and M. Olabarrieta, 2009: External forcing of meteorological tsunamis at the coast of the Balearic Islands. *Physics and Chemistry of the Earth*, **34 (17-18)**, 938–947, doi:10.1016/j.pce.2009.10.001, URL http://dx.doi.org/10.1016/j.pce.2009.10.001.

Metzner, M., M. Gade, I. Hennings, and A. B. Rabinovich, 2000: The observation of seiches in the baltic sea using a multi data set of water levels. *Journal of Marine Systems*, **24 (1)**, 67–84, doi:https://doi.org/10.1016/S0924-7963(99)00079-2, URL https://www.sciencedirect.com/science/article/pii/S0924796399000792.

Miles, J., and W. Munk, 1961: Harbor paradox. *Journal of the Waterways and Harbors Division*, **87 (3)**, 111–132, doi:10.1061/JWHEAU.0000223, URL https://ascelibrary.org/doi/abs/10.1061/JWHEAU.0000223.

Monserrat, S., A. Ibbetson, and A. Thorpe, 1991a: Atmospheric gravity waves and the 'rissaga' phenomenon. *Quarterly Journal of the Royal Meteorological Society*, **117**, 553–570.

Monserrat, S., A. B. Rabinovich, and B. Casas, 1998: On the reconstruction of the transfer function for atmospherically generated seiches. *Geophysical Research Letters*, **25 (12)**, 2197–2200, doi:10.1029/98GL01506.

Monserrat, S., C. Ramis, and A. J. Thorpe, 1991b: Large-amplitude pressure oscillations in the western mediterranean. *Geophysical Research Letters*, **18 (2)**, 183–186, doi:https://doi.org/10.1029/91GL00234, URL https://agupubs.onlinelibrary.wiley.com/doi/abs/10.1029/91GL00234.

Monserrat, S., and A. J. Thorpe, 1992: Gravity-Wave Observations Using an Array of Microbarographs In the Alearic Islands. *Quarterly Journal of the Royal Meteorological Society*, **118 (504)**, 259–282, doi:10.1002/qj.49711850405.

Monserrat, S., and A. J. Thorpe, 1996: Use of ducting theory in an observed case of gravity waves. *Journal of the Atmospheric Sciences*, **53**, 1724–1736.

Monserrat, S., I. Vilibić, and A. B. Rabinovich, 2006: Meteotsunamis: atmospherically induced destructive ocean waves in the tsunami frequency band. *Natural Hazards and Earth System Sciences*, **6 (6)**, 1035–1051, doi:10.5194/nhess-6-1035-2006, URL https://nhess.copernicus.org/articles/6/1035/2006/.

Mourre, B., and Coauthors, 2020: On the potential of ensemble forecasting for the prediction of meteotsunamis in the Balearic Islands: sensitivity to atmospheric model parameterizations. *Natural Hazards*, **106 (2)**, 1315–1336, doi:10.1007/s11069-020-03908-x, URL https://doi.org/10.1007/s11069-020-03908-x.

Nomitsu, T., 1935: A theory of tsunamis and seiches produced by wind and barometric gradient. *Memoirs of the College of Science; Kyoto Imperial University Series A*, **18**, 201–214.

Okal, E. A., 2019: Twenty-five years of progress in the science of "geological" tsunamis following the 1992 nicaragua and flores events. *Pure and Applied Geophysics*, **176 (7)**, 2771–2793, doi:10.1007/s00024-019-02244-x, URL https://doi.org/10.1007/s00024-019-02244-x.

Orlic, M., 1980: About a possible occurrence of the proudman resonance in the adriatic. *Thalassia Jugoslavica*, **16**, 79–88.

Orlić, M., D. Belušić, I. Janeković, and M. Pasarić, 2010: Fresh evidence relating the great Adriatic surge of 21 June 1978 to mesoscale atmospheric forcing. *Journal of Geophysical Research: Oceans*, **115 (6)**, 1–19, doi:10.1029/2009JC005777.

Pattiaratchi, C. B., and E. M. S. Wijeratne, 2015: Are meteotsunamis an underrated hazard? *Philosophical Transactions of the Royal Society A: Mathematical, Physical and Engineering Sciences*, **373 (2053)**, 20140 377, doi:10.1098/rsta.2014.0377, URL https://royalsocietypublishing.org/doi/abs/10.1098/rsta.2014.0377.

Powers, J. G., and R. J. Reed, 1993: Numerical simulation of the large-amplitude mesoscale gravity-wave event of 15 december 1987 in the central united states. *Monthly Weather Review*, **121 (8)**, 2285 – 2308, doi:10.1175/1520-0493(1993)121⟨2285:NSOTLA⟩2.0.CO;2, URL https://journals.ametsoc.org/view/journals/mwre/121/8/1520-0493_1993_121_2285_nsotla_2_0_co_2.xml.

Proudman, J., 1929: The effects on the sea of changes in atmospheric pressure. *Geophysical Journal International*, **2 (s4)**, 197–209, doi:https://doi.org/10.1111/j.1365-246X.1929.tb05408.x, URL https://onlinelibrary.wiley.com/doi/abs/10.1111/j.1365-246X.1929.tb05408.x.

Rabinovich, A., S. Monserrat, and I. Fain, 1999: Numerical modelling of extreme seiche oscillations ('rissaga waves') in vicinity of the balearic islands. *Oceanology*, **39**.

Rabinovich, A. B., 1997: Spectral analysis of tsunami waves: Separation of source and topography effects. *Journal of Geophysical Research: Oceans*, **102 (C6)**, 12 663–12 676, doi:10.1029/97JC00479.

Rabinovich, A. B., 2020: Twenty-Seven Years of Progress in the Science of Meteorological Tsunamis Following the 1992 Daytona Beach Event. *Pure and Applied Geophysics*, **177 (3)**, 1193–1230, doi:10.1007/s00024-019-02349-3.

Rabinovich, A. B., and S. Monserrat, 1996: Meteorological tsunamis near the balearic and kuril islands: Descriptive and statistical analysis. *Natural Hazards*, **13 (1)**, 55–90, doi:10.1007/BF00156506, URL https://doi.org/10.1007/BF00156506.

Rabinovich, A. B., and S. Monserrat, 1998: Generation of meteorological tsunamis (large amplitude seiches) near the balearic and kuril islands. *Natural Hazards*, **18 (1)**, 27–55, doi:10.1023/A:1008096627047, URL https://doi.org/10.1023/A:1008096627047.

Rabinovich, A. B., I. Vilibić, and S. Tinti, 2009: Meteorological tsunamis: Atmospherically induced destructive ocean waves in the tsunami frequency band. *Physics and Chemistry of the Earth*, **34 (17-18)**, 891–893, doi:10.1016/j.pce.2009.10.006.

Ramis, C., and A. Jansà, 1983: Condiciones meteorológicas simultáneas a la aparición de oscilaciones del nivel del mar de amplitud extraordinaria en el mediterraneo occidental. *Revista de Geofísica*, **(39)**, 35–42.

Renault, L., G. Vizoso, A. Jansá, J. Wilkin, and J. Tintoré, 2011: Toward the predictability of meteotsunamis in the balearic sea using regional nested atmosphere and ocean models. *Geophysical Research Letters*, **38 (10)**, doi:https://doi.org/10.1029/2011GL047361, URL https://agupubs.onlinelibrary.wiley.com/doi/abs/10.1029/2011GL047361.

Romero, R., M. Vich, and C. Ramis, 2019: A pragmatic approach for the numerical prediction of meteotsunamis in ciutadella harbour (balearic islands). *Ocean Modelling*, **142**, 101 441, doi:https://doi.org/10.1016/j.ocemod.2019.101441, URL https://www.sciencedirect.com/science/article/pii/S1463500319301210.

Salaree, A., R. Mansouri, and E. A. Okal, 2018: The intriguing tsunami of 19 march 2017 at bandar dayyer, iran: field survey and simulations. *Natural Hazards*, **90 (3)**, 1277–1307, doi:10.1007/s11069-017-3119-5, URL https://doi.org/10.1007/s11069-017-3119-5.

Šepic, J., I. Vilibic, A. B. Rabinovich, and S. Monserrat, 2015: Widespread tsunami-like waves of 23-27 June in the Mediterranean and Black Seas generated by high-Altitude atmospheric forcing. *Scientific Reports*, **5 (January)**, 1–8, doi:10.1038/srep11682.

Šepić, J., I. Vilibić, and D. Belušić, 2009: Source of the 2007 ist meteotsunami (adriatic sea). *Journal of Geophysical Research: Oceans*, **114 (C3)**, doi:https://doi.org/10.1029/2008JC005092, URL https://agupubs.onlinelibrary.wiley.com/doi/abs/10.1029/2008JC005092.

Šepić, J., I. Vilibić, and I. Fine, 2015: Northern adriatic meteorological tsunamis: Assessment of their potential through ocean modeling experiments. *Journal of Geophysical Research: Oceans*, **120 (4)**, 2993–3010, doi:https://doi.org/10.1002/2015JC010795, URL https://agupubs.onlinelibrary.wiley.com/doi/abs/10.1002/2015JC010795.

Šepić, J., I. Vilibić, and S. Monserrat, 2009: Teleconnections between the adriatic and the balearic meteotsunamis. *Physics and Chemistry of the Earth, Parts A/B/C*, **34 (17)**, 928–937, doi:https://doi.org/10.1016/j.pce.2009.08.007, URL https://www.sciencedirect.com/science/article/pii/S1474706509001077.

Šepić, J., I. Vilibić, and S. Monserrat, 2016: Quantifying the probability of meteotsunami occurrence from synoptic atmospheric patterns. *Geophysical Research Letters*, **43 (19)**, 10,377–10,384, doi:https://doi.org/10.1002/2016GL070754, URL https://agupubs.onlinelibrary.wiley.com/doi/abs/10.1002/2016GL070754.

Stull, R., 1988: *An Introduction to Boundary Layer Meteorology.* Atmospheric and Oceanographic Sciences Library, Springer Netherlands.

Tintoré, J., D. Gomis, S. Alonso, and D.-P. Wang, 1988: A theoretical study of large sea level oscillations in the western mediterranean. *Journal of Geophysical Research: Oceans*, **93 (C9)**, 10 797–10 803, doi:https://doi.org/10.1029/JC093iC09p10797, URL https://agupubs.onlinelibrary.wiley.com/doi/abs/10.1029/JC093iC09p10797.

Torrence, C., and G. P. Compo, 1998: A Practical Guide to Wavelet Analysis. *Bulletin of the American Meteorological Society*, **79 (1)**, 61–78, doi:10.1175/1520-0477(1998)079⟨0061:APGTWA⟩2.0.CO;2, URL https://doi.org/10.1175/1520-0477(1998)079⟨0061:APGTWA⟩2.0.CO;2.

Ursell, F., and G. I. Taylor, 1952: Edge waves on a sloping beach. *Proceedings of the Royal Society of London. Series A. Mathematical and Physical Sciences*, **214 (1116)**, 79–97, doi:10.1098/rspa.1952.0152, URL https://royalsocietypublishing.org/doi/abs/10.1098/rspa.1952.0152.

Vennell, R., 2007: Long barotropic waves generated by a storm crossing topography. *Journal of Physical Oceanography*, **37 (12)**, 2809 – 2823, doi:10.1175/2007JPO3687.1, URL https://journals.ametsoc.org/view/journals/phoc/37/12/2007jpo3687.1.xml.

Vich, M. d. M., and R. Romero, 2021: Forecasting meteotsunamis with neural networks: the case of Ciutadella harbour (Balearic Islands). *Natural Hazards*, **106 (2)**, 1299–1314, doi:10.1007/s11069-020-04041-5, URL https://doi.org/10.1007/s11069-020-04041-5.

Vilibić, I., C. Denamiel, P. Zemunik, and S. Monserrat, 2020: The mediterranean and black sea meteotsunamis: an overview. *Natural Hazards*, doi:10.1007/s11069-020-04306-z, URL https://doi.org/10.1007/s11069-020-04306-z.

Vilibić, I., S. Monserrat, A. Rabinovich, and H. Mihanović, 2008: Numerical modelling of the destructive meteotsunami of 15 june, 2006 on the coast of the balearic islands. *Pure and Applied Geophysics*, **165 (11)**, 2169–2195, doi:10.1007/s00024-008-0426-5, URL https://doi.org/10.1007/s00024-008-0426-5.

Vilibić, I., and J. Šepić, 2009: Destructive meteotsunamis along the eastern adriatic coast: Overview. *Physics and Chemistry of the Earth, Parts A/B/C*, **34 (17)**, 904–917, doi:https://doi.org/10.1016/j.pce.2009.08.004, URL https://www.sciencedirect.com/science/article/pii/S1474706509001089.

Vilibić, I., J. Šepić, N. Dunić, F. Sevault, S. Monserrat, and G. Jordà, 2018: Proxy-based assessment of strength and frequency of meteotsunamis in future climate. *Geophysical Research Letters*, **45 (19)**, 10,501–10,508, doi:https://doi.org/10.1029/2018GL079566, URL https://agupubs.onlinelibrary.wiley.com/doi/abs/10.1029/2018GL079566.

Welch, P., 1967: The use of fast fourier transform for the estimation of power spectra: A method based on time averaging over short, modified periodograms. *IEEE Transactions on Audio and Electroacoustics*, **15 (2)**, 70–73, doi:10.1109/TAU.1967.1161901.

Williams, D. A., K. J. Horsburgh, D. M. Schultz, and C. W. Hughes, 2021: Proudman resonance with tides, bathymetry and variable atmospheric forcings. *Natural Hazards*, **106 (2)**, 1169–1194, doi:10.1007/s11069-020-03896-y, URL https://doi.org/10.1007/s11069-020-03896-y.

Zemunik, P., and Coauthors, 2021: Observing meteotsunamis ("marrobbio") on the southwestern coast of sicily. *Natural Hazards*, **106 (2)**, 1337–1363, doi:10.1007/s11069-020-04303-2, URL https://doi.org/10.1007/s11069-020-04303-2.